# A CELLULARIZED BIOMATERIAL MODEL OF CARDIAC FIBROBLASTS FOR EVALUATION OF FIBROBLAST INDUCED CHANGES IN STIFFNESS

by

James Paul Kennedy

A dissertation submitted to the faculty of
The University of Utah
in partial fulfillment of the requirements for the degree of

Doctor of Philosophy

Department of Bioengineering

University of Utah

May 2013

# The University of Utah Graduate School

## STATEMENT OF DISSERTATION APPROVAL

The dissertation of **James Paul Kennedy**

has been approved by the following supervisory committee members:

| | | |
|---|---|---|
| **Robert Hitchcock** | , Chair | **3/12/13** Date Approved |
| **Vladimir Hlady** | , Member | **3/12/13** Date Approved |
| **Greg Burns** | , Member | **3/13/13** Date Approved |
| **Patrick Tresco** | , Member | **3/12/13** Date Approved |
| **David Grainger** | , Member | **3/12/13** Date Approved |

and by **Patrick Tresco**, Chair of the Department of **Bioengineering**

and by Donna M. White, Interim Dean of The Graduate School.

# ABSTRACT

Chronic heart failure (CHF) is a life-altering long-term condition that contributes a substantial burden to our healthcare system. It is caused by a maladaptive remodeling of the heart mediated through fibroblast synthesis, degradation, and modification of extracellular matrix (ECM). It is currently managed through pharmacologic intervention or medical device treatment, but can be reversed only through heart transplantation. Cell therapy is a new approach to treating CHF that promises to prevent and potentially reverse cardiac remodeling through interaction with cardiac fibroblasts. Adherent bone marrow derived stem cells (MSC) are one of the most promising candidates for use in cell therapies. The major challenge hindering standard clinical application of MSC therapy is limited understanding of how MSC interact with heart cells to reverse remodeling. Numerous techniques are available to harvest, isolate, and modify MSC, however these techniques are believed to influence the efficacy of the treatment. Current techniques for evaluating efficacy of MSC treatments are either prohibitively difficult or significantly limited in their ability to assess functional changes. Establishing an *in vitro* platform for evaluating the influence of MSC coculture on performance characteristics of cardiac fibroblasts is a logical and efficient step prior to successful clinical implementation of MSC therapy. The objective of this research was to develop a three-dimensional (3D) tissue model that allows investigation of the underlying mechanism

responsible for MSC mediated cardiac regeneration. The three phases of this work included: (1) development of a biomaterial substrate capable of sustaining fibroblast attachment, proliferation, and alignment, (2) development of a culture platform and seeding techniques capable of providing sufficient mass transport to sustain a relatively thick 3D scaffold populated with both fibroblasts and MSC (3) application of the substrate and culture platform to evaluate changes in mechanical properties and cell distribution resulting from MSC coculture with cardiac fibroblasts.

To my wife, Jill

TABLE OF CONTENTS

ABSTRACT ..... iii

LIST OF FIGURES ..... viii

ACKNOWLEDGEMENTS ..... x

Chapters

1 INTRODUCTION ..... 1

1.1 Introduction ..... 1
1.2 The Cardiac Fibroblast ..... 4
1.3 Cardiac Disease and Heart Failure ..... 14
1.4 Cardiac Cell Therapy ..... 19
1.5 Three-Dimensional Culture Models ..... 22
1.6 Summary and Contributions ..... 33
1.7 References ..... 38

2 DESIGN OF SEMIAUTOMATEDTOOLING FOR FABRICATION OF POROUS POLYURETHANE FOAMS ..... 49

2.1 Introduction ..... 49
2.2 Spray Parameters ..... 50
2.3 Tooling Applications ..... 53

3 THE MECHANICALLY ENHANCED PHASE SEPARATION OF SPRAYED POLYURETHANE SCAFFOLDS AND THEIR EFFECT ON THE ALIGNMENT OF FIBROBLASTS ..... 64

3.1 Introduction ..... 65
3.2 Materials and Methods ..... 66
3.3 Results ..... 67
3.4 Discussion ..... 68
3.5 Conclusion ..... 70
3.6 Acknowledgements ..... 70

3.7 Appendix ..... 70
3.8 References ..... 70

4 ENGINEERED CHANNELS ENHANCE CELLULAR DENSITY IN PERFUSED SCAFFOLDS ..... 72

4.1 Introduction ..... 73
4.2 Methods ..... 74
4.3 Results ..... 76
4.4 Discussion ..... 78
4.5 Conclusion ..... 80
4.6 Acknowledgments ..... 80
4.7 Appendix A ..... 80
4.8 References ..... 80

5 MSC COCULTURE INCREASES TISSUE STIFFNESS IN THREE-DIMENSIONAL CARDIAC FIBROBLAST MODEL ..... 82

5.1 Abstract ..... 82
5.2 Introduction ..... 83
5.3 Materials and Methods ..... 87
5.4 Results ..... 97
5.5 Discussion ..... 100
5.6 Acknowledgements ..... 105
5.7 References ..... 105

6 CONCLUSION AND FUTURE DIRECTIONS ..... 121

6.1 Summary and Conclusions ..... 121
6.2 Applications and Future Directions ..... 124
6.3 References ..... 129

APPENDIX: ENGINEERING PRINTS OF PERFUSION BIOREACTOR ..... 134

LIST OF FIGURES


2.1 Spray assembly ..... 55

2.2 Nozzle assembly ..... 56

2.3 Spray surface assembly ..... 57

2.4 Waste reservoir ..... 58

2.5 Spray plate ..... 59

2.6 Spray substrate ..... 60

2.7 Scaffold frame ..... 61

2.8 Mask ..... 62

2.9 Alignment pin and T-nut ..... 63

3.1 Representative SEM images of scaffolds ..... 67

3.2 Effective modulus of elasticity of scaffolds ..... 68

3.3 Porosity of scaffolds ..... 69

3.4 Confocal image of aligned fibroblasts ..... 69

3.5 Surface plot of 2D FFT and intensity angle plot ..... 69

3.6 Orientation index of porous scaffolds ..... 69

3.7 Cross sectional SEM of laminated scaffold ..... 70

4.1 Polyester frame and lamination procedure ..... 74

4.2 Fabrication of patterned substrates ..... 75

4.3 Custom molded silicone adapter ..... 75

4.4 Culture chamber and schematic of bioreactor ..... 76

4.5 SEM imaging of scaffold sheets ..... 77

4.6 Hydraulic permeability testing ..... 77

4.7 Cross-sectional images of constructs ..... 78

4.8 Spatial image analysis of cross sections ..... 79

4.9 Cell density ..... 79

5.1 Culture platform schematic ..... 109

5.2 Image processing method ..... 110

5.3 Initial phenotyping of cardiac cell population ..... 111

5.4 3T3 Fb density with different seeding velocities and substrate coatings ..... 112

5.5 Cardiac Fb uniformity with different seeding velocities and durations ..... 113

5.6 Mean cardiac Fb density with different seeding velocities and durations ..... 114

5.7 Treatment induced changes in stiffness ..... 115

5.8 Tensile modulus of MSC coculture constructs ..... 116

5.9 Cell characterization during culture ..... 117

5.10 Collagen labeling during culture ..... 118

# ACKNOWLEDGEMENTS

I gratefully acknowledge my advisor and mentor, Dr. Robert Hitchcock, who provided me with the guidance, insight and support to complete this work. I thank my advisory committee members for their guidance, insight, and persistent efforts to enhance the quality of my education: Drs. David Grainger, Greg Burns, Patrick Tresco, and Vladimir Hlady. I acknowledge my fellow graduate students Richard Lasher, Monir Parikh, Tanner Coleman, Kylee North, and Chao Huang, for their friendship and technical support during this work. I humbly acknowledge the essential contributions of the undergraduate students who worked with me: Sean McCandless, Asad Rauf, Laura Williams, Jason Hansen, Jenn Hillam, Molly Person, Jessica Ashmead, Hendrik Stegall, John Lackey, Alexis Johnson, Joseph Goodrick, Martin Jensen, Ryan Russon, Mark Sedlacek, Karan Mehta, and Shaswat Chapagain. Finally, I thank my family, especially my wife Jill and my parents Jim and DeAnn for their continuous love, optimisim, and encouragement.

# CHAPTER 1

# INTRODUCTION

## 1.1 Introduction

Chronic heart failure is a significant problem facing the United States. In 2006, there were 5.8 million Americans living with heart failure [1]. The associated personal and economic burdens are enormous. The most common acute cause of heart failure is myocardial infarction (MI) [1]. Infarct-induced ischemia and hypoxia lead to myocyte depletion in the infarct zone and border regions, and local activation of inflammatory and fibroblast cell types. These two physiologic responses to MI often result in a self-sustaining series of detrimental structural changes to the heart. Typically termed maladaptive remodeling, this phenomenon is a biomechanical process that is attributed to changes in passive stiffness of the ventricular wall. More specifically, maladaptive remodeling is a consequence of changes in ventricular wall stiffness during two distinct phases of healing after MI. During the early post-MI phase, the stiffness of the infarct area is dramatically decreased. Rupture, dyskinesis, and infarct expansion arise from insufficient stiffness of the ventricular wall and lead to infarct expansion, dilated cardiomyopathy, decreased ejection fraction, and systolic heart failure. On the other hand, during the later post-MI healing phase, activated myofibroblasts (myoFb) increase

matrix production and organization to stiffen the infarcted region. In many cases, increased matrix accumulation in regions remote to the infarct accompanies local matrix deposition. Increased passive stiffness in remote regions prevent adequate filling of the ventricle during diastole, and leads to diastolic heart failure. Both cases, systolic and diastolic heart failure, are results of pathologic changes in passive stiffness. Prevention of maladaptive remodeling and regeneration of myocardial function after MI relies on a delicate balance of passive stiffness and therefore is profoundly influenced through the matrix regulation activity of cardiac fibroblasts (CFb).

Cardiac cell therapy appears to be a promising new treatment to prevent heart failure after MI [2]. The aim of this therapy is to enhance *in situ* regeneration of cardiac function. Modulation of the CFb response during post-MI healing is one potentially powerful approach that may lead to functional myocardial regeneration. Despite significant findings initially, cell therapy has been delayed in its transition to a standard treatment following MI. Delivery of bone marrow cells including mesenchymal stem cells (MSC) has been shown in animal models to increase positive clinical endpoints such as ejection fraction and survival [3, 4]. However, in multisubject human clinical trials, cell therapy has not significantly prevented or reversed cardiac remodeling [5]. To realize the potential of cardiac cell therapy, we need to elucidate the mechanism behind the apparent MSC-induced cardiac regeneration observed in animal models.

One pathway to increased understanding of MSC-heart interactions is the development of better *in vitro* model systems. Two-dimensional (2D) coculture of MSC and CFb relies on subjective interpretation of expression of ECM components and regulators to draw speculative conclusions about changes in stiffness. The most recent

three-dimensional (3D) engineered tissue models allow investigation of survival, integration, differentiation, and coupling between stem cells and cardiac cells [6-8]. These models, however, are aimed at understanding how stem cells can help recover active contraction of cardiac tissue rather than modulating the passive stiffness. Prior to the work described in this dissertation, no model capable of directly coupling changes in stiffness with stem cell therapy has been described. The overarching purpose of the work described in this dissertation was to investigate the effects of MSC coculture with CFb mediated changes in stiffness. The objective of this work was accomplished through three distinct research phases:

1. Develop and characterize a 3D substrate capable of supporting and influencing fibroblast attachment and organization.
2. Design and validate a perfusion culture platform that supports a uniform fibroblast distribution throughout a 3D substrate of scalable thickness.
3. Apply the substrate and culture platform to evaluate MSC therapy on CFb-mediated changes in stiffness *in vitro*.

To provide a conceptual framework to this work, the physiologic role of the cardiac fibroblast, the impetus and mechanics of heart failure, cardiac cell therapy, and state-of-the-art cell culture and tissue engineering models are reviewed below.

## 1.2. The Cardiac Fibroblast

### 1.2.1 The Fibroblast in Cardiac Physiology

The human heart is a four chambered pump responsible for ensuring adequate metabolic exchange in our body. The primary function of the cardiovascular system is to

convectively transport blood (and the metabolites it contains) throughout the body. The role of the heart in this system is to generate a pressure gradient that will move blood through the vasculature. Pulsatile flow is generated through a biphasic process consisting of filling (diastole) and emptying (systole) of the heart. During diastole, the pressure of the blood entering the ventricle is stored as strain energy in the ventricular wall as the ventricle stretches to accommodate an increased blood volume. Systole begins when the heart contracts. The active mechanical contraction of the heart can be described as a sudden and significant increase in the stiffness of the heart wall. The balance between the stress and strain of the tissue during diastole is no longer stable. The effectively stiffer tissue causes the ventricular muscle to contract to balance the stress with a proportionally smaller strain. The contraction of the heart is responsible for expelling a fraction of the blood and driving it through the body. The ejection fraction is a function of the difference between passive mechanical properties, and active mechanical contraction.

The majority of heart cells are either cardiac fibroblasts, or cardiac myocytes. Myocytes occupy the majority of the volume of the heart [9]. These cells are responsible for generation of active mechanical properties of the heart. Through an elegant excitation-contraction mechanism, electrical action potentials are converted to mechanical work – shortening of the cardiac myocyte. Tissue organization and specific timing converts small contractions of individual cells to macroscopic tissue contraction.

The cardiac fibroblast is the other major cell type in the heart. Roughly 60-70% of all cells in the heart are fibroblasts [10]. These cells contribute to electrical, biochemical, and structural characteristics of cardiac muscle. Fibroblasts, unlike myocytes, are nonexcitable cells. They play a passive role in propagation of action potentials through

cardiac muscle by acting as obstacles to the orderly spread electrical excitation in the heart. Recent discoveries have also implicated fibroblasts in a more active role in cardiac electrophysiology through gap junction connections with each other and cardiac myocytes [11, 12]. CFb also maintain the structure and composition of cardiac extracellular matrix (ECM). Type I and III collagen account for 90% of the protein content of the cardiac ECM [13]. The ECM helps mechanically couple myocytes, and transfers the force generated by individual myocytes throughout the organ [14]. Moreover, the ECM composition and organization provides the passive stiffness and toughness necessary during systole. Coordinated action of both myocytes and fibroblasts is necessary to maintain cardiac function. The following sections describe in further detail the role of the cardiac fibroblast in maintaining the structure and function of the cardiac ECM.

### 1.2.2 The Myofibroblast

In 1971, Gabbiani and colleagues observed what they termed a "modified fibroblast" and suggested that these cells have an important role in wound contraction [15]. The distinguishing features of these cells included increased expression of an intracellular fibrillar system, nuclear deformations (due to contraction of the cell), and increased intercellular connections [15]. This modified type of the cardiac fibroblast has come to be known as the myofibroblast. The most discernible structural feature of the myofibroblast when compared to the fibroblast is the presence of smooth muscle actin and myosin. The distinction between CFb and the myofibroblast is significant in terms of activity. Cardiac fibroblasts have been referred to as "silent" under normal circumstances

in the heart. The myofibroblast phenotype, on the other hand is typically associated with the active matrix synthesis, degradation, and modification activities normally associated with fibroblasts in general.

The transition to a myofibroblastic phenotype occurs in response in vivo to mechanical stimulation, hypoxia, and inflammatory cytokines [16]. In vitro, increased substrate stiffness has been shown to cause fibroblasts to assume a myofibroblastic phenotype [17]. Anseth and colleagues utilized a light sensitive hydrogel to demonstrate that myofibroblast differentiation is nonterminal, and can be reversed. Myofibroblasts on a relatively stiff hydrogel substrate were induced to deactivate by decreasing their substrate modulus [18]. Importantly, it has been hypothesized that increased stiffness *in vivo* due to fibrosis results in positive feedback, with more fibroblasts becoming activated and assuming the myofibroblast phenotype [19].

A specific definition of myofibroblasts as a different cell type has yet to be generally established. Indeed, fibroblasts are pleomorphic in the sense that they change their structure and function depending on external stimuli [10]. Therefore, in this work the myofibroblast will be considered a phenotypic subset of the fibroblast. In the section below, the fibroblast mediated mechanisms of ECM turnover are discussed. Elevated levels of ECM modification are typically associated with what is considered a myofibroblast phenotype.

### 1.2.3 Fibroblast Maintenance of the Extracellular Matrix

One primary physiologic role of cardiac fibroblasts (CFb) is to regulate extracellular matrix composition and properties through a complex network of interactive

mechanisms. One of the important functions of the ECM is to maintain the passive stiffness and elasticity of cardiac muscle. Indeed it has been shown that ECM components, even in hypertrophic disease conditions, are almost entirely responsible for passive stiffness of the heart muscle [20]. CFb respond to chemical and mechanical cues that result in matrix synthesis, matrix degradation, and ECM modification. These tasks are accomplished through ECM component synthesis (primarily type I and type III collagen), expression of matrix metalloproteinases (MMP's) and protease inhibitors (TIMP), and expression of matrix cross-linking enzymes enzymes (e.g., lysyl oxidases).

CFb are responsible for production of procollagen fibers that will eventually become type I and type III collagen, the primary dictators of passive cardiac stiffness [21]. CFb synthesis of collagen is modulated through growth factors (e.g., TGF-β), signal peptides (e.g., angiotensin II), and cytokines (e.g., interleukins, TNF-α) [13]. The most potent regulators of collagen synthesis in CFb appear to be TGF-β, the rennin-angiotensin-aldesterone system (RAAS) and β-adrenergic system [22]. CFb also respond to mechanical stress by immediately increasing collagen deposition [16]. In vitro, CFb have been shown to increase matrix production in response to cyclic strain [23].

Another key role of the cardiac fibroblast is expression of matrix metalloproteinases (MMP). MMP are a family of zinc-dependent proteins expressed throughout the body. This class of proteases is responsible for cleaving extracellular matrix (ECM) molecules. In the heart, MMP play a critical role in maintaining the balance of ECM synthesis and degradation, as well as influencing ECM organization [24].

MMP are typically classified according to their substrate specificity. Cardiac fibroblasts express MMP-1, MMP-2, MMP-3, MMP-9, and MMP-14. Collagenase-type MMPs (MMP-1) cleave fibrillar collagen (type I, II, III). Gelatinases (MMP-2 and MMP-9) cleave gelatin, nonfibrillar collagen and fibronectin. Stromelysins (MMP-3), like gelatinases, can cleave gelatins, nonfibrillar collagens, and fibronectin; however, they also cleave laminin and MMP zymogens. This makes the stromelysin class of MMP important for regulation of other classes of MMP. The last class of MMP found in the heart are membrane bound proteases. MMP-14, a membrane bound MMP, has the same substrate specificity to stromelysins, plus fibrillar collagen. Cytokines (TNF-alpha, IL-1), growth factors (TGF-beta), signal molecules (angiotensin, endothelin), reactive oxygen species (ROS), and mechanical stimuli all affect MMP transcription.

MMP-1, 3 and 9 expression is typically low, and is upregulated by proinflammatory cytokines such as TNF-α and IL-6. MMP-2 and MMP-9 are expressed constitutively, however their expression can be increased by proinflammatory cytokines or decreased by angiotensin II through the TGF-β pathway. MMP-14 expression, remarkably, is increased by TGF-β expression. MMP-1 cleaves fibrillar collagen (types I, II, and III) and MMP-1 expression has been shown to mitigate pathologic cardiac remodeling in transgenic mice [25]. Conversely, increased expression of MMP-2 has been associated with early (0-7 day) left ventricular rupture after infarction and late stage (4 week) dilatation in a murine MMP-2 knock-out model [26]. Increased expression of MMP-14 has also been shown to favor pathologic remodeling of the heart [27]. However, in a different murine model of heart failure, treatment with a proinflammatory nuclear protein 2 weeks after infarction increased the activity of MMP-2 and MMP-9. In apparent

contradiction to previous findings, increased activity of MMP-2 resulted in higher ejection fractions and lower dilatation 7 weeks after infarction [28].

Because of the critical role of MMP in maintaining healthy, homeostatic condition of the ECM, they are tightly regulated not only in expression, but in function through a family of four different MMP inhibitors (TIMP). TIMP-3 is one of the major inhibitors found in cardiac tissue; it inhibits the function of all cardiac fibroblast-produced MMP. TIMP-3 is produced by most cardiac cells including myocytes, vascular smooth muscle cells, and fibroblasts. In addition to its function as an MMP inhibitor, TIMP-3 has MMP-independent effects including modulating Fb differentiation to myoFb, decreasing angiogenesis, signaling smooth muscle cell apoptosis, and preventing cardiomyocyte proliferation [29, 30].

Another fibroblast-mediated mechanism of ECM regulation in the heart is lysyl oxidase (LOX) production. LOX and LOX-like (LOXL) proteins are found throughout the body, including in the heart [31]. In the heart, LOX is an extracellular enzyme produced by CFb responsible for forming cross-links in types I and III fibrillar collagen. Crosslinking is the final step in collagen synthesis, and results in collagen fibrils that are less soluble, more resistant to degradation, and much stiffer [32]. LOX expression is stimulated through hypoxia and TNF-α (mediated through TGF-β signaling) [33].

The last, and indirect method of CFb maintenance of the ECM is through cellular signaling. Fibroblasts, in response to angiotensin II, increase production of TGF-β which in turn act as a potent autocrine signal for ECM modulation [34]. Further, CFb are the primary source of tumor necrosis factor-α (TNF-α) which serves as both an autocrine signaling molecule for fibroblast activity, and a paracrine signal molecule for numerous

other cell types [35]. Interleukin-6 (IL-6) is another CFb-produced molecule that influences cell activity in the heart [36]. In response to proinflammatory cytokines, human CFb has been shown to upregulate expression of cell surface markers such as ICAM-1 and E-selectin that facilitate leukocyte recruitment [37]. These cells in turn, express ROS that enhance the function of LOX.

Until recently, the focus on cardiac tissue has been on the elegant excitation contraction mechanism of cardiac myocytes. Fibroblasts have been relegated to bystander status with little appreciation given for the role they play in maintenance and support of the myocardium. We are now beginning to understand just how important fibroblasts are in the production, maintenance and remodeling of the cardiac ECM. Myocytes play little role in the ECM synthesis and architecture yet rely on this matrix to act in synchrony to develop a functional contraction to pump blood through our vasculature. Understanding the role that fibroblasts play in creating and maintaining the exquisite balance of mechanical properties needed for optimum cardiac performance is paramount for the development of regenerative strategies for cardiac repair.

### 1.2.4 Fibroblast Contributions to Biomechanical Stiffness

Fibroblasts are the most numerous stromal cell type in the heart. Fibroblasts have been shown to contribute to tissue stiffness through two different mechanisms: directly through tractional forces including cytoskeletal filament contraction [38] and indirectly through expression and assembly of matrix elements. Here both contributions of fibroblasts to the biomechanical stiffness of 3D tissue will be reviewed.

Some of the earliest studies investigating cell tractional forces were performed in collagen gels. Bell and colleagues developed a unique 3D model of dermal fibroblast (Fb) behavior by casting living fibroblasts inside a collagen gel [39]. They observed six to eight fold decreases in collagen expression in 3D collagen matrices when compared to 2D culture conditions. Further, the collagen that was produced in the 3D model appeared to be tightly bound to the surrounding matrix while collagen produced in 2D culture was passed to the culture medium [40]. In addition, they observed that upon incorporation into the gel lattice, fibroblasts began to extend processes and collect collagen fibrils. This compaction of collagen resulted in macroscopic contraction of the collagen gel [41]. Grinnell and colleagues modified this model to evaluate fibroblast mediated contraction of collagen gels. They utilized either floating, unconstrained collagen gels, or mechanically anchored gels to evaluate fibroblast mediated contraction of the gels [42]. Floating gels were unstressed throughout the experiments, while anchored gels developed internal stresses. Two different mechanisms of contraction of the gels were observed; in unstressed gels, tractional forces resulting from extension of Fb processes was responsible for contraction. Moreover, in unstressed gels, the fibroblasts maintained a dendritic morphology and did not produce high level of actin stress fibers [43]. In contrast to their behavior in unstressed gels, Fb in stressed gels were observed to elongate into a lamellar phenotype expressing higher levels of smooth muscle actin filaments [44]. Upon release of the gel, these cells also were observed to contract the collagen gel. Although the outcome of gel contraction was identical, the difference in Fb response to the two conditions indicated the possibility of a different mechanism responsible for each condition. Indeed it was observed that contraction of unstressed collagen is primarily due

to extension of cellular processes that create tractional forces, while contraction of stressed gels results from smooth muscle-like contraction of the Fb themselves [45]. Grinnell further demonstrated the difference in these mechanism by showing that contraction can be induced in floating gels by platelet derived growth factor (PDGF) stimulation, while contraction in the stressed state is not induced by PDGF [46]. Coupling cell-populated collagen gels to strain gauges in order to measure cell tractional forces allowed assessment of tractional force, however this approach is limited to measuring bulk forces, and cannot assess the contribution of individual cells [38].

Elegant methods for measuring individual cell tractional forces (CTF) have been developed to understand the forces that can be generated by fibroblasts to complement the work that was performed using cell-populated collagen gels. In 1980, Harris et al. described a method of culturing cells on a thin polymer film and observing wrinkling of the film as a measure of CTF [47]. This method was improved by anchoring the edges the silicone film, and incorporating fiduciary beads. The embedded beads allow quantification of surface deformation, and therefore permit estimation of the CTF with force resolution approaching nanonewtons [48]. The elasticity of the silicone film in conjunction with the surface deformation can be used to create a surface force map. An alternative to the use of silicone films is the use of polyacrylamide gels [49]. Mircobead markers embedded in the gel provide deformation data, while the concentration of acrylamide determines the stiffness of the gel. The low affinity of cells for polyacrylamide gels requires gel coating with ECM proteins such as fibronectin to allow mediate cell attachment. Use of micromachined force sensors is another approach to

measuring CTF. Du Roure and colleagues developed a micropost array that is able to measure post deformation and correlate the deformation directly to cellular forces [50].

In addition to the potential for active contraction, cardiac stromal cells contribute to stiffness of cardiac tissue through expression and assembly of matrix elements as described in the previous section. Collagen (primarily type I and type III) is the predominant constituent of cardiac extracellular matrix. By volume, it comprises 2-6% of the myocardium [51]. Despite the low volume fraction, collagen appears to be the primary contributor to myocardial stiffness due to its relatively high modulus. The modulus of a single procollagen molecule ranges from 2.9 to 9.0 GPa as measure using an X-ray diffraction technique [52]. Once assembled into macroscopic filaments, collagen fibers are considerably softer, measured at 0.7-3.7 MPa using tensile stress-strain analysis [53]. Collagen fibers are coupled to the cells themselves through lateral struts that are anchored through focal adhesion complexes [54]. Confocal microscopy has revealed that interstitial collagen fibers in the relaxed heart resemble a helical twisted ribbon with relatively high degree of tortuosity [55]. During diastole as the myocardium is strained, it appears that perimysial collagen fibers are not elongated, but rather undergo helical bending and uncrimping. The energy required to bend and uncrimp the collagen appears to accounts for the majority of the measured stiffness in the myocardium [56]. In a mathematical model of cardiac tissue these forces have been calculated to be on the order of 135-160 MPa [56] which correspond to roughly 100% of the modulus measured in rat ventricular tissue [57].

In the model described in this research, Fb are grown on a non-degradable, elastic polyurethane substrate. The goal of the research to evaluate tissue-level changes in

passive stiffness, so while this model as described in this work cannot discriminate between individual contributions of cells and matrix, it can provide an overall functional picture of changes in tissue stiffness. In reality, the overall changes in stiffness measured in this model are a composite value corresponding to contribution of both active cell tractional forces, and passive matrix stiffness.

## 1.3. Cardiac Disease and Heart Failure

### 1.3.1 Cardiac Disease

Heart disease is a leading cause of death worldwide [58]. In America, an average of 2,300 people died every day from cardiovascular disease in 2006 [1]. Many cardiovascular diseases including infarction, hypertension, valvular diseases, and congenital heart disease lead to the same end stage outcome: heart failure [59]. Heart failure is currently only treatable with transplant and has a high associated mortality. Moreover, heart failure is a chronic condition that constitutes a major socio-economic burden to nations, and a significant personal burden to families and individuals. Rates of heart failure are increasing in developed countries due to longer life-spans and increased likelihood of surviving of acute myocardial injury (primarily infarction) [22].

Heart failure occurs when the cardiac output is unable to meet the metabolic demands of the body. There are two mechanisms of heart failure: systolic and diastolic [60]. Systolic heart failure occurs when the heart is unable to generate sufficient force to eject all of the blood from the heart. Ejection fraction is typically decreased during systolic heart failure. Systolic heart failure results from decreased efficiency of cardiac contraction. Ischemia/infarction can cause myocyte necrosis and apoptosis, which may

contribute to systolic HF. The primary impetus, however, for systolic HF is expansion of the dilatation of the ventricular chamber which increases wall stresses and creates further stress on functional myocytes [22].

Diastolic heart failure, on the other hand results from inadequate filling of the ventricle. This is almost exclusively a result of fibrosis, which in turn is a secondary effect of a primary cardiac pathology. During diastolic heart failure, increases in stiffness of the cardiac muscle prevent adequate filling of the ventricle during diastole. So while ejection fraction may remain high, cardiac output is decreased.

Both systolic and diastolic heart failure are results of maladaptive structural remodeling of the heart. While there are many cardiovascular diseases that share HF as an end-stage outcome, here only HF induced through coronary artery disease and myocardial infarction is addressed.

### 1.3.2 Maladaptive Remodeling

Studies of the biomechanical response of the left ventricle (LV) to myocardial infarction (MI) have identified infarct expansion (i.e., stretching) and infarct-induced fibrosis of remote tissue as important phenomenon that both initiate and sustain a progressive pathologic process that ultimately results in structural and functional changes of the heart [61, 62]. This maladaptive response is a complex biomechanical process caused by depletion of myocytes from the infarct zone and a biologic response to abnormal stress distributions in the heart [63]. Clinically, ventricular remodeling is a primary indicator of adverse outcomes such as chronic heart failure and death [64].

Within minutes to hours of ischemia-induced hypoxia, cellular death occurs and cardiac tissue ceases to be an active, force-generating tissue, and assumes passive viscoelastic mechanical properties [65]. Systolic stiffness of the infarcted tissue is decreased drastically. During this phase, the tissue begins to be depleted of its myocyte population through necrosis (20% of cells) and apoptosis (80% of cells) [66]. Simultaneously, the disparity between the systolic stiffness of the unimpaired heart and infarcted region results in dyskinesis and stretching of the infarcted region [67]. This mismatch in stiffness dissipates the mechanical energy generated by the contractile region of the heart, resulting in decreased ejection fraction (EF). Stroke volume is maintained by increasing the end diastolic volume (EDV), and results in long-term cardiac dilatation. However, cardiac dilatation further increases the burden on functional myocytes through increased wall stresses according to Laplace's law [63]. Moreover, it is during this acute phase prior to infarct stiffening through neomatrix formation that the risk of catastrophic failure resulting from rupture of the ventricle is highest [61]. A rapid increase in the passive stiffness of the infarcted tissue is imperative for maintaining cardiac function.

Within hours, the passive (diastolic) stiffness of the tissue begins to increase due to edema [65]. In an ovine model of MI, passive stiffness of infarcted tissue increased by approximately 250% after 4 hrs [68]. At about 1 week postinfarction in humans, the fibrotic phase begins resulting in accumulation of collagen produced by activated myofibroblasts. This local deposition of collagen results in significantly increased stiffness of the infarct. In the previously mentioned ovine model, the passive stiffness increased by 800% at 1 week post-MI, and 1600% at 2 weeks [68]. This increase in

stiffness is critical for minimizing infarct expansion, decreasing the risk of rupture, and restoring ejection fraction by decreasing the energy loss due to infarct stretching. Indeed insufficient stiffening of the infarcted region results in infarct expansion, wall thinning, and dilatated cardiomyopathy; all of which are predictive factors pointing toward systolic heart failure [61]. While stiffening of the infarcted region is critical for prevention of maladaptive remodeling, it is a double-edged sword. Stiffening of the infarct has been associated with stiffening of regions remote to the infarct as well. Gupta et al. showed that in the ovine model of MI, the passive stiffness of the remote myocardium had increased >300% at 1 week [68]. Using a rabbit model of hypertension-induced heart failure, Yamamoto et al. demonstrated that changes in the passive stiffness of cardiac tissue are due to fibrosis, rather than compensatory hypertrophy of the myocyte population that is associated with both hypertensive and MI induced heart failure [20]. In a sheep model of MI, Wilson et al. demonstrated that matrix metalloproteinase (MMP) and tissue inhibitors of metalloproteinases (TIMP) levels in the remote regions were altered compared to control values indicative of ECM remodeling remote to the infarct [69]. Accumulation of collagen in sites remote to the infarct results in pathologic fibrosis, and increased passive stiffness of the myocardium which in turn causes decreased EDV of the heart, decreased cardiac output, and diastolic heart failure.

It is clear that changes in active and passive mechanical properties of both the infarct and noninfarcted myocardium are key parameters affecting ventricular remodeling and corresponding health outcomes after MI. During the early stages after MI it is essential to have a significant increase in passive stiffness of the infarcted zone. However, in later stages, increased fibrosis in the infarct leads to remote matrix

accumulation, global stiffening of the heart, pathologic fibrosis, and diastolic heart failure.

### 1.3.3 The Role of the Cardiac Fibroblast in Remodeling

Cardiac fibroblasts are jointly responsible with acute phase inflammatory cells for wound healing after cardiac injury. The successful recapitulation of cardiac function after the initial insult is largely dependent on the activity of CFb. Upon infarction, inactive MMP found in the interstitial space become are zymogenically activated as surrounding matrix is degraded in response to necrotic and apoptotic signals from myocytes. This immediate activation results in a local and significant degradation of collagen. Takahashi et al. demonstrated that within 3 hrs after infarction, 50% of collagen in the infarct region was degraded in rats [70]. Increased MMP activity and resultant decreases in the collagen volume fraction in the heart have been correlated with ventricular dilatation and systolic dysfunction [71].

Collagen cross-linking is another important factor that impacts cardiac function. Fibroblasts affect collagen cross-linking through LOX production and secretion. While it has been shown that collagen production increases in the infarct region [72], this does not necessarily translate to an increase in tissue stiffness (see [68]). Several studies have correlated increases in collagen cross-linking with increases in apparent myocardial stiffness [73, 74]. These increases in apparent myocardial stiffness, and not just collagen content are hypothesized to be responsible for diastolic dysfunction of the heart.

The passive stiffness of the myocardium is paramount in determining post-MI outcomes. Scar formation in myocyte depleted regions is a dynamic process consisting of

continuous collagen turnover, cytokine expression, and myofibroblastic activation persisting in humans for decades [75]. ECM and therefore the cardiac fibroblast clearly have an important role in maintaining the geometry and elasticity of the heart in both the acute and long term after infarction. Improved understanding of the mechanisms responsible for fibroblast-mediated changes in stiffness will provide a foundation for novel therapeutic approaches to treating heart failure.

## 1.4. Cardiac Cell Therapy

Under normal conditions after MI, myocytes are depleted from the wound site via necrosis or apoptosis. Fibroblasts replace the missing myocytes with a stiff, dense scar. Little regeneration of cardiac muscle occurs. Chronic mechanical stimulation and autocrine signaling through TGF-β and TNF-α results in maladaptive remodeling and heart failure initiated by changes in ventricular fibroblast activity. Starting around the year 2000, a novel approach to regenerating cardiac muscle began to be explored: cardiac cell therapy.

The complex biologic and mechanical impetus of ventricular remodeling makes it a challenging pathology to treat. Indeed, medical device and pharmacologic treatments are used to manage and minimize cardiac remodeling, but are generally unable to reverse its course [62]. Heart transplantation remains the most effective method for treating maladaptive remodeling, but is limited by a persistent shortage of donor organs. Cardiac cell therapy is a promising new treatment that is currently in the early phases of clinical trials [2, 76]. In a single case study performed by Okano and colleagues, a myoblast "cell-sheet" was delivered to a patient with progressive heart failure. After implantation,

this treatment improved the patient's EF from 26% to 46%, allowed explantation of his left ventricular assist system, and removed him from the heart transplant waiting list [77].

Cell therapy utilizes exogenous cells to stimulate cardiac regeneration. Early attempts to regenerate cardiac function focused on delivering cells that would replace the myocytes lost to ischemic injury. In the last 12 years, however, the cardiac cell therapy paradigm has shifted largely away from replacement of myocytes, to cytoprotective and regenerative paracrine support of cardiac function [66, 78]. Utilization of mesenchymal stem cells (MSC) in animal models, has shown considerable promise as a treatment to prevent postinfarction remodeling. Moreover, the low immunogenicity of MSC allows the use of allogenic donor cells and proprietary expansion methods of MSC make this cell type attractive to biotech companies interested in commercialization [5].

In small animal models of MI, MSC have been shown to effectively treat some of the major histologic and functional pathologies associated with ventricular remodeling. Mias et al. showed that in a rat MI model, injection of MSC pretreated with melatonin significantly increased ejection fraction (EF), and decreased wall thinning and collagen accumulation [4]. Godier-Furnémont and colleagues utilized a decellularized human tissue patch to deliver TGF-β pre-conditioned mesenchymal precursor cells to a nude rat MI model [79]. Histologically, they observed increased angiogenesis; functionally, they observed increased fractional shortening (FS) of the heart. Another group genetically modified MSC to increase prostaglandin I synthase (PG1S) transcription. Increased PG1S production resulted in increased FS and EF, while simultaneously decreasing fibrosis, wall thinning and apoptosis [80]. Gnecchi et al. showed that MSC's modified with ATK-

1, a cytoprotective factor encoding gene, were shown to result in smaller infarct sizes and decreased myocyte apoptosis after infarction in rats [81].

Despite the numerous animal studies performed, and their favorable results, the mechanism behind the observed efficacy of cell therapy in animal models is still poorly understood. There are, in fact, at least five proposed paracrine mechanisms that may be responsible for the histologic and functional improvements observed in animal studies: (1) Decreased remodeling of the myocardium, (2) paracrine mediated angiogenesis, (3) modulation of the immune response, (4) cytoprotection of residual myocytes in the infarct region and border zones, and (5) recruitment of resident cardiac progenitor cells [82-85]. This lack of mechanistic understanding becomes significantly more important when the results of early human clinical trials are considered. Unlike most animal models, the efficacy of cell therapy in humans has been questionable. A meta analysis of 13 clinical trials with a total of 811 patients revealed that bone marrow cell therapy did not improve postinfarction remodeling [5]. Further mechanistic investigation of cell therapy is paramount for moving cell therapies from the trial phase to a standard treatment in the clinic.

Certain approaches to cell therapy have proposed that the fibroblast may be an important therapeutic target for cell therapy. Mias et al. showed that fibroblast MMP expression was altered by paracrine factors from injected MSC [4]. While this study is key, there is no direct link between the expression of MMP and mechanical properties, which are more directly responsible for the function of the heart. Development of a model that couples changes in bulk mechanical properties based on cell injection

approaches will accelerate our ability to design cell-based therapies that more effectively prevent maladaptive remodeling of the heart.

## 1.5. Three-Dimensional Cell Culture Models

*In vitro* cell culture is a common tool used to evaluate the response of cells to stimuli. Practically, cell culture is an essential component of all drug and device development. Indeed ISO 10993 – the international standard for medical device biocompatibility – requires that cell culture be used to evaluate cytotoxicity for all medical devices adhering to this standard. The primary components of cardiac cell culture strategies are: (1) the substrate, (2) the environmental culture conditions, (3) the culture medium, and (4) the cells themselves [86]. Since the first attempts at cell culture, researchers have been defining and refining these elements of cell culture. Current tissue culture plastic (TCP) based cell culture models are the result of decades of discovery and development.

In more recent history, focus has shifted from development of cell culture models that are cultured on a flat substrate like TCP, to development of three-dimensional (3D) cell culture models [87]. This has been a particularly challenging paradigm shift to implement, because both the substrate and the culture conditions must change drastically to accommodate 3D cell culture. This section will review some of the key developments in substrate design, and culture platform innovation that have facilitated development of 3D models. Further, recent applications of 3D tissue models to understanding cardiac cell therapy will be reviewed.

1.5.1 The Substrate

Cardiac cells, including fibroblasts, are anchorage-dependent, and therefore require a substrate for attachment to facilitate survival, activity, and proliferation. In the realm of tissue engineering there are currently four different approaches to providing a 3D substrate: (1) utilization of naturally occurring substrates from animals, (2) cell entrapment within hydrogels, (3) lamination of cell sheets with a self-assembled substrate, and (4) utilization of porous, engineered substrates [88-90]. Each of these approaches provides engineering control over two key substrate properties: (1) material composition (2) substrate microarchitecture, including porosity, alignment, and mechanical properties.

**1.5.1.1 Material Composition**

Evaluation of cardiac fibroblast (CFb) response to material composition in the literature is very limited. Exclusive cardiac fibroblast culture in 3D substrates are almost nonexistent. Most studies that have cultured CFb on different materials have included the CFb as part of a coculture including myocytes. Lasher et al. utilized fibrin gel to coculture cardiac myocytes and cardiac fibroblasts [91]. Vimentin staining revealed cardiac fibroblasts distributed between myocytes throughout the construct. These findings indicate that CFb are able to maintain vitality when cultured in serum containing DMEM-based media. Moreover, electrical stimulation did not appear to affect CFb numbers [91]. Freed et al. evaluated CFb cultured on a synthetic, elastomeric polymer substrate. Her group stained for F-actin in a mixed neonatal rat heart cell population. They observed that F-actin expressing cells (primarily CFb) filled the void spaces in porous poly (glycerol-

sebacate) substrates [57]. Our own group demonstrated that cardiac fibroblasts will attach and proliferate on poly (ether-urethane) substrates in serum containing media (See Chapter 3). Further we observed that cell attachment after perfusion seeding significantly increased with a composite fibronectin-coated polyurethane substrate (unpublished data).

#### 1.5.1.2 Architecture

Substrate microarchitecture profoundly influences cell response to the substrate. Further, substrate microarchitecture can be used to influence functional properties of the tissue model such as stiffness and hydraulic permeability. The geometric configuration of the substrate on the micro scale is determined by material fabrication and processing techniques. Therefore, a discussion of substrate design parameters must necessarily be coupled with a discussion of fabrication methods and techniques. The key architectural features that will be discussed here are: (1) porosity, (2) alignment/anisotropy, (3) stiffness, and (4) hydraulic permeability.

1.5.1.2.1 Porosity. Porosity is defined as the ratio of void space to total volume of a porous material. This parameter affects how much space is available for cells to occupy, diffusion of nutrients through the substrate matrix, and the effective mechanical properties of the construct [92]. Techniques for evaluating porosity include mercury-intrusion porosimetry, optical analysis, and gravimetric analysis (based on material densities). These methods provide insight to pore size, pore morphology, and porosity respectively. Electrospinning is common biomaterial fabrication technique for creating fibrous, nonwoven materials with fiber diameters typically on the order nanometers [93]. A polymer dissolved in solution is drawn through a charged spinneret to a conductive

surface by a high electrical potential, typically on the order of 10 kV [94, 95]. Baker et al. utilized an electrospinning approach to prepare fibrous of controlled porosity [96]. Sacrificial poly (ethylene oxide) (PEO) fibers were cospun with permanent poly (ε-caprolactone) fibers. After spinning, the PEO fibers were removed by ethanol immersion for 3 hrs, resulting in increased porosity that was dependent on the fraction of PEO fibers in the original material. Cell culture studies revealed that cell infiltration into the interior of the 3D substrate increased with increased fraction of sacrificial fibers [96]. Phase separation is a technique that is frequently used to fabricate porous biomaterials. This fabrication technique provides significantly more flexibility to the ability to control porosity of the resultant material. Rowlands et al. used a thermal phase separation (TIPS) technique to form polyurethane/PLGA substrates with pores ranging from 0.1-200 μm in diameter [97]. Woodhouse and colleagues created porous polyurethane substrates using TIPS. The resultant material was found to have nominal porosities ranging from 14% to 35% depending on fabrication conditions. When embryonic stem cell-derived cardiac cells were seeded onto these substrates, they were observed to infiltrate approximately 72 μm into the tissue, with significantly decreased numbers beyond this depth [98]. Another variant to the phase separation approach is the sprayed technique. In sprayed phased separation, two spray nozzles are simultaneously employed to deposit a solvent solution and nonsolvent onto a surface. Khorasani et al. described an elegant sprayed phase separation technique where porous substrates were fabricated by spraying onto a rotating mandrel. SEM was used to evaluate morphological changes that occurred in response to changes in the working distance of the spray nozzles and the speed of the mandrel [99]. Papenburg et al. took the phase separation fabrication techniques a step further. They

introduced a notable micromolding enhancement to the phase separation approach. This method utilizes a patterned substrate to provide geometric patterns to a thin sheet of phase separated material [100]. Moreover, they investigated the use of several different alcohols as nonsolvents in substrate formation. They determined that the type of alcohol affected porosity and pore structure. Using this method, they were able to independently control surface patterns of thin sheets through the mold geometry, and porosity through variation of the composition of the nonsolvent [100]. In addition to these approaches, Papenburg and colleagues also proposed, simultaneously to my own research, lamination of thin phase separated sheets to build thick 3D constructs [101].

Control over porosity has evolved from simple use of sacrificial components, to elegant physiochemical-control mechanisms that provide multiple levels of input and capabilities to substrate fabrication techniques. The work described herein utilizes a sprayed phase separation approach to substrate fabrication because of the high level of control over porosity and the ease of automation of this approach.

1.5.1.2.2 Alignment. Substrate alignment is a key feature that relates both to cell response and bulk mechanical properties. Contact guidance is a well established hypothesis that postulates that cells will be guided through contacting external geometric cues [102]. Using advanced quantification techniques [103], Freed and colleagues demonstrated that cardiac fibroblasts would align according to geometric cues of laser-ablated synthetic substrates [57]. Using micromolding techniques, Papenburg et al. demonstrated that cells can be aligned according to CAD-defined geometric patterns [100]. In Chapter 3, utilization of postspray elongation technique is discussed in detail

that provides alignment cues to fibroblasts. Further, a FFT-based method for assessing cellular alignment in response to the substrate is described.

1.5.1.2.3 Mechanical properties. Substrate mechanical properties are often key determinants of construct function. In addition, substrate mechanical properties can have profound effects on cellular activity [17, 104]. For soft tissue (such as cardiac tissue) tensile properties are of primary interest. In general, mechanical properties are measured through tensile testing, and normalization of the results. Cardiac tissue is a highly anisotropic tissue, meaning that, structural and functional parameters are inhomogeneous. Tensile properties of cardiac tissue are generally referred to in terms of the longitudinal or preferred modulus, and the transverse modulus. Several approaches to recapitulating the anisotropy of cardiac tissue in biomaterial substrates have been proposed. One method for controlling mechanical properties of cell substrate is through material composition. Zhang et al. developed custom polyurethane base formulations, and demonstrated different tensile properties over time base on material composition [105]. Rowlands et al. utilized different blends of polyurethane and PLGA, and demonstrated moduli ranging from 15 to 93 kPa depending on the material composition [97]. Geometric composition is another approach to control mechanical properties. Baker et al. achieved anisotropic geometry by electro-spinning onto a rotating mandrel to create fiber alignment. This fiber alignment resulted in an approximately 10-fold difference between the elastic modulus in the preferred direction and transverse direction [96]. Moroni et al. utilized a 3D fiber deposition approach controlled by CAD-CAM techniques to create substrates with geometrically controlled moduli ranging from 0.26 MPa to 13.7 MPa [106]. In Chapter 3, a postspray elongation technique is used to create geometric base

tensile anisotropy. This anisotropy is evaluated both optically through electron microscopy, and mechanically through tensile testing.

1.5.1.2.4 Hydraulic permeability. The last architectural feature of biomaterial for substrates that will be discussed here is hydraulic permeability. Hydraulic permeability is defined as the permeability of a porous medium to aqueous solutions. This architectural feature is of special interest to 3D cell culture because media perfusion is often used to enhance mass transport in the interior of thick substrates. Hydraulic permeability is measured by monitoring flow of media through a substrate while maintaining a constant head pressure. Hydraulic permeability, like mechanical properties, can be either isotropic, or anisotropic. Geometric features such as channels can be included in the porous matrix to influence hydraulic permeability [107-109]. Papenburg et al. utilized the micromolding approach to design corrugations into thin sheets which were then rolled up resulting in channel-like geometries running through the materials [110]. Chapter 4 includes a detailed discussion hydraulic permeability of various types of substrates including the substrate developed for use in this work.

## 1.5.2. Culture Conditions

Advances in design, processing, and fabrication of 3D substrates has necessitated concurrent advances in cell culture platforms. Native human tissue is sustained through a complex cooperation between multiple physiologic systems. As engineered tissues become more complex, the framework required to support the tissue will increase in complexity. Engineered tissue that is identical to native tissue will, by definition, require the same type of complex environmental support that is found in the body. The design of

advanced bioreactors and culture conditions is an essential step toward achieving more native like tissues.

In an important review, Barron et al. defines a bioreactor as "a system that simulates physiological environments for the creation, physical conditioning, and testing of cells, tissues, precursors, support structures, and organs *in vitro*" [111]. In the realm of cardiac tissue engineering, there are three important environmental conditions that can be simulated through utilization of bioreactors: mechanical stimulation, electrical stimulation, and enhanced metabolic exchange through perfusive flow [111]. In addition, an essential function of a bioreactor for evaluating 3D cardiac tissue is to support a uniform cell distribution throughout a 3D substrate [112, 113].

The greatest impediment to obtaining a uniform cell distribution in a 3D model is maintaining proper mass transport. Oxygen, nutrients, and metabolites must be brought near enough to cells to allow diffusive transport to exchange the spent resources with fresh ones. Convective fluid transport is the most versatile way of supplementing the transport capabilities of diffusion. Without convective supplementation, diffusion can only provide support to cardiac tissue that is ~100 μm thick [114]. In a mathematical model of oxygen transport and consumption, Radisic et al. demonstrated that perfusion of a channeled substrate can provide sufficient oxygen to support a 2 mm thick construct that is densely packed with cardiac cells [115]. In an *in vitro* model, Carrier et al. demonstrated that perfusion increased spatial uniformity of cardiac cells in a synthetic 3D substrate [116]. Liu and colleagues demonstrated that perfusion significantly increased the number of cells on an elastomeric polyurethane substrate when compared to static controls [117]. Moreover, perfusion provides important stimuli to cardiac cells. Maidhof

and colleagues showed that excitation threshold increased significantly without perfusion or electrical stimulation [118].

There are two distinct phases that occur during perfusion culture that influence cell distribution: seeding and steady state culture. The seeding phase of culture occurs in the beginning to help cells attach to the substrate. In a 3D substrate, efficient seeding is necessary to ensure that cells are anchored uniformly throughout the material. Maidhof et al. explored the important seeding parameters in elastomeric channeled substrates. They determined that flow velocity and duration of seeding of cardiac myocytes are important seeding parameters [108]. They evaluated seeding velocities ranging from 6 mm/min to 60 mm/min. They determined the highest flow (60 mm/min) resulted in the highest seeding efficiency (87%). When they investigated how long to maintain the seeding velocity, they found that 2 hrs provided a higher seeding efficiency than 1 hr. During the steady state culture phase, the flow velocity is the primary perfusion parameter. McCoy et al. developed a mathematical model to understand the effect of flow rate on cell attachment in a bioreactor [119]. Under high flow conditions, cells were detached from the substrate surface by the flow-induced shear stress. The work of McCoy et al. and Maidhof et al. help establish general constraints for seeding and steady state perfusion parameters: high velocity is good for a limited duration while cells are attaching, but lower velocities are better long term to prevent cells from detaching.

### 1.5.3 3D Cell Culture Applications

3D cell culture is only possible through the use of appropriate substrates and culture platforms. Development of 3D culture techniques, while challenging, has been

primarily motivated by two different potential applications: therapeutic use of 3D cell culture (engineered tissue) to treat diseased or damaged tissue [88, 120, 121], and utilization of advanced cell culture as a bridge between 2D *in vitro* and *in vivo* testing [87, 122, 123].

Many of the design requirements for engineered tissue and 3D models overlap, however, there are fundamental differences. For example, cell culture models do not have the stringent requirements for systemic biocompatibility that are necessary for implanted tissues. While this can simplify some aspects of the design, the advantage is tempered by inability of *in vitro* models to undergo modification after implantation. For example, one approach to creating therapeutic engineered tissue relies on *in vitro* angiogenesis to provide vascularization [124, 125]. 3D models, on the other hand, will undergo angiogenesis and vascularization only if the culture conditions are designed specifically for this purpose.

At the present, there has been only one attempt at developing 3D cardiac fibroblast models. Gaile et al. seeded CFb into collagen gels that were either free floating, or constrained at the edges and observed changes in mRNA levels of collagen (type I and III), TGF-β, and α-smooth muscle actin (α-SMA) [17]. No changes in collagen or TGF-β expression were detected. A significant increase in α-SMA was detected at 6 and 24 hrs, but became nonsignificant after 48 hrs. Further Gaile and colleagues monitored the stiffness of the constructs after 6 hrs and 120 hrs. They noted that the elastic modulus was similar to fibrotic cardiac tissue after 120 hrs and proposed that a 3D cell model of cardiac fibroblasts could be used to better understand fibrosis in the heart [17].

While engineered tissue models have primarily been focused on cardiac myocytes, some models have been developed that utilize a mixed cell population of both myocytes and fibroblasts. Freed and colleagues demonstrated that coculture of myocytes and CFb resulted in higher levels of MMP 2 expression than CM enriched populations [126]. In another study, Freed and colleagues observed that cardiac fibroblasts when cocultured with myocytes aligned to match scaffold geometry [57].

Beyond the scope of cardiac fibroblasts, the concept of a 3D *in vitro* model for evaluating stem cell therapy has been pioneered by Radisic and colleagues [6]. Using a collagen sponge substrate and an electrical stimulation bioreactor, Song et al. investigated the functional integration of injected stem cells and surrogate heart tissue. They observed that embryonic stem cell derived cardiomyocytes (ESC-CM) cultured in low glucose were able to significantly improve the excitation threshold of the surrogate cardiac tissue [7]. On the other hand, these same cells also decreased the maximum rate of synchronous contraction of these constructs. In another important study, Radisic's group used surrogate cardiac tissue to understand embryonic stem cell (ESC) response to a cardiac environment [8]. They observed that ESC can survive and even proliferate in a cardiac environment. Despite this initial positive finding, they also observed that ESC did not functionally integrate with the surrogate heart tissue. The findings of these landmark studies have pushed researchers to look for other potential mechanisms of cardiac regeneration through cell therapy, and demonstrate the utility of 3D cell models in evaluating and designing stem cell therapies.

The last type of *in vitro* 3D model that will be discussed here is explanted cardiac tissue models. Pillenkamp developed a model of cardiac tissue by explanting and

sectioning murine hearts. These 300 μm thick slices of cardiac tissue were functionally maintained using static cell culture techniques for up to 24 hrs before evidence of apoptosis became evident [127]. These models were used to assess the influence of ESC-CM injection on force of contraction of the tissue [127]. The results indicated that ESC-CM injection improved contractile force of the constructs. Pillenkamp et al., like Radisic's group, observed that ESC-CM did not functionally integrate with surrounding cardiac tissue [128]. Another group modified the tissue slice model by utilizing a gas-liquid interface bioreactor to increase the time that the tissue slice could survive *ex vivo* [129]. The gas-liquid interface culture platform allowed Habeler and colleagues to functionally preserve the tissue slice for up to 80 days. Further application of this model demonstrated that 60 days after injection, ESC in the heart slice had adapted a cardiac myocyte like phenotype [130].

The future of more complex experimental treatments for heart failure will rely on better methods to understand these treatments. Models like surrogate heart tissue and heart slices have demonstrated their ability to make a significant impact on the development of novel treatments however, these models rely on complex substrates, and advanced bioreactors to simulate the necessary environmental signals. Further expansion of 3D tissue models to include cardiac fibroblasts will broaden our capacity to evaluate the next generation of treatments for chronic heart disease.

## 1.6 Summary, Overview, and Contributions

There is an important opportunity for advanced cell culture platforms to make a significant impact on the standard treatment of heart failure by helping successfully

design stem cell therapy treatments. In this chapter the physiologic role of the cardiac fibroblast, the impetus and mechanics of heart failure, cardiac cell therapy, and state-of-the-art cell culture and tissue engineering models were reviewed. The overarching objective of the research described in this dissertation was to directly correlate MSC treatment with CFb mediated changes in stiffness. This objective was addressed through the development of culture materials, a specialized bioreactor and utilization of newly developed methods to coculture fibroblasts and MSCs.

In Chapter 2 the design requirements and specifications for foundational equipment used in all further chapters are described. Chapter 2 includes a description of pertinent design spray parameters, as well as the mechanical design for the spray assembly and substrate fixturing.

In Chapter 3, novel methods for fabricating a porous polyurethane substrate that mimics the mechanical anisotropy of ventricular heart tissue are described. Dual spray nozzles were mounted onto a three axis computer numeric control robot (see appendix A for engineering drawings of spray platform). An elastomeric poly(ether-urethane) dissolved in N-dimethylacetamide (DMAc) was sprayed through one nozzle while a water-alcohol mixture serving as the nonsolvent was sprayed simultaneously through the other. The polymer begins to precipitate on the spray substrate as the solvent is diluted in the nonsolvent. After spray deposition, the biomaterial was uniaxially strained in custom frames that held the material in an elongated conformation during the curing period. After 24 hrs the biomaterial had relaxed and cured sufficiently to be removed from the frames while permanently maintaining the elongated architecture. Electron microscopy, gravimetric porosity analysis, and mechanical testing were used to evaluate the

architecture of the biomaterial. To validate that the architecture observed through characterization testing would influence cell behavior, 3T3 murine dermal fibroblasts were seeded and cultured on 250 μm thick sheets. A two-dimensional fast fourier transform (2D FFT) was used to evaluate cell alignment with the direction of postspray elongation. Fibroblasts were observed to increase alignment of cytoskeletal actin filaments as the degree of postspray elongation increased. To demonstrate further flexibility of the substrate, multiple thin sheets were laminated after spraying. After the curing period, thick robust sheets were observed with little discernible evidence of lamination boundaries when imaged with an electron microscope.

In Chapter 4 two different methods for supporting cell populations in the interior of a 1 mm thick laminated substrate were developed and evaluated: (1) development of channel-like features running along the length of the substrate, and (2) development of perfusion seeding and culture. Phase separation molding techniques were adapted to the sprayed phase separation technique described in Chapter 3. Computer aided design (CAD) techniques and rapid stereo-lythographic prototyping were employed to fabricate corrugated spray substrates. Sprayed phase separation of the polymer onto this surface yielded reciprocal corrugations on one surface of the porous polyurethane material. Electron microscopy characterization confirmed that the corrugation pattern closely resembled the CAD pattern. Lamination of six corrugated sheets created a composite substrate approximately 1 mm thick with channel-like features arrayed in parallel along the length of the material. Hydraulic permeability testing confirmed the functional performance of the channels. One of the fundamental limitations of 3D materials for cell culture is inadequate mass transport near the cells. A perfusion bioreactor was design to

allow continuous perfusion through the channels and porous matrix of the substrate. Human mesenchymal stem cells were seeded either using a surface or perfusion approach. Following a 7 day culture period, cellularized samples were evaluated for cell density and cell distribution. Perfusion seeding and culture were observed to increase cell density and provide a more homogenous distribution of cells through the substrate. The presence of channel-like features in the substrate increased cell density in perfusion seeded samples when compared to nonchanneled materials.

In Chapter 5, the perfusion culture system was modified and utilized in conjunction with the channeled substrate to evaluate the effect of MSC coculture on CFb-mediated changes in stiffness. Appendix B contains engineering drawings and design considerations for the individual perfusion cassette cell culture platform used in Chapter 5. Chapter 5 first describes design and validation of the culture platform. Dermal fibroblasts were used to evaluate fibronectin preconditioning of the substrate and optimize seeding flow velocity for cell density and distribution. Cardiac fibroblasts were then used in a second seeding optimization investigation seeding velocity and duration. The purpose of the culture platform is to allow direct evaluation of treatment induced changes in stiffness. To validate that the model is capable of detecting increases in stiffness, dermal fibroblasts were cultured with and without ascorbic acid. Stiffness assessment demonstrated a significant increase between acellular substrates and fibroblast seeded constructs, and again between fibroblast seeded constructs without ascorbic acid supplementation, and constructs with ascorbic acid supplementation. To validate that the model was capable of detecting treatment induced decreases in stiffness, a common ACE inhibitor that has been shown to inhibit fibroblast mediated fibrosis was

used to treat cardiac fibroblast seeded constructs. After cell culture, the stiffness of the ACE inhibitor treated group was significantly less stiff than untreated CFb group. To test whether MSC coculture influence stiffness, CFb and MSC were cultured together on the substrate. End-point stiffness assessment revealed that MSC coculture resulted in increased stiffness. Confocal imaging revealed that MSC were present and type III collagen was expressed in higher abundance in the coculture samples.

Chapter 6 discusses the conclusions from this work, specifically that MSC increase construct stiffness when cocultured with CFb. These findings seem to indicate that clinical application of MSC to alter is stiffness is a feasible approach to treating passive biomechanical heart pathologies. Moreover, future development of stem cell and pharmacologic therapeutics be evaluated using the model platform described in this work to quantitatively evaluate treatment induced changes in stiffness.

### 1.6.1 Contributions

Chapters 3 and 4 are comprised of multiple author peer-reviewed publications. In Chapter 3 James Kennedy, Sean McCandless, and Robert Hitchcock were responsible for conception, design of the study, and experiments. Richard Lasher and James Kennedy were responsible for development of image analysis algorithms. James Kennedy analyzed the data and primarily wrote the manuscript. Robert Hitchcock, Sean McCandless, and Richard Lasher assisted in writing and provided critical review of the manuscript. All authors approved the final version of the manuscript.

In Chapter 4, James Kennedy, Sean McCandless, Asad Rauf, and Robert Hitchcock were responsible for conception, design of the study, and experiments. James

Kennedy, Jennifer Hillam and Laura Williams performed cell culture experiments. James Kennedy analyzed the data and primarily wrote the manuscript. Sean McCandless, Asad Rauf, and Robert Hitchcock assisted in writing and provided critical review of the manuscript. All authors approved the final version of the manuscript.

## 1.7 References

[1] Lloyd-Jones D, Adams RJ, Brown TM, Carnethon M, Dai S, De Simone G, et al. Heart disease and stroke statistics--2010 update: a report from the American Heart Association. Circulation. 2010;121:e46-e215.

[2] Segers VF, Lee RT. Stem-cell therapy for cardiac disease. Nature. 2008;451:937-42.

[3] Dai W, Hale SL, Martin BJ, Kuang JQ, Dow JS, Wold LE, et al. Allogeneic mesenchymal stem cell transplantation in postinfarcted rat myocardium: short- and long-term effects. Circulation. 2005;112:214-23.

[4] Mias C, Lairez O, Trouche E, Roncalli J, Calise D, Seguelas MH, et al. Mesenchymal stem cells promote matrix metalloproteinase secretion by cardiac fibroblasts and reduce cardiac ventricular fibrosis after myocardial infarction. Stem Cells. 2009;27:2734-43.

[5] Menasche P. Cardiac cell therapy: lessons from clinical trials. J Mol Cell Cardiol. 2010;50:258-65.

[6] Nunes SS, Song H, Chiang CK, Radisic M. Stem cell-based cardiac tissue engineering. J Cardiovasc Transl Res. 2011;4:592-602.

[7] Song H, Yoon C, Kattman SJ, Dengler J, Masse S, Thavaratnam T, et al. Interrogating functional integration between injected pluripotent stem cell-derived cells and surrogate cardiac tissue. Proc Natl Acad Sci U S A. 2010;107:3329-34.

[8] Dengler J, Song H, Thavandiran N, Masse S, Wood GA, Nanthakumar K, et al. Engineered heart tissue enables study of residual undifferentiated embryonic stem cell activity in a cardiac environment. Biotechnol Bioeng. 2011;108:704-19.

[9] Nag AC. Study of non-muscle cells of the adult mammalian heart: a fine structural analysis and distribution. Cytobios. 1980;28:41-61.

[10] Camelliti P, Borg TK, Kohl P. Structural and functional characterisation of cardiac fibroblasts. Cardiovasc Res. 2005;65:40-51.

[11] Goldsmith EC, Hoffman A, Morales MO, Potts JD, Price RL, McFadden A, et al. Organization of fibroblasts in the heart. Dev Dyn. 2004;230.

[12] Duffy HS. Fibroblasts, myofibroblasts, and fibrosis: fact, fiction, and the future. J Cardiovasc Pharmacol. 2011;57:373-5.

[13] Agocha A, Sigel AV, Eghbali-Webb M. Characterization of adult human heart fibroblasts in culture: a comparative study of growth, proliferation and collagen production in human and rabbit cardiac fibroblasts and their response to transforming growth factor-beta1. Cell Tissue Res. 1997;288:87-93.

[14] Curtis MW, Russell B. Micromechanical regulation in cardiac myocytes and fibroblasts: implications for tissue remodeling. Pflugers Arch. 2011;462:105-17.

[15] Gabbiani G, Ryan GB, Majne G. Presence of modified fibroblasts in granulation tissue and their possible role in wound contraction. Experientia. 1971;27:549-50.

[16] Daskalopoulos EP, Janssen BJ, Blankesteijn WM. Myofibroblasts in the infarct area: concepts and challenges. Microsc Microanal. 2012;18:35-49.

[17] Galie PA, Westfall MV, Stegemann JP. Reduced serum content and increased matrix stiffness promote the cardiac myofibroblast transition in 3D collagen matrices. Cardiovasc Pathol. 2011;20:325-33.

[18] Wang H, Haeger SM, Kloxin AM, Leinwand LA, Anseth KS. Redirecting valvular myofibroblasts into dormant fibroblasts through light-mediated reduction in substrate modulus. PLoS One. 2012;7:e39969.

[19] Weber KT, Sun Y, Bhattacharya SK, Ahokas RA, Gerling IC. Myofibroblast-mediated mechanisms of pathological remodelling of the heart. Nat Rev Cardiol. 2013;10:15-26.

[20] Yamamoto K, Masuyama T, Sakata Y, Nishikawa N, Mano T, Yoshida J, et al. Myocardial stiffness is determined by ventricular fibrosis, but not by compensatory or excessive hypertrophy in hypertensive heart. Cardiovasc Res. 2002;55:76-82.

[21] Eghbali M, Robinson TF, Seifter S, Blumenfeld OO. Collagen accumulation in heart ventricles as a function of growth and aging. Cardiovascular Res. 1989;23:723-9.

[22] Leonard BL, Smaill BH, Legrice IJ. Structural remodeling and mechanical function in heart failure. Microsc Microanal. 2012;18:50-67.

[23] Webb K, Hitchcock RW, Smeal RM, Li W, Gray SD, Tresco PA. Cyclic strain increases fibroblast proliferation, matrix accumulation, and elastic modulus of fibroblast-seeded polyurethane constructs. J Biomech. 2006;39:1136-44.

[24] Turner NA, Porter KE. Regulation of myocardial matrix metalloproteinase expression and activity by cardiac fibroblasts. IUBMB Life. 2012;64:143-50.

[25] Foronjy RF, Sun J, Lemaitre V, D'Armiento JM. Transgenic expression of matrix metalloproteinase-1 inhibits myocardial fibrosis and prevents the transition to heart failure in a pressure overload mouse model. Hypertens Res. 2008;31:725-35.

[26] Hayashidani S, Tsutsui H, Ikeuchi M, Shiomi T, Matsusaka H, Kubota T, et al. Targeted deletion of MMP-2 attenuates early LV rupture and late remodeling after experimental myocardial infarction. Am J Physiol Heart Circ Physiol. 2003;285:H1229-35.

[27] Spinale FG, Mukherjee R, Zavadzkas JA, Koval CN, Bouges S, Stroud RE, et al. Cardiac restricted overexpression of membrane type-1 matrix metalloproteinase causes adverse myocardial remodeling following myocardial infarction. J Biol Chem. 2010;285:30316-27.

[28] Limana F, Esposito G, D'Arcangelo D, Di Carlo A, Romani S, Melillo G, et al. HMGB1 Attenuates Cardiac Remodelling in the Failing Heart via Enhanced Cardiac Regeneration and miR-206-Mediated Inhibition of TIMP-3. PLoS One. 2011;6:e19845.

[29] Vanhoutte D, Heymans S. TIMPs and cardiac remodeling: 'Embracing the MMP-independent-side of the family'. J Mol Cell Cardiol. 2009;48:445-53.

[30] Liu H, Chen SE, Jin B, Carson JA, Niu A, Durham W, et al. TIMP3: a physiological regulator of adult myogenesis. J Cell Sci. 2010;123:2914-21.

[31] Molnar J, Fong KS, He QP, Hayashi K, Kim Y, Fong SF, et al. Structural and functional diversity of lysyl oxidase and the LOX-like proteins. Biochim Biophys Acta. 2003;1647:220-4.

[32] Lopez B, Gonzalez A, Hermida N, Valencia F, de Teresa E, Diez J. Role of lysyl oxidase in myocardial fibrosis: from basic science to clinical aspects. Am J Physiol Heart Circ Physiol. 2010;299:H1-9.

[33] Voloshenyuk TG, Hart AD, Khoutorova E, Gardner JD. TNF-alpha increases cardiac fibroblast lysyl oxidase expression through TGF-beta and PI3Kinase signaling pathways. Biochem Biophys Res Commun. 2011;413:370-5.

[34] Lee AA, Dillmann WH, McCulloch AD, Villarreal FJ. Angiotensin II stimulates the autocrine production of transforming growth factor-beta 1 in adult rat cardiac fibroblasts. J Mol Cell Cardiol. 1995;27:2347-57.

[35] Yokoyama T, Sekiguchi K, Tanaka T, Tomaru K, Arai M, Suzuki T, et al. Angiotensin II and mechanical stretch induce production of tumor necrosis factor in cardiac fibroblasts. Am J Physiol. 1999;276:H1968-76.

[36] Ancey C, Corbi P, Froger J, Delwail A, Wijdenes J, Gascan H, et al. Secretion of IL-6, IL-11 and LIF by human cardiomyocytes in primary culture. Cytokine. 2002;18:199-205.

[37] Turner NA, Das A, O'Regan DJ, Ball SG, Porter KE. Human cardiac fibroblasts express ICAM-1, E-selectin and CXC chemokines in response to proinflammatory cytokine stimulation. Int J Biochem Cell Biol. 2011;43:1450-8.

[38] Wang JH, Lin JS. Cell traction force and measurement methods. Biomechanics and Modeling in Mechanobiology. 2007;6:361-71.

[39] Bell E, Ivarsson B, Merrill C. Production of a tissue-like structure by contraction of collagen lattices by human fibroblasts of different proliferative potential in vitro. Proc Natl Acad Sci U S A. 1979;76:1274-8.

[40] Nusgens B, Merrill C, Lapiere C, Bell E. Collagen biosynthesis by cells in a tissue equivalent matrix in vitro. Collagen and Related Research. 1984;4:351-63.

[41] Coulomb B, Dubertet L, Merrill C, Touraine R, Bell E. The collagen lattice: a model for studying the physiology, biosynthetic function and pharmacology of the skin. The British Journal of Dermatology. 1984;111 Suppl 27:83-7.

[42] Grinnell F. Fibroblasts, myofibroblasts, and wound contraction. J Cell Biol. 1994;124:401-4.

[43] Grinnell F. Fibroblast-collagen-matrix contraction: growth-factor signalling and mechanical loading. Trends in Cell Biology. 2000;10:362-5.

[44] Grinnell F. Fibroblast biology in three-dimensional collagen matrices. Trends in Cell Biology. 2003;13:264-9.

[45] Rhee S, Grinnell F. Fibroblast mechanics in 3D collagen matrices. Advanced Drug Delivery Reviews. 2007;59:1299-305.

[46] Grinnell F. Fibroblast mechanics in three-dimensional collagen matrices. Journal of Bodywork and Movement Therapies. 2008;12:191-3.

[47] Harris AK, Wild P, Stopak D. Silicone rubber substrata: a new wrinkle in the study of cell locomotion. Science. 1980;208:177-9.

[48] Beningo KA, Wang YL. Flexible substrata for the detection of cellular traction forces. Trends in Cell Biology. 2002;12:79-84.

[49] Pelham RJ, Jr., Wang Y. Cell locomotion and focal adhesions are regulated by substrate flexibility. Proc Natl Acad Sci U S A. 1997;94:13661-5.

[50] du Roure O, Saez A, Buguin A, Austin RH, Chavrier P, Silberzan P, et al. Force mapping in epithelial cell migration. Proc Natl Acad Sci U S A. 2005;102:2390-5.

[51] MacKenna DA, Omens JH, McCulloch AD, Covell JW. Contribution of collagen matrix to passive left ventricular mechanics in isolated rat hearts. Am J Physiol. 1994;266:H1007-18.

[52] Sasaki N, Odajima S. Stress-strain curve and Young's modulus of a collagen molecule as determined by the X-ray diffraction technique. J Biomech. 1996;29:655-8.

[53] Christiansen DL, Huang EK, Silver FH. Assembly of type I collagen: fusion of fibril subunits and the influence of fibril diameter on mechanical properties. Matrix Biology : Journal of the International Society for Matrix Biology. 2000;19:409-20.

[54] Robinson TF, Geraci MA, Sonnenblick EH, Factor SM. Coiled perimysial fibers of papillary muscle in rat heart: morphology, distribution, and changes in configuration. Circ Res. 1988;63:577-92.

[55] MacKenna DA, Omens JH, Covell JW. Left ventricular perimysial collagen fibers uncoil rather than stretch during diastolic filling. Basic Res Cardiol. 1996;91:111-22.

[56] MacKenna DA, Vaplon SM, McCulloch AD. Microstructural model of perimysial collagen fibers for resting myocardial mechanics during ventricular filling. Am J Physiol. 1997;273:H1576-86.

[57] Engelmayr GC, Jr., Cheng M, Bettinger CJ, Borenstein JT, Langer R, Freed LE. Accordion-like honeycombs for tissue engineering of cardiac anisotropy. Nat Mater. 2008;7:1003-10.

[58] Lloyd-Jones D, Adams R, Carnethon M, De Simone G, Ferguson TB, Flegal K, et al. Heart disease and stroke statistics--2009 update: a report from the American Heart Association Statistics Committee and Stroke Statistics Subcommittee. Circulation. 2009;119:480-6.

[59] Cutler MJ, Rosenbaum DS, Dunlap ME. Structural and electrical remodeling as therapeutic targets in heart failure. J Electrocardiol. 2007;40:S1-7.

[60] Brower GL, Gardner JD, Forman MF, Murray DB, Voloshenyuk T, Levick SP, et al. The relationship between myocardial extracellular matrix remodeling and ventricular function. Eur J Cardiothorac Surg. 2006;30:604-10.

[61] Connelly CM, Vogel WM, Wiegner AW, Osmers EL, Bing OH, Kloner RA, et al. Effects of reperfusion after coronary artery occlusion on post-infarction scar tissue. Circ Res. 1985;57:562-77.

[62] Gorman RC, Jackson BM, Burdick JA, Gorman JH. Infarct restraint to limit adverse ventricular remodeling. J Cardiovasc Transl Res. 2011;4:73-81.

[63] Pfeffer MA, Braunwald E. Ventricular remodeling after myocardial infarction. Experimental observations and clinical implications. Circulation. 1990;81:1161-72.

[64] Udelson JE, Konstam MA. Relation between left ventricular remodeling and clinical outcomes in heart failure patients with left ventricular systolic dysfunction. J Card Fail. 2002;8:S465-71.

[65] Holmes JW, Borg TK, Covell JW. Structure and mechanics of healing myocardial infarcts. Annu Rev Biomed Eng. 2005;7:223-53.

[66] Forrester JS, White AJ, Matsushita S, Chakravarty T, Makkar RR. New paradigms of myocardial regeneration post-infarction: tissue preservation, cell environment, and pluripotent cell sources. JACC Cardiovasc Interv. 2009;2:1-8.

[67] Sunagawa K, Maughan WL, Sagawa K. Effect of regional ischemia on the left ventricular end-systolic pressure-volume relationship of isolated canine hearts. Circ Res. 1983;52:170-8.

[68] Gupta KB, Ratcliffe MB, Fallert MA, Edmunds LH, Jr., Bogen DK. Changes in passive mechanical stiffness of myocardial tissue with aneurysm formation. Circulation. 1994;89:2315-26.

[69] Wilson EM, Moainie SL, Baskin JM, Lowry AS, Deschamps AM, Mukherjee R, et al. Region- and type-specific induction of matrix metalloproteinases in post-myocardial infarction remodeling. Circulation. 2003;107:2857-63.

[70] Takahashi S, Barry AC, Factor SM. Collagen degradation in ischaemic rat hearts. Biochem J. 1990;265:233-41.

[71] Janicki JS, Brower GL, Henegar JR, Wang L. Ventricular remodeling in heart failure: the role of myocardial collagen. Adv Exp Med Biol. 1995;382:239-45.

[72] Cleutjens JP, Verluyten MJ, Smiths JF, Daemen MJ. Collagen remodeling after myocardial infarction in the rat heart. Am J Pathol. 1995;147:325-38.

[73] Norton GR, Tsotetsi J, Trifunovic B, Hartford C, Candy GP, Woodiwiss AJ. Myocardial stiffness is attributed to alterations in cross-linked collagen rather than total collagen or phenotypes in spontaneously hypertensive rats. Circulation. 1997;96:1991-8.

[74] Woodiwiss AJ, Tsotetsi OJ, Sprott S, Lancaster EJ, Mela T, Chung ES, et al. Reduction in myocardial collagen cross-linking parallels left ventricular dilatation in rat models of systolic chamber dysfunction. Circulation. 2001;103:155-60.

[75] Sun Y, Weber KT. Infarct scar: a dynamic tissue. Cardiovasc Res. 2000;46:250-6.

[76] Passier R, van Laake LW, Mummery CL. Stem-cell-based therapy and lessons from the heart. Nature. 2008;453:322-9.

[77] Sawa Y, Miyagawa S, Sakaguchi T, Fujita T, Matsuyama A, Saito A, et al. Tissue engineered myoblast sheets improved cardiac function sufficiently to discontinue LVAS in a patient with DCM: report of a case. Surg Today. 2012;42:181-4.

[78] Menasche P. Stem cell therapy for chronic heart failure: lessons from a 15-year experience. C R Biol. 2011;334:489-96.

[79] Godier-Furnemont AF, Martens TP, Koeckert MS, Wan L, Parks J, Arai K, et al. Composite scaffold provides a cell delivery platform for cardiovascular repair. Proc Natl Acad Sci U S A. 2011;108:7974-9.

[80] Lian WS, Cheng WT, Cheng CC, Hsiao FS, Chen JJ, Cheng CF, et al. In vivo therapy of myocardial infarction with mesenchymal stem cells modified with prostaglandin I synthase gene improves cardiac performance in mice. Life Sci. 2011;88:455-64.

[81] Gnecchi M, He H, Liang OD, Melo LG, Morello F, Mu H, et al. Paracrine action accounts for marked protection of ischemic heart by Akt-modified mesenchymal stem cells. Nat Med. 2005;11:367-8.

[82] Moreno-Gonzalez A, Korte FS, Dai J, Chen K, Ho B, Reinecke H, et al. Cell therapy enhances function of remote non-infarcted myocardium. J Mol Cell Cardiol. 2009;47:603-13.

[83] Chimenti I, Smith RR, Li TS, Gerstenblith G, Messina E, Giacomello A, et al. Relative roles of direct regeneration versus paracrine effects of human cardiosphere-derived cells transplanted into infarcted mice. Circ Res. 2010;106:971-80.

[84] Hamdi H, Planat-Benard V, Bel A, Puymirat E, Geha R, Pidial L, et al. Epicardial adipose stem cell sheets results in greater post-infarction survival than intramyocardial injections. Cardiovasc Res. 2010;93:483-91.

[85] Bel A, Planat-Bernard V, Saito A, Bonnevie L, Bellamy V, Sabbah L, et al. Composite cell sheets: a further step toward safe and effective myocardial regeneration by cardiac progenitors derived from embryonic stem cells. Circulation. 2010;122:S118-23.

[86] Vunjak-Novakovic G, Tandon N, Godier A, Maidhof R, Marsano A, Martens T, et al. Challenges in Cardiac Tissue Engineering. Tissue Engineering Part B: Reviews. 2009:140-568.

[87] Hollister S, Wang Y, Wang G, Chen L, Li H, Yin T, et al. Scaffold engineering: a bridge to where? Biofabrication. 2009;1:012001-14.

[88] Eschenhagen T, Zimmermann WH. Engineering myocardial tissue. Circ Res. 2005;97:1220-31.

[89] Naito H, Melnychenko I, Didie M, Schneiderbanger K, Schubert P, Rosenkranz S, et al. Optimizing engineered heart tissue for therapeutic applications as surrogate heart muscle. Circulation. 2006;114:I72-8.

[90] Zimmermann WH, Cesnjevar R. Cardiac tissue engineering: implications for pediatric heart surgery. Pediatr Cardiol. 2009;30:716-23.

[91] Lasher RA, Pahnke AQ, Johnson JM, Sachse FB, Hitchcock RW. Electrical stimulation directs engineered cardiac tissue to an age-matched native phenotype. J Tissue Eng. 2012;3:1-15.

[92] Hollister SJ. Porous scaffold design for tissue engineering. Nat Mater. 2005;4:518-24.

[93] Huang Z, Zhang Y, Kotaki M, Ramakrishna S. A review on polymer nanofibers by electrospinning and their applications in nanocomposites. Composites Science and Technology. 2003;63:2223-53.

[94] Doshi J, Reneker D. Electrospinning process and applications of electrospun fibers. Journal of Electrostatics. 1995;35:151-60.

[95] Reneker D, Yarin A. Electrospinning jets and polymer nanofibers. Polymer. 2008;49:2387-425.

[96] Baker BM, Gee AO, Metter RB, Nathan AS, Marklein RA, Burdick JA, et al. The potential to improve cell infiltration in composite fiber-aligned electrospun scaffolds by the selective removal of sacrificial fibers. Biomaterials. 2008;29:2348-58.

[97] Rowlands AS, Lim SA, Martin D, Cooper-White JJ. Polyurethane/poly(lactic-co-glycolic) acid composite scaffolds fabricated by thermally induced phase separation. Biomaterials. 2007;28:2109-21.

[98] Fromstein JD, Zandstra PW, Alperin C, Rockwood D, Rabolt JF, Woodhouse KA. Seeding bioreactor-produced embryonic stem cell-derived cardiomyocytes on different porous, degradable, polyurethane scaffolds reveals the effect of scaffold architecture on cell morphology. Tissue Eng Part A. 2008;14:369-78.

[99] Khorasani MT, Shorgashti S. Fabrication of microporous polyurethane by spray phase inversion method as small diameter vascular grafts material. J Biomed Mater Res A. 2006;77:253-60.

[100] Papenburg B, Vogelaar L, Bolhuis-Versteeg L, Lammertink R, Stamatialis D, Wessling M. One-step fabrication of porous micropatterned scaffolds to control cell behavior. Biomaterials. 2007;28:1998-2009.

[101] Papenburg BJ, Liu J, Higuera GA, Barradas AM, de Boer J, van Blitterswijk CA, et al. Development and analysis of multi-layer scaffolds for tissue engineering. Biomaterials. 2009;30:6228-39.

[102] Guido S, Tranquillo RT. A methodology for the systematic and quantitative study of cell contact guidance in oriented collagen gels. Correlation of fibroblast orientation and gel birefringence. J Cell Sci. 1993;105 ( Pt 2):317-31.

[103] Ayres CE, Jha BS, Meredith H, Bowman JR, Bowlin GL, Henderson SC, et al. Measuring fiber alignment in electrospun scaffolds: a user's guide to the 2D fast Fourier transform approach. J Biomater Sci Polym Ed. 2008;19:603-21.

[104] Marsano A, Maidhof R, Wan LQ, Wang Y, Gao J, Tandon N, et al. Scaffold stiffness affects the contractile function of three-dimensional engineered cardiac constructs. Biotechnol Prog. 2010;26:1382-90.

[105] Zhang C, Wen X, Vyavahare NR, Boland T. Synthesis and characterization of biodegradable elastomeric polyurethane scaffolds fabricated by the inkjet technique. Biomaterials. 2008;29:3781-91.

[106] Moroni L, de Wijn JR, van Blitterswijk CA. 3D fiber-deposited scaffolds for tissue engineering: influence of pores geometry and architecture on dynamic mechanical properties. Biomaterials. 2006;27:974-85.

[107] Zhang T, Wan LQ, Xiong Z, Marsano A, Maidhof R, Park M, et al. Channelled scaffolds for engineering myocardium with mechanical stimulation. J Tissue Eng Regen Med. 2011;6:748-56.

[108] Maidhof R, Marsano A, Lee EJ, Vunjak-Novakovic G. Perfusion seeding of channeled elastomeric scaffolds with myocytes and endothelial cells for cardiac tissue engineering. Biotechnol Prog. 2010;26:565-72.

[109] Kaihara S, Borenstein J, Koka R, Lalan S, Ochoa E, Ravens M, et al. Silicon micromachining to tissue engineer branched vascular channels for liver fabrication. Tissue Engineering. 2000;6:105-17.

[110] Papenburg BJ, Bolhuis-Versteeg LA, Grijpma DW, Feijen J, Wessling M, Stamatialis D. A Facile Method to Fabricate Poly(L-lactide) Nano-fibrous Morphologies by Phase Inversion. Acta Biomater. 2010;6:2477-83.

[111] Barron V, Lyons E, Stenson-Cox C, McHugh PE, Pandit A. Bioreactors for cardiovascular cell and tissue growth: a review. Ann Biomed Eng. 2003;31:1017-30.

[112] Freed LE, Vunjak-Novakovic G. Tissue engineering bioreactors. Principles of Tissue Engineering. 2000;2:143-56.

[113] Thevenot P, Nair A, Dey J, Yang J, Tang L. Method to Analyze Three-Dimensional Cell Distribution and Infiltration in Degradable Scaffolds. Tissue Engineering Part A. 2008;14:319-31.

[114] Radisic M, Marsano A, Maidhof R, Wang Y, Vunjak-Novakovic G. Cardiac tissue engineering using perfusion bioreactor systems. Nat Protoc. 2008;3:719-38.

[115] Radisic M, Deen W, Langer R, Vunjak-Novakovic G. Mathematical model of oxygen distribution in engineered cardiac tissue with parallel channel array perfused

with culture medium containing oxygen carriers. American Journal of Physiology-Heart and Circulatory Physiology. 2005;288:1278-89.

[116] Carrier RL, Rupnick M, Langer R, Schoen FJ, Freed LE, Vunjak-Novakovic G. Perfusion improves tissue architecture of engineered cardiac muscle. Tissue engineering. 2002;8:175-88.

[117] Liu C, Abedian R, Meister R, Haasper C, Hurschler C, Krettek C, et al. Influence of perfusion and compression on the proliferation and differentiation of bone mesenchymal stromal cells seeded on polyurethane scaffolds. Biomaterials. 2011;33:1052-64.

[118] Maidhof R, Tandon N, Lee EJ, Luo J, Duan Y, Yeager K, et al. Biomimetic perfusion and electrical stimulation applied in concert improved the assembly of engineered cardiac tissue. J Tissue Eng Regen Med. 2012;6:e12-23.

[119] McCoy RJ, Jungreuthmayer C, O'Brien FJ. Influence of flow rate and scaffold pore size on cell behavior during mechanical stimulation in a flow perfusion bioreactor. Biotechnol Bioeng. 2012;109:1583-94.

[120] Sekine H, Shimizu T, Okano T. Myocardial tissue engineering: toward a bioartificial pump. Cell Tissue Res. 2012;347:775-82.

[121] Zimmermann W, Eschenhagen T. Cardiac tissue engineering for replacement therapy. Heart Failure Reviews. 2003;8:259-69.

[122] Rouwkema J, Gibbs S, Lutolf MP, Martin I, Vunjak-Novakovic G, Malda J. In vitro platforms for tissue engineering: implications for basic research and clinical translation. J Tissue Eng Regen Med. 2011;5:e164-7.

[123] Bursac N, Papadaki M, Cohen RJ, Schoen FJ, Eisenberg SR, Carrier R, et al. Cardiac muscle tissue engineering: toward an in vitro model for electrophysiological studies. Am J Physiol. 1999;277:H433-44.

[124] Asakawa N, Shimizu T, Tsuda Y, Sekiya S, Sasagawa T, Yamato M, et al. Pre-vascularization of in vitro three-dimensional tissues created by cell sheet engineering. Biomaterials. 2010;31:3903-9.

[125] Shimizu T, Sekine H, Yang J, Isoi Y, Yamato M, Kikuchi A, et al. Polysurgery of cell sheet grafts overcomes diffusion limits to produce thick, vascularized myocardial tissues. FASEB J. 2006;20:708-10.

[126] Nichol JW, Engelmayr GC, Jr., Cheng M, Freed LE. Co-culture induces alignment in engineered cardiac constructs via MMP-2 expression. Biochem Biophys Res Commun. 2008;373:360-5.

[127] Pillekamp F, Reppel M, Dinkelacker V, Duan Y, Jazmati N, Bloch W, et al. Establishment and characterization of a mouse embryonic heart slice preparation. Cell Physiol Biochem. 2005;16:127-32.

[128] Pillekamp F, Halbach M, Reppel M, Pfannkuche K, Nazzal R, Nguemo F, et al. Physiological differences between transplanted and host tissue cause functional decoupling after in vitro transplantation of human embryonic stem cell-derived cardiomyocytes. Cell Physiol Biochem. 2009;23:65-74.

[129] Habeler W, Peschanski M, Monville C. Organotypic heart slices for cell transplantation and physiological studies. Organogenesis. 2009;5:62-6.

[130] Habeler W, Pouillot S, Plancheron A, Puceat M, Peschanski M, Monville C. An in vitro beating heart model for long-term assessment of experimental therapeutics. Cardiovasc Res. 2009;81:253-9.

# CHAPTER 2

# DESIGN OF SEMIAUTOMATED TOOLING FOR FABRICATION OF POROUS POLYURETHANE FOAMS

## 2.1 Introduction

Through all of the work described in this dissertation, substrates were fabricated using custom, semiautomated tooling. Development of this tooling was performed prior to the research described in Chapters 3-5. The fundamental purpose of this tooling was to enable production of biomaterials to be used as three-dimensional substrata for cell culture. Beyond this requirement, consideration was given to reproducibility of output materials independent of the operator, and a high degree of flexibility to adapt this process to the unique requirements of small batch production. A combination of custom, and off-the- shelf components were used to build the spray tooling. The primary components of the spray assembly are a computer, off-the-shelf syringe pump, CNC robot (Fig 2.1 MaxNC, Gilbert AZ), the nozzle assembly (Fig 2.2), and the spray surface assembly (Fig 2.3). The spray surface assembly is comprised of a spray plate (Fig 2.4) on top of a waste reservoir (Fig 2.5). A silicone substrate (Fig 2.6) was used in Chapter 4 for sprayed micromolding of the material. Polyester frames (Fig 2.7) were used in the spray

surface assembly to facilitate handle-ability of the material after production. A mask (Fig 2.8) was aligned using alignment pins anchored to t-nuts on the surface of the CNC (Fig 2.9). At the end of this chapter, the engineering assembly drawings, part drawings, and bill of materials are included to describe the geometric and mechanical configuration of this device. Validation of the ability of this system to produce porous polyurethane substrates for use as cell scaffolding in cell culture is included in Chapter 3 and 4.

## 2.2 Spray Parameters

The important inputs to the spray process include the volume of polymer solution on the deposited on surface, the rate of deposition, the spray pressure, the spray pattern, and curing conditions. These parameters and their influence on the overall process are described in detail in the following sections.

### 2.2.1 Polymer Deposition

The volume of polymer deposited on the spray surface is determined by the concentration of the polymer solution and the volume of this solution that is pumped during spray. The polymer deposition was normalized to the area of the surface, yielding a coverage parameter measured in $g/in^2$. For this work, a coverage value of 0.65 $g/in^2$ was found to yield acceptable substrates. The coverage parameter can be altered in a custom Matlab program that will automatically calculate the corresponding pump settings. This value is limited on the upper side by accumulation of solvent that is trapped within the precipitated material, resulting in resolubilization of the deposited polymer,

and loss of control over the porous architecture, and on the lower limit by the handle-ability of the material after deposition.

### 2.2.2 Rate of Deposition

The rate of deposition is a function both of flow rate from the pump, and speed of the CNC while it moves through the spray pattern (discussed below). Precipitation of the polymer appears to happen relatively quickly with respect to the deposition rate, therefore, we used deposition rates that corresponded to the maximum linear travel speed of the CNC. The deposition rate is a user input parameter that can be altered for more sensitive processes requiring more time for precipitation or curing during fabrication.

### 2.2.3 Spray Pressure

Air pressure is required to aerosolize the polymer and nonsolvent solution. However, upon precipitation, the polyurethane materials fabricated in this work were very fragile and easily susceptible to plastic deformation. Artifacts in substrate geometry resulting from air flow induced deformation were minimized through minimizing the air pressure, and maximizing the working distance between the nozzles (see Fig 2.2) and the spray surface (Fig 2.3, see below for more details on spray pattern). A minimum of 10 PSI was required for adequate dispersal of the polymer and nonsolvent. Depending on the viscosity and surface tension of the solutions used, this value may potentially be reduced even lower. Regardless of the solutions used, air pressure should be minimized to decrease deformation of the substrate geometry by air flow.

2.2.4 Spray Pattern

The spray pattern is determined by the nozzle itself, and the working distance between the nozzle and the deposition surface. Initial spray experiments using dye loaded solutions sprayed onto absorbent paper demonstrated a linear increase ($R^2$=0.9995) in spray diameter as a function of the working distance from 7.6 cm to 17.8 cm. The maximum working distance with the spray plate (Fig 2.5) and waste reservoir (Fig 2.4) loaded into the assembly was 14.0 cm. A working distance of 13 cm was selected and calculated to produce a spray diameter of 5.1 cm at the surface. Due to the side-by-side arrangement of the nonsolvent and solvent spray nozzles (see Fig 2.2), nonuniform border regions exist around the border of the sprayed material. These regions, depending on their location receive either excess polymer solution, or excess nonsolvent. To ensure consistent material properties in the final biomaterial, a mask (Fig 2.8) was designed and incorporated into the spray surface assembly to separate the consistent center regions from the nonhomogenous border regions. The travel distance in the X and Y axis of the CNC robot, in conjunction with the offset of the nozzles in the cross head and working distance provide a maximum consistent spray region of 13.3 cm x 8.9 cm.

Beyond the available space to create a uniform spray deposition, the spray pattern itself was controlled. The CNC traversed the spray in a serpentine pattern. The pitch of the each traverse is a user input parameter, limited on the low end by the ability of an off-the-shelf syringe pump to consistently deliver low volumes, and on the high end by the diameter of the spray pattern by the nozzle. For this research, a 17 mm step over was found to provide good coverage, while working within an optimal flow rate for the pump. In addition to the pitch, the number of passes is a variable user input. We used two coats

to create substrates that were approximately 200 μm thick in order to return the spray nozzles to the start position at the end of a run, although fewer or more coats seemed to work equally well.

### 2.2.5 Curing Conditions

After spray, the majority of the solvent and nonsolvent are collected in the waste reservoir. Removal of residual solvent is necessary for curing the material. Removal of solvent can be accomplished through evaporation or through diffusion when submerged in a solvent-miscible nosolvent. For all the polyurethane material used in this research, an aqueous nonsolvent was used. It was observed that relative humidity impacted the curing process when solvent was allowed to evaporate. To control for variations in relative humidity, samples were cured in water to remove residual solvent. Another important environmental parameter influencing the rate of solvent removal is ambient temperature. It was observed that low temperatures appeared to decrease the rate of solvent removal, resulting in slower kinetics of precipitation, and generally, higher porosity. All experiments were performed at room temperature, and relied on nonsolvent composition to influence the kinetics of precipitation, but future applications could utilize temperature as well as nonsolvent composition to influence material architecture using this system.

## 2.3 Tooling Applications

In the research described in this dissertation, the material used with system was an elastomeric poly (ether-urethane), however, while this was the only material used in this

research, the tooling described in this chapter has also been used to deposit drug loaded poly (lactic-glycolic acid) (PLGA) coatings, and fabricate composite polyurethane /collagen blends. Future adaption of the spray parameters described in this section can be used to fabricate a wide variety of porous biomaterial sheets using the tooling described here.

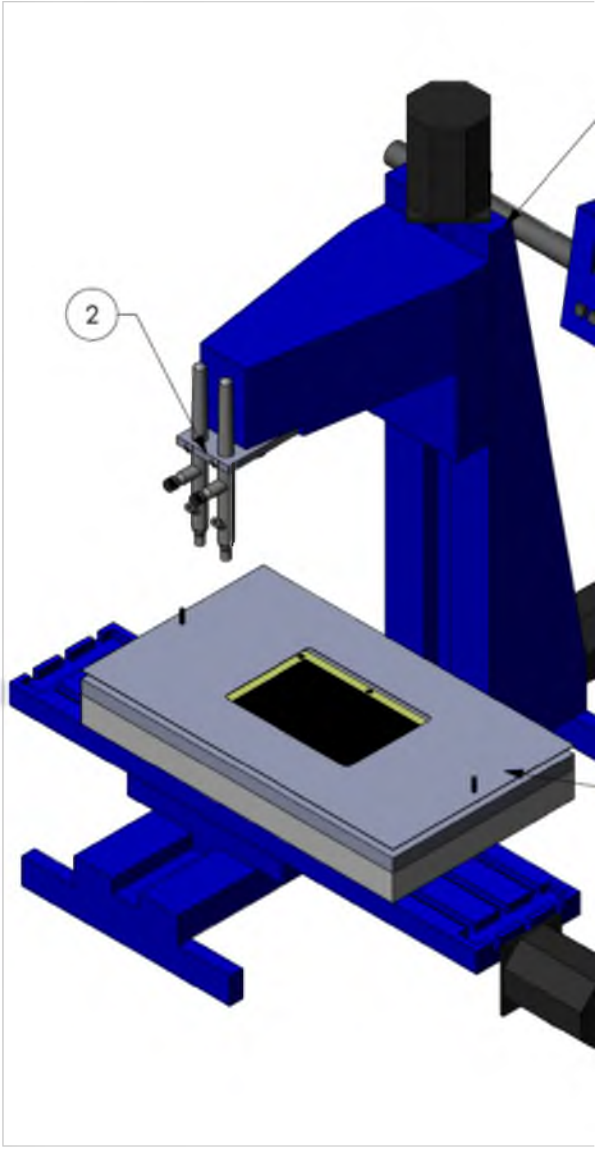
2

| REV | DESCRIPTION | DWN | DATE |
|---|---|---|---|
| 01 | INITIAL RELEASE | JK | 2/27/13 |
| | | | |
| | | | |
| | | | |
| | | | |

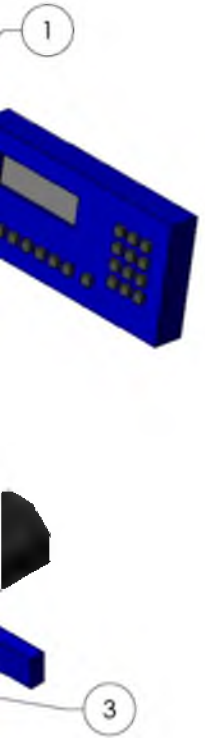


| Item No. | Description | QTY. |
|---|---|---|
| 1 | CNC Computer Mill (MAXNC, P/N MAXNC15 | 1 |
| 2 | Spray nozzle assembly - See Page 2 | 1 |
| 3 | Spray substrate - See Page 3 | 1 |

**UNIVERISTY OF UTAH**
20 S 2030 E Rm 108
Salt Lake City, 84112

| | | |
|---|---|---|
| TITLE: Base Assembly | | |
| SIZE A | DWG. NO. N/A | REV 01 |
| PART NO: N/A | SPEC: N/A | |
| MODEL FILE: Base Assembly | | |
| SCALE: 1:4 | | SHEET 1 OF 9 |

Fig 2.1 Spray assembly

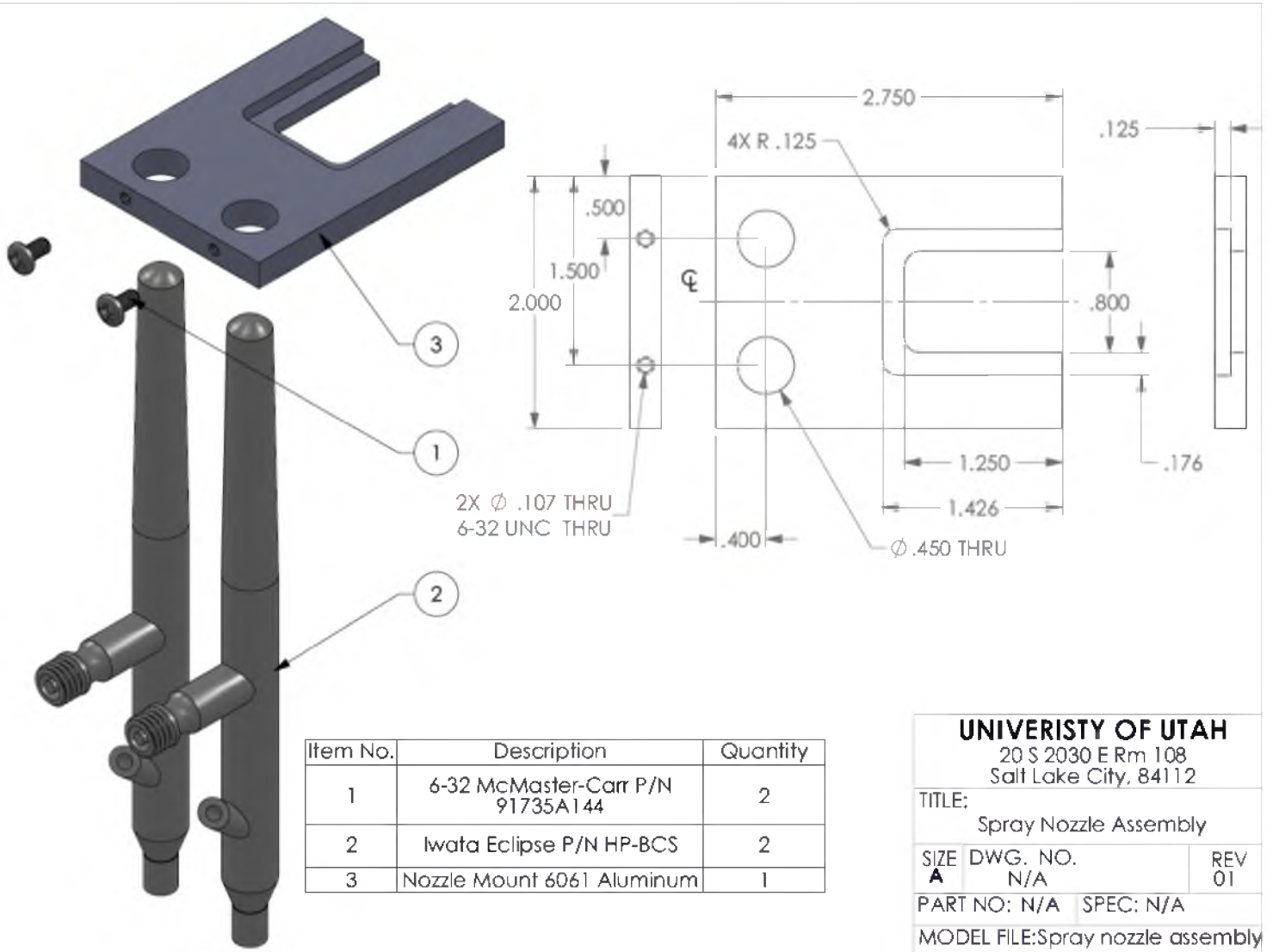


| Item No. | Description | Quantity |
|---|---|---|
| 1 | 6-32 McMaster-Carr P/N 91735A144 | 2 |
| 2 | Iwata Eclipse P/N HP-BCS | 2 |
| 3 | Nozzle Mount 6061 Aluminum | 1 |

**UNIVERISTY OF UTAH**
20 S 2030 E Rm 108
Salt Lake City, 84112

| | | |
|---|---|---|
| TITLE: Spray Nozzle Assembly | | |
| SIZE A | DWG. NO. N/A | REV 01 |
| PART NO: N/A | SPEC: N/A | |
| MODEL FILE:Spray nozzle assembly | | |
| SCALE: 1:1 | | SHEET 2 OF 9 |

Fig. 2.2 Nozzle assembly

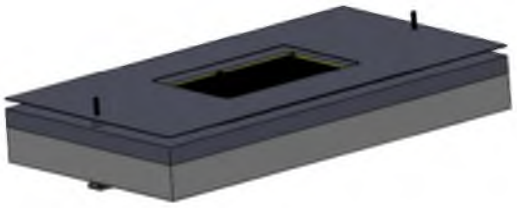

| Item Number | Description | Quanity |
|---|---|---|
| 1 | Aluminum T-Nut - see page 9 | 2 |
| 2 | Aluminum Alignment Pin - see page 9 | 2 |
| 3 | Polyethylene Waste Resevior - see page 4 | 1 |
| 4 | Aluminum Spray Plate - see page 5 | 1 |
| 5 | VST50 Platinum Cure Silicone - see page 6 | 1 |
| 6 | Polyester Frame - see page 7 | 1 |
| 7 | Aluminum Mask - see page 8 | 1 |

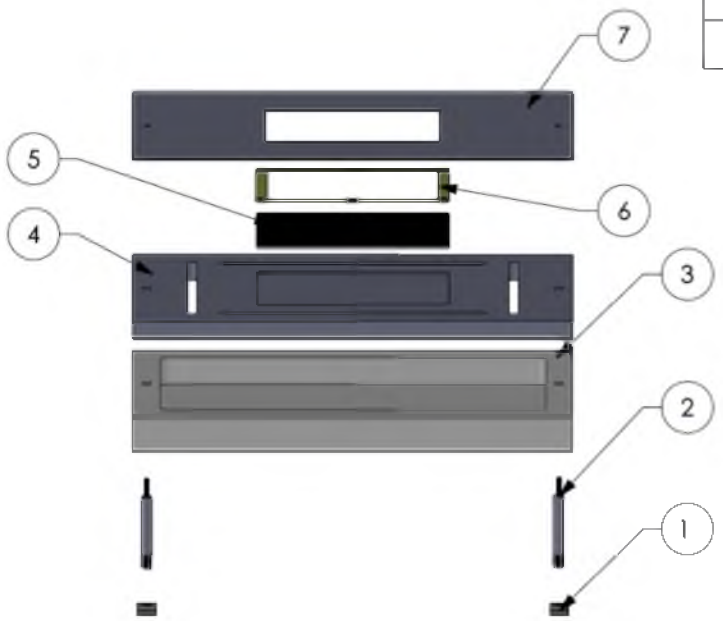


Fig 2.3 Spray surface assembly

**UNIVERISTY OF UTAH**
20 S 2030 E Rm 108
Salt Lake City, 84112

TITLE:
Spray Substrate

| SIZE | DWG. NO. | REV |
|---|---|---|
| A | N/A | 01 |

PART NO: N/A | SPEC: N/A

MODEL FILE: Spray assembly

SCALE: 1:4 | SHEET 3 OF 9

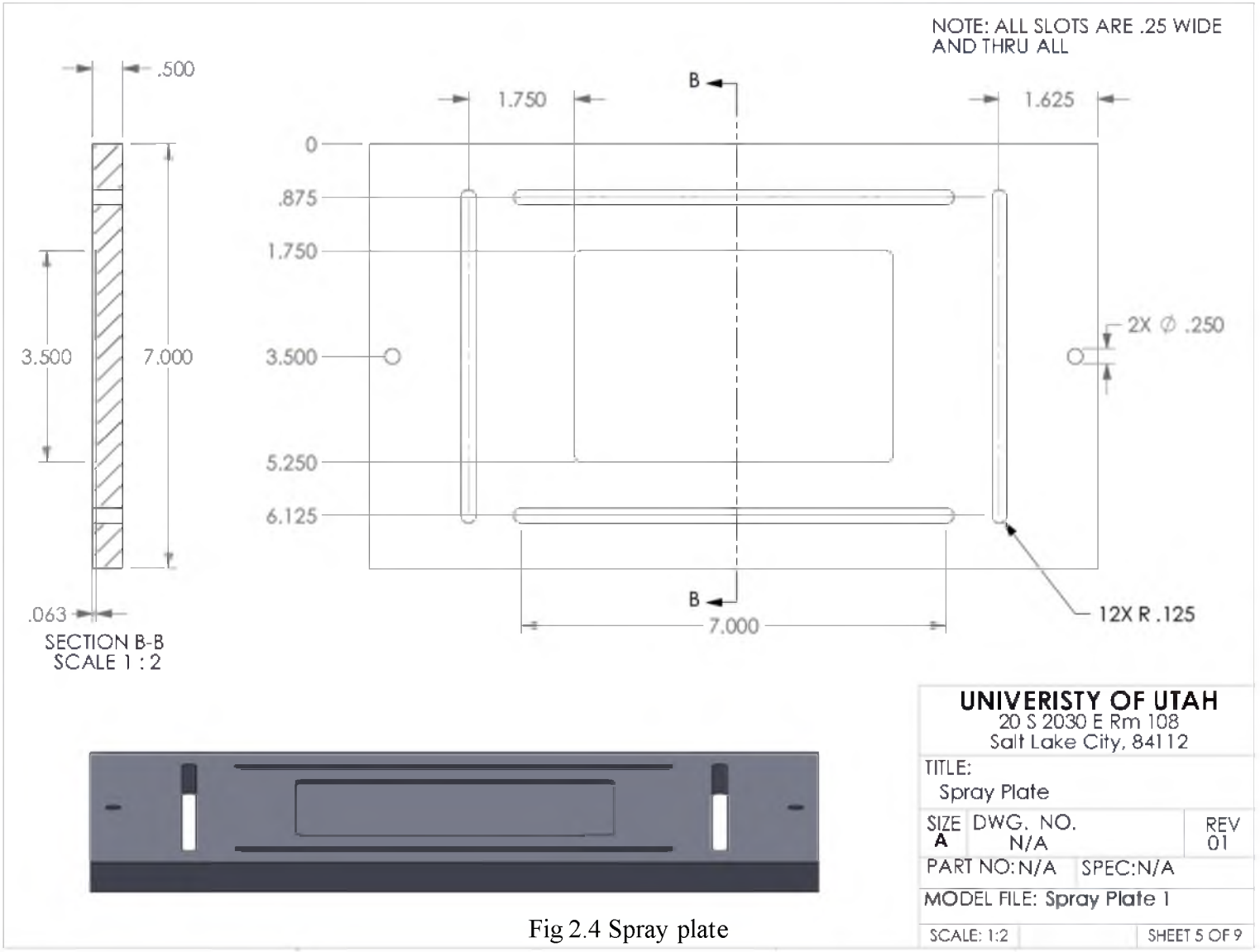


Fig 2.4 Spray plate

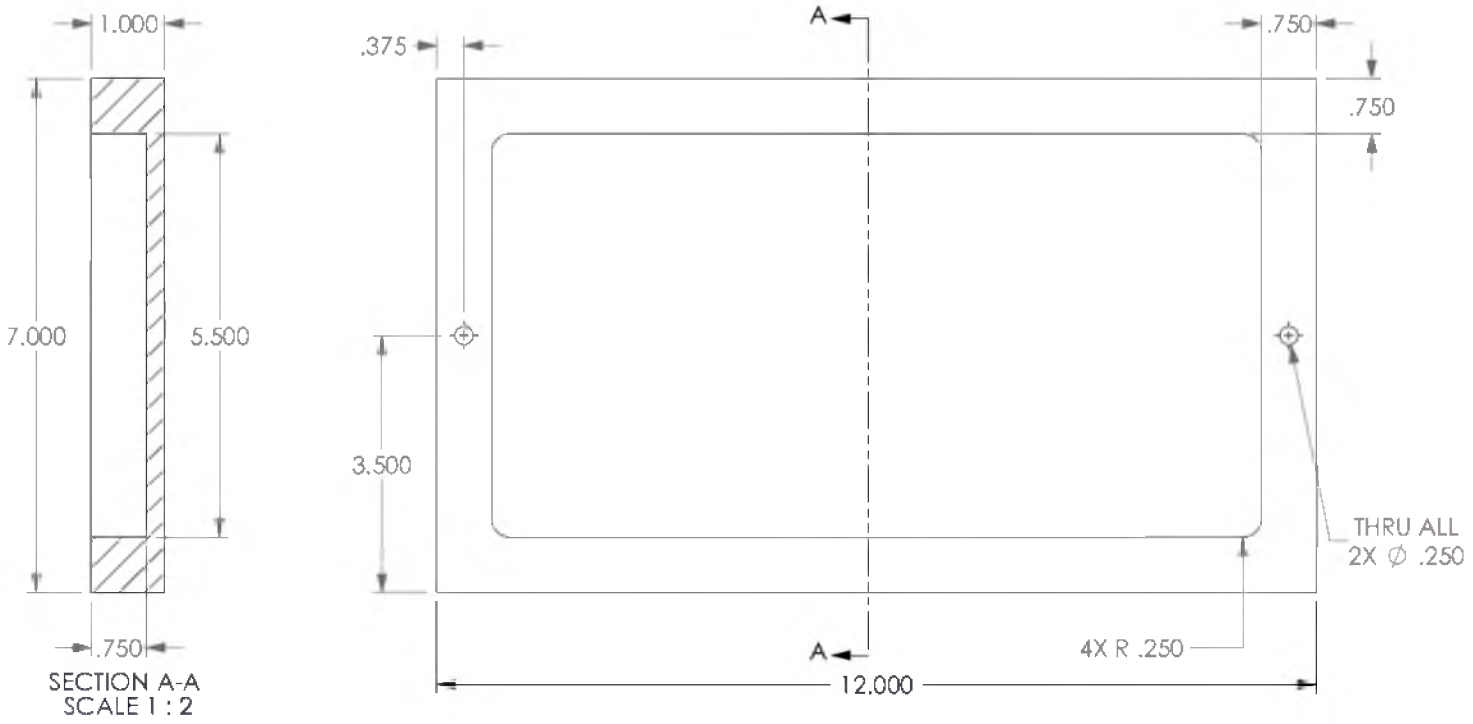


| UNIVERISTY OF UTAH<br>20 S 2030 E Rm 108<br>Salt Lake City, 84112 | | |
|---|---|---|
| TITLE:<br>Waste Reservoir | | |
| SIZE<br>A | DWG. NO.<br>N/A | REV<br>01 |
| PART NO: N/A | SPEC: N/A | |
| MODEL FILE: waste reservoir | | |
| SCALE: 1:2 | | SHEET 4 OF 9 |

Fig 2.5 Waste reservoir

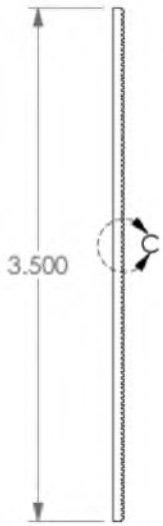


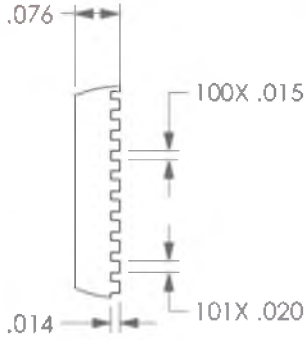


DETAIL C
SCALE 4 : 1

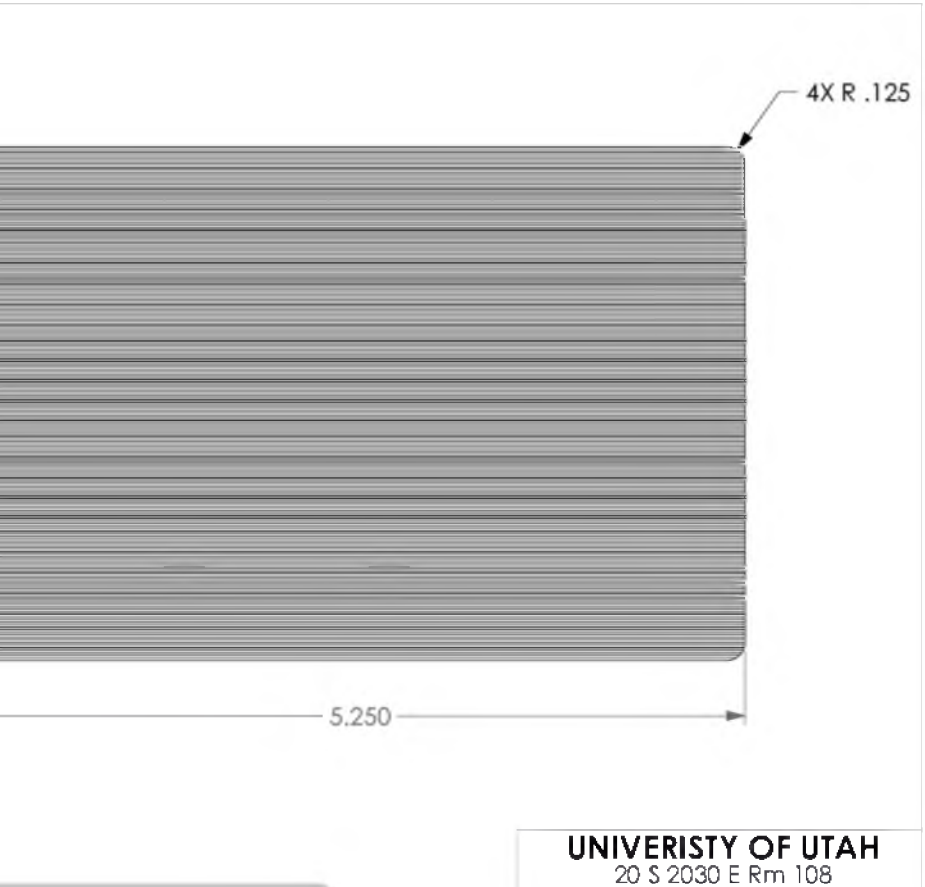


| UNIVERISTY OF UTAH<br>20 S 2030 E Rm 108<br>Salt Lake City, 84112 | | |
|---|---|---|
| TITLE:<br>Spray Substrate | | |
| SIZE<br>A | DWG. NO.<br>N/A | REV<br>01 |
| PART NO: N/A | SPEC: N/A | |
| MODEL FILE:<br>Silicone pattern 500w 875p 350d | | |
| SCALE: 1:1 | | SHEET 6 OF 9 |

Fig. 2.6 Spray substrate

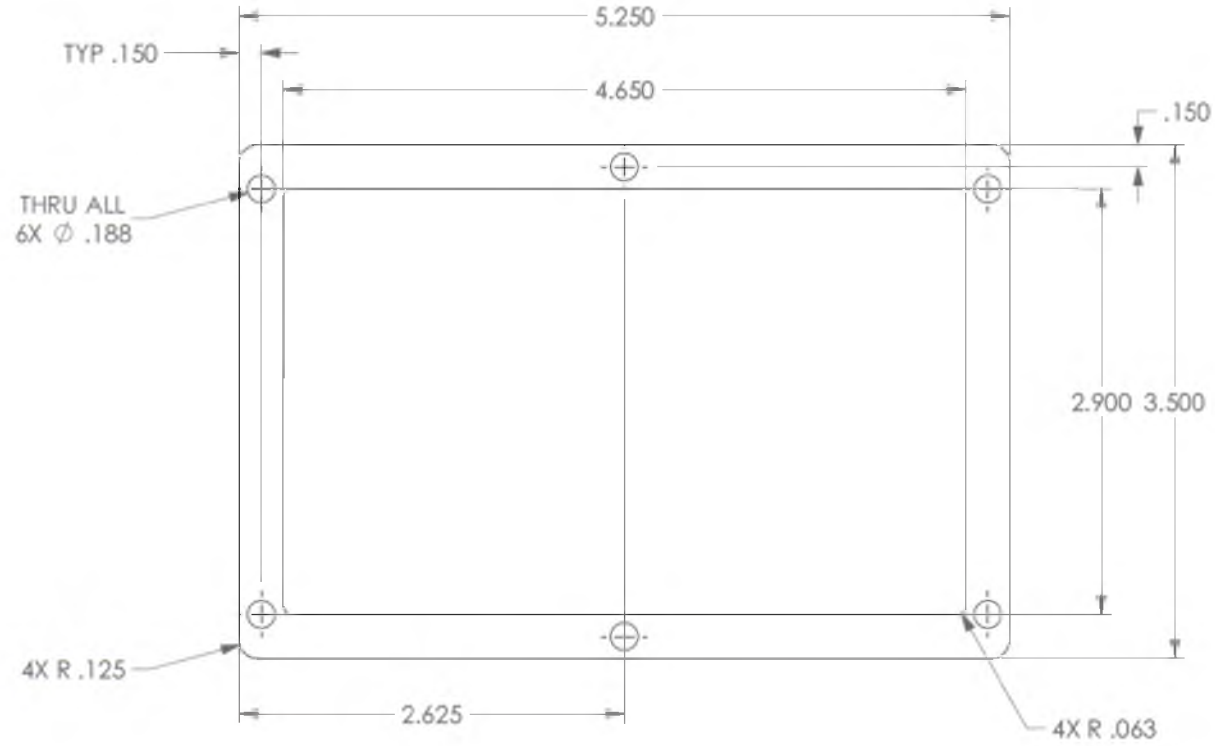


NOTE: THICKNESS IS .014

| UNIVERISTY OF UTAH<br>20 S 2030 E Rm 108<br>Salt Lake City, 84112 | | |
|---|---|---|
| TITLE:<br>Frame | | |
| SIZE<br>A | DWG. NO.<br>N/A | REV<br>01 |
| PART NO: N/A | SPEC: N/A | |
| MODEL FILE: Large frame | | |
| SCALE: 1:1 | | SHEET 7 OF 9 |

Fig 2.7 Scaffold frame

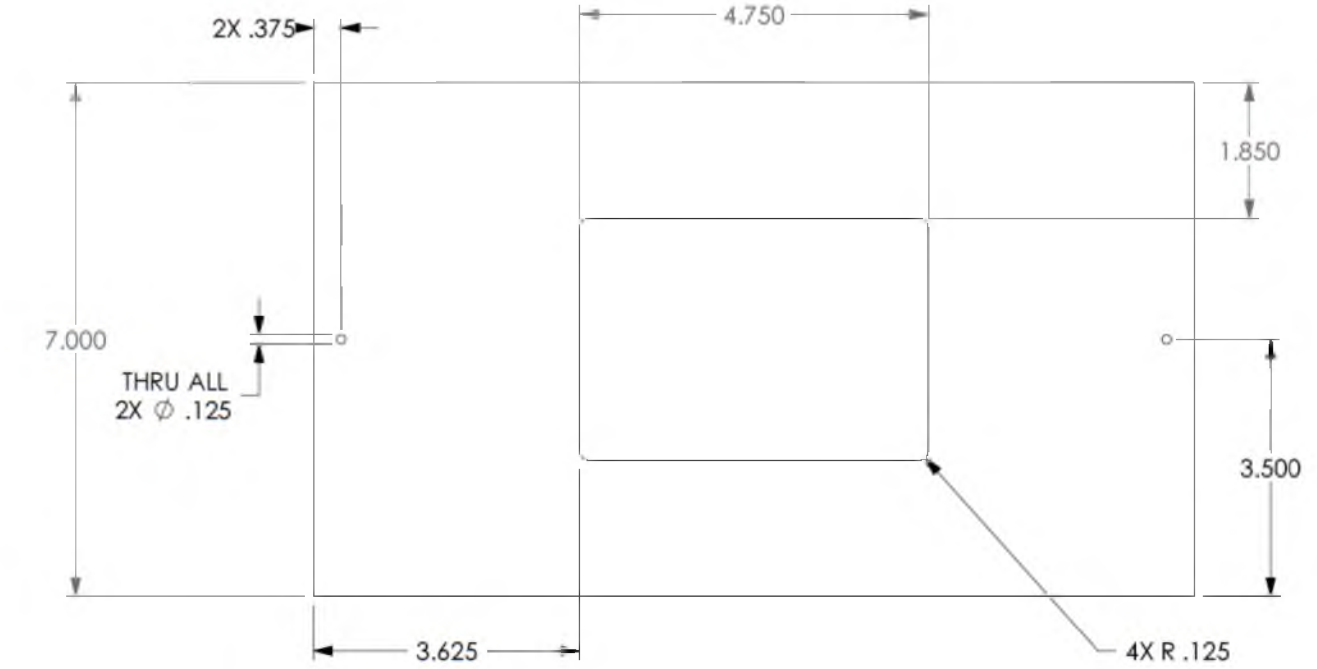


NOTE: THICKNESS IS .0625

| UNIVERISTY OF UTAH<br>20 S 2030 E Rm 108<br>Salt Lake City, 84112 | | |
|---|---|---|
| TITLE: Mask | | |
| SIZE A | DWG. NO. N/A | REV 01 |
| PART NO: N/A | SPEC: N/A | |
| MODEL FILE: mask2 | | |
| SCALE: 1:2 | | SHEET 8 OF 9 |

Fig 2.8 Mask

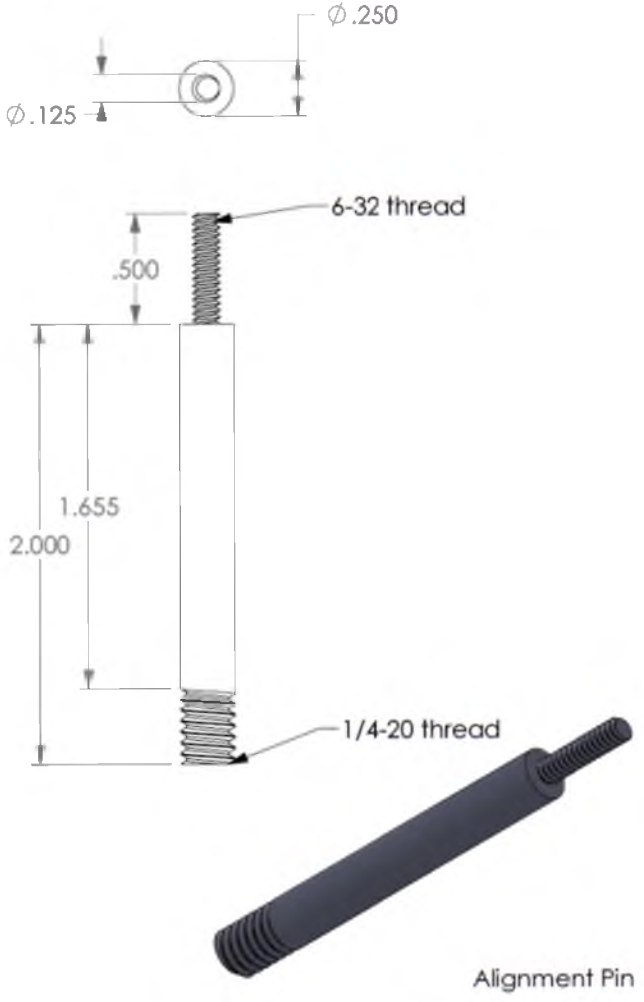


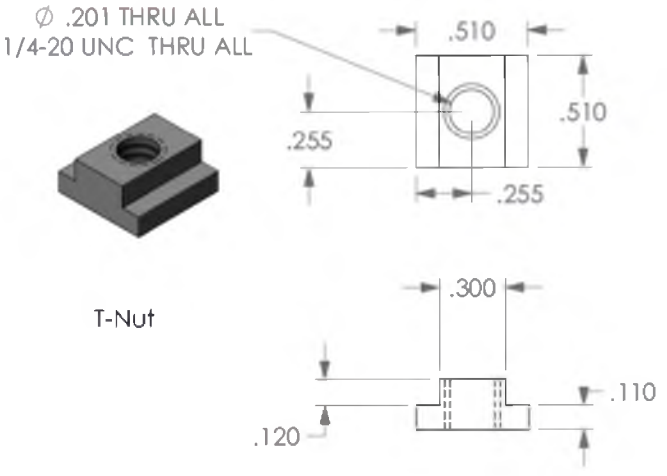


| UNIVERISTY OF UTAH<br>20 S 2030 E Rm 108<br>Salt Lake City, 84112 | | |
|---|---|---|
| TITLE: Alignment Pin and T-Nut | | |
| SIZE A | DWG. NO. N/A | REV 01 |
| PART NO: N/A | SPEC. N/A | |
| MODEL FILE: alignment pin | | |
| SCALE: 3:2 | | SHEET 9 OF 9 |

Fig 2.9 Alignment pin and t-nut

# CHAPTER 3

# THE MECHANICALLY ENHANCED PHASE SEPARATION OF SPRAYED POLYURETHANE SCAFFOLDS AND THEIR EFFECT ON THE ALIGNMENT OF FIBROBLASTS

Reprinted from Biomaterials, Vol 31 Issue 6, Kennedy, J. P. McCandless, S. P. Lasher, R. A. Hitchcock, R. W, The mechanically enhanced phase separation of sprayed polyurethane scaffolds and their effect on the alignment of fibroblasts 1126-1132, (2010), with permission from Elsevier

Biomaterials 31 (2010) 1126–1132

Contents lists available at ScienceDirect

Biomaterials

journal homepage: www.elsevier.com/locate/biomaterials

# The mechanically enhanced phase separation of sprayed polyurethane scaffolds and their effect on the alignment of fibroblasts

James P. Kennedy, Sean P. McCandless, Richard A. Lasher, Robert W. Hitchcock*

*Department of Bioengineering, University of Utah, 20 S 2030 E, Rm 108 Salt Lake City, UT 84112, USA*

ARTICLE INFO

*Article history:*
Received 3 August 2009
Accepted 9 October 2009
Available online 30 October 2009

*Keywords:*
Scaffold
Cell alignment
Mechanical properties
Porosity
Polyurethane
Tissue engineering

ABSTRACT

This paper reports a method to fabricate anisotropic scaffolds of tunable porosity and mechanical properties. Scaffolds were fabricated using a computer controlled sprayed phase separation technique. Following fabrication, the sheets were elongated 0, 35 or 70% of their original length to induce varying degrees of scaffold alignment and anisotropy. The nonsolvent used in the phase separation was shown to affect porosity and the elastic modulus. Mouse embryo NIH-3T3 fibroblasts were cultured on the scaffolds to investigate cell response to the anisotropy of the scaffold. A 2D FFT method was used to quantify cellular alignment. Cells were shown to align themselves with the scaffold. This sheet-like scaffold material can be used in single plys or can be laminated to form porous 3D composite scaffolds.
Published by Elsevier Ltd.

## 1. Introduction

Tissue engineering and regenerative medicine have the potential to develop novel biosynthetic materials for improved treatment, maintenance, and regeneration of diseased or damaged tissue. Development of materials that utilize tissue engineering strategies requires design considerations such as cell type, seeding and attachment, as well as molecular signals, and macromolecular matrix in order to develop constructs that improve or replace function of natural tissue [1–3]. Many types of engineered tissue rely on a provisional or permanent scaffold to generate a three-dimensional framework for cell attachment and tissue organization. Both natural and synthetic scaffold materials are used in tissue engineering [4,5]. Synthetically derived cell scaffolds can be permanent or degradable and facilitate expression and organization of the extracellular matrix (ECM). Architectural cues in these scaffolds have been shown to affect the morphology, organization, and phenotypic expression of cells in vitro [6–8]. In order to develop effective implants, the tissue engineer needs to be able to specify and tune the scaffold's morphological features for different applications. In addition, scaffold architecture must be designed to provide cues for cellular organization and form the basis for engineered tissue constructs that mimic tissue specific organization and physical properties.

Cardiac tissue is an example of highly structured tissue that relies on cellular organization for its function [9,10]. Cell scaffold materials can help cardiac tissue development by: (1) providing cues that induce alignment of cardiac myocytes, (2) allowing sufficient nutrient and cell infiltration necessary to form a 3D tissue construct, (3) modulating the cell type distribution of co-cultures, and (4) mimicking anisotropic mechanical stiffness of the heart. Scaffolds used for cardiac tissue engineering applications require development of design specifications that include scaffold alignment, structure, porosity, and stiffness all of which will influence cellular development, overall tissue organization, and bioreactor integration [11–13].

Various methods have been employed to fabricate scaffolds of varying porosity and anisotropy. For example, microfabrication techniques have been used to fabricate scaffolds with aligned structure [14,15]. Electrospinning methods have been employed with post process elongation to produce anisotropic fibrous scaffold architecture [16]. In order to create scaffolds that allow adequate nutrient and oxygen diffusion, methods such as 3D fiber deposition, sacrificial fiber electrospinning, and phase separation have been utilized to generate scaffolds of controlled porosity [17–20]. Spray phase separation (SPS) is method for creating scaffolds with control over alignment, porosity, and stiffness; however this method has not been directly applied for cardiac tissue scaffolds [19].

SPS fabricated scaffolds are produced using a method that simultaneously sprays a polymer solution and a nonsolvent onto the surface. The nonsolvent mixes with the solvent and the

* Corresponding author.
*E-mail address:* r.hitchcock@utah.edu (R.W. Hitchcock).

0142-9612/$ – see front matter Published by Elsevier Ltd.
doi:10.1016/j.biomaterials.2009.10.024

polymer causing the polymer to precipitate. Some groups have used SPS methods to fabricate materials of varying porosity for drug delivery devices [21] and vascular graft materials [19,22]. SPS fabrication is a promising method for controlling scaffolds properties such as alignment, porosity, stiffness, and anisotropy, which are key features for directing cellular development, overall tissue organization, and bioreactor integration [11–13].

We hypothesized that post spray elongation of SPS scaffolds would generate scaffold microstructure alignment and in turn induce cellular alignment. Furthermore, we hypothesized that the nonsolvent (NS) EtOH concentration would affect scaffold porosity. In addition, we hypothesize that this material may be laminated into thick scaffold material. Here we report an SPS method for fabricating polyurethane scaffolds for tissue engineering applications.

## 2. Materials and methods

### 2.1. Scaffold fabrication

Scaffolds were fabricated using an SPS method. A 4% polyurethane solution was prepared by dissolving Tecoflex SG80 polyether polyurethane (Lubrizol Advanced Materials Inc. Cleveland, OH) in dimethylacetamide (DMAc) (Sigma Aldrich, St. Louis, MO). Polyether polyurethane was selected because of its known biocompatibility, ease of processing, and extensive use in the past for scaffold materials [23–25]. The polymer solution was sealed in glass storage containers prior to use and used immediately after opening to ensure that minimal solvent was lost through evaporation. Deionized water (referred to as 0% ethanol), 50% EtOH, and 70% EtOH solutions were used as the nonsolvent for precipitation.

Spray nozzles (Excel ES4, Porter Cable, Jackson, TN) were mounted onto a custom crossbar attached to the spindle head of a computer-controlled desktop milling machine (MaxNC 12, MAXNC, Gilbert AZ) to provide X–Y–Z control of spray pattern. Custom G-code was used to move the spray head and control the spray pattern and spray time. The spray nozzles traversed the substrate at a distance of 20 cm and a speed of 0.85 cm/s in a serpentine pattern yielding a total spray time of 2.5 min.

Aluminum frames were designed to facilitate manipulation and mechanical alignment of the scaffold material during and after spraying. The frames were fabricated from 0.32 cm thick 6016-T6 aluminum (McMaster-Carr, Princeton NJ) with an outside dimension of 5.3 cm × 3.7 cm and an inside dimension of 2.86 cm × 2.54 cm. Stainless steel hypodermic tubing sliders (Small Parts Inc., Miramar, FL) were assembled and attached to frames with UV cure adhesive to facilitate elongation and constrain the maximum elongation to 3.86 cm (35% elongation) or 4.86 cm (70% elongation). Frames without sliders were used to make scaffolds with no in-process mechanical alignment. Stainless steel screens (Type 316 Mesh #60, Small Parts Inc.) were attached to the opposite ends of the frame to provide a rigid, yet porous surface for scaffold adherence. A sheet of 0.32 cm thick aluminum (McMaster-Carr) was coated with silicone (VST 50 silicone elastomer, Factor II Inc., Lakeside, AZ) to prevent the scaffold from sticking to the aluminum. Three frames (one of 0%, 35% and 70% elongation) were clamped to this silicone coated aluminum backing which was subsequently placed inside the spray chamber.

The polymer solution and nonsolvent were sprayed simultaneously onto the frames at a pressure of 40 psi. Spray rates were calculated by measuring the mass loss of the spray reservoir after a 30 s test spray. Spray rates of the polymer solution and the nonsolvent were adjusted on the spray nozzle to 7.5 ± 0.5 g/min and 45.0 ± 5.0 g/min respectively to achieve uniform scaffold structure.

After the spray process was completed, scaffolds were immediately rinsed with gently flowing DI water for 1 min. The frames were then removed from the aluminum backing, and scaffolds were elongated 0%, 35% or 70% of their original length and allowed to dry for 24 h in the stretched conformation. After the scaffolds were dry, they were removed from the frames for testing.

### 2.2. Mechanical testing

Mechanical properties were measured in the direction aligned with the in-process elongation (preferred direction) and perpendicular (transverse) to this direction. A sample was removed from the center of each scaffold for mechanical testing ($n = 3$). The samples used for longitudinal testing measured 20.0 mm × 5.0 mm and the samples used for transverse testing measured 5.0 mm × 1.5 mm. These sizes were chosen based on the physical limitations of the scaffold and frame configuration. Samples were tested on an Instron 3342 (Instron, Norwood MA) with a 50 N load cell. A gauge length of 10 mm was used for longitudinal testing, while a gauge length of 3 mm was used for transverse testing. The samples were tested to 40% strain at a speed of 20 mm/min. The effective stress for each sample was calculated by dividing the force by the overall cross section. From the effective stress and strain data an effective modulus of elasticity was calculated in both the preferred and the transverse direction. Anisotropy is reported as the ratio of the effective modulus in the preferred direction to the effective modulus in the transverse direction.

### 2.3. Porosity

Porosity is defined as the ratio of the void space to the total volume of a solid. Total volume was calculated by measuring length, width and height of rectangular scaffold samples [26]. The mass of the scaffold samples was then used in conjunction with the specific gravity of Tecoflex SG80 polyurethane (1.04 g/cc) to determine the volume of polyurethane in the sample. Void space was the difference in volume between the total volume, and the volume of the polyurethane. Porosity was calculated as the ratio of void space to total volume of the scaffold.

### 2.4. Cell culture and seeding

Mouse embryo fibroblast NIH-3T3 cells were cultured in Dulbecco's modified Eagle medium (DMEM) with 10% FBS and 1% L-glutamine, and 1% penicillin and streptomycin (Invitrogen, Carlsbad, CA). All culture media mentioned herein is the same as described above unless otherwise noted. Cells were cultured in a T- flask (Fisher Scientific, Waltham, MA) and media was changed twice per week until they reached approximately 90% confluence. Cells were then passaged. Briefly, culture media was removed from the cells. Cells were then rinsed with sterile PBS to remove any remaining culture media. Trypsin was added to the flask, and allowed to act for 2–4 min. at 37° C. Fresh media was then added to quench the trypsin. Cells were centrifuged and the supernatant discarded. The cell containing pellet was then resuspended in fresh media and transferred to a new T-flask. Cells were passaged three times before seeding onto the scaffold.

Prior to seeding, scaffolds were sterilized by spraying with 70% EtOH and rinsing with sterile PBS and culture media. Cells were removed from the surface of the cell culture flask via trypsinization as described above. These cells were then separated from trypsin through centrifugation and resuspended in cell culture media. Approximately $3.5 \times 10^7$ cells were seeded by gently pipetting 500 µl of the cell suspension onto the surface of the scaffold in a 100 mm plastic culture dish (Fisher Scientific). Cells were allowed to attach for two hours according to previously published methods (7) before the scaffold was covered with fresh culture media. Media was replaced with fresh media twice each week for 14 days.

### 2.5. Cell imaging and analysis

Following cell culture, cells were imaged with fluorescein diacetate (FDA) (Invitrogen) to ensure that viable cells were present. The cells were then fixed with 4% paraformaldehyde, and stained with DAPI (Invitrogen) for nuclei visualization and phalloidin conjugated with alexafluor 488 (Invitrogen) for actin filament visualization according to the manufacture's guidelines. Images were then collected using an Olympus FV 1000 (Center Valley, PA) confocal microscope starting at the surface of the scaffolds, and capturing image slices every 5 µm to a depth of 50 µm. These stacks were then projected into a single image of the maximum intensity pixels through scaffold using ImageJ, (NIH imaging software, Bethesda MD).

Image analysis was performed on the projected images using custom written MATLAB code. A 2D FFT method similar to what is reported by Ayers et al. was used to measure the direction fiber alignment [27]. Briefly, randomly selected regions of cell growth were processed with a Gaussian filter in order to reduce edge effects. A 2D FFT was performed and filtered to include only frequencies from 20–50 pixels. This range was selected based on the average spacing of actin filaments in the images in order to decrease artifacts from larger structures such as scaffold structure. Average pixel intensity was measured at every angle in the frequency range mentioned above. Average pixel intensity was plotted with respect to the angle from horizontal, and shifted 90° to align the peak with the direction of actin filament alignment. Cellular alignment is reported as the orientation index, which is defined as the angle that captures 50% of the actin filament alignment, as determined by the area under the average pixel intensity curve.

### 2.6. Scaffold lamination

In order to generate thicker materials, scaffolds were laminated during the drying process. Scaffolds were fabricated as described previously and elongated 70%. Instead of drying overnight individually, five scaffolds were placed one on top of another and allowed to dry. During the drying process the scaffolds formed a continuously adhered lamination. After the laminated scaffolds had dried, they were frozen in liquid nitrogen and broken to expose the cross section. The cross section of these thick scaffolds was observed through electron microscopy to qualitatively assess pore structure and the lamination interface.

### 2.7. SEM

Scaffolds were sputter coated with gold (Pelco SC-7, Ted Pella, Inc., Redding, CA) prior to electron microscopy and imaged using a Hitachi S-2460 N (Hitachi, Tokyo, Japan) at 35× (laminated scaffold) or 200× magnification and a voltage of 10.0 kV.

### 2.8. Statistical analysis

A single factor ANOVA ($\alpha = 0.05$) was used to compare moduli of scaffolds prepared with the same nonsolvent. A Tukey post hoc test was used to assess statistical significance. Unpaired *t*-tests were used to assess the statistical significance of porosity and cellular alignment.

## 3. Results

Scaffolds of varying anisotropy were fabricated using the computer controlled dual spray nozzle apparatus. For these initial studies, nonsolvent (NS) concentrations of 0%, 50% and 70% EtOH were used. Post-spray elongation was varied at 0%, 35% and 70%. Scaffold thickness was $75 \pm 8$ μm for 0% EtOH scaffolds, $167 \pm 42$ μm for 50% EtOH scaffolds, and $210 \pm 11$ μm for 70% EtOH scaffolds, per individual sheet. SEM visualization revealed that scaffolds fabricated with lower NS concentrations of EtOH appeared to have fewer pores than scaffolds fabricated with higher NS concentrations of EtOH (Fig. 1). As the percent post-spray elongation (PE) increased more elongated and aligned surface architecture was observed (Fig. 1). Scaffolds fabricated with 50% or 70% EtOH NS were found to have microfibers oriented in the direction of elongation. Scaffolds fabricated with 0% EtOH NS did not have fibers, but did show increasing alignment of ridge-like structures as the PE increased.

### 3.1. Tensile properties and anisotropy

Tensile testing was performed to determine the effects of PE and NS composition on the mechanical properties of the scaffolds. Testing was performed in the preferred direction (PD) and perpendicular to the direction of alignment (transverse, XD). The modulus was calculated for the linear portion of the stress–strain curve, which for all scaffolds corresponded to strains from 10–40%. Transverse moduli for 70% PE scaffolds were less than the longitudinal modulus ($p < 0.05$), while the transverse moduli of 35% PE scaffolds were always less but not always significant (Fig. 2). All scaffolds that were mechanically aligned showed a significant increase in longitudinal modulus between 0% and 35%, and 0% and 70% PE ($p < 0.05$) (Fig. 2). All scaffolds fabricated with equal PE exhibited increasing effective moduli as the NS EtOH decreased ($p < 0.05$).

Mechanical anisotropy of the scaffolds was assessed as the ratio of the longitudinal modulus to the transverse modulus. For all scaffolds the anisotropy ratio increased as the PE increased (Table 1).

### 3.2. Porosity

Porosity of the scaffolds varied with respect to the percent EtOH used in the NS. Measured porosity was independent of in-process elongation (data not shown). Porosity of scaffolds fabricated with

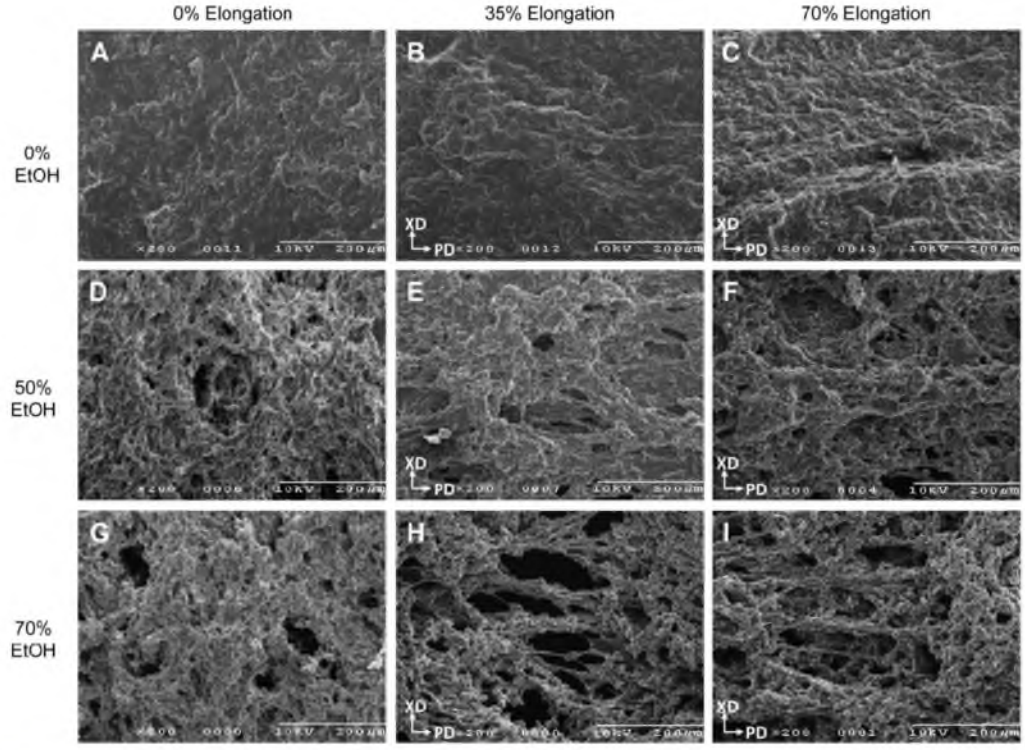


**Fig. 1.** Representative SEM images of scaffolds. (A–C) 0% EtOH nonsolvent, (D–F) 50% EtOH nonsolvent, (G–I) 70% EtOH. The first column (A, D, G) were not elongated; the second column (B, E, H) were elongated 35%; the third column (C, F, I) were elongated 70%. Scale bars are 200 μm.

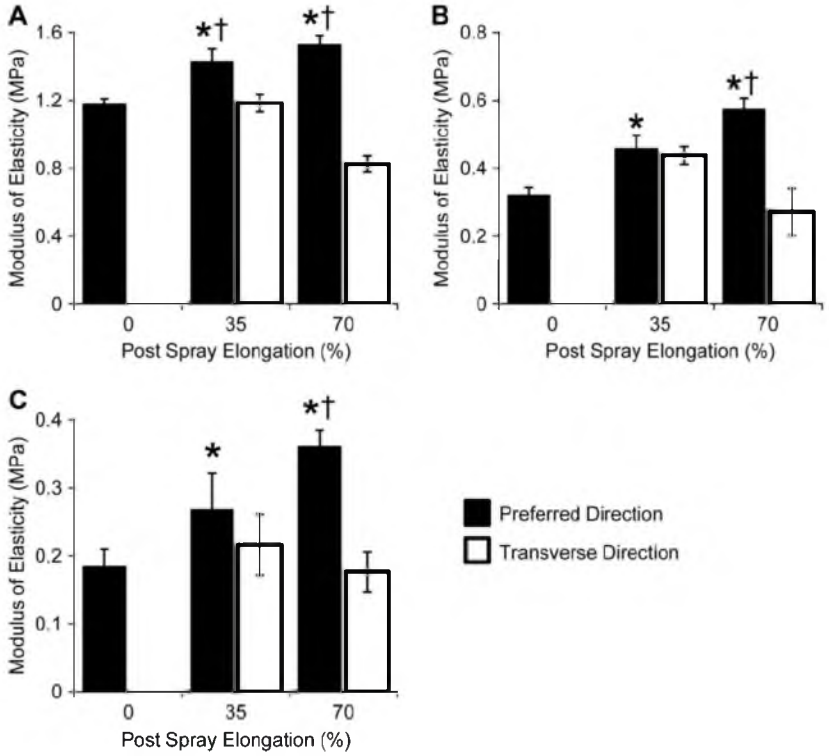


**Fig. 2.** Effective modulus of elasticity of scaffolds fabricated with (A) 0% EtOH, (B) 50% EtOH, and (C) 70% EtOH. Longitudinal moduli were compared to 0% elongation (*). 35% and 70% scaffolds were compared to themselves in the longitudinal and transverse directions (†).

0% EtOH NS (porosity of 70 ± 6%) was lower than those fabricated with 50% EtOH NS (porosity of 78 ± 3%, $p = 0.0006$) (Fig. 3). Scaffolds fabricated with 70% EtOH (porosity of 88 ± 2%) had a significantly higher porosity than scaffolds fabricated with 50% EtOH NS ($p = 0.00014$).

### 3.3. Cellular alignment

To determine the effect of the scaffold microarchitecture on cellular alignment, actin filaments of the cells were stained with phalloidin and nuclei were stained with DAPI (Fig. 4). Cells were imaged at 20x magnification in order to include the largest number of cells in the field of view while maintaining sufficient resolution to image individual actin filaments. Scaffolds were imaged at 5 μm intervals from the surface of the scaffold to a depth of 50 μm. Cells were generally observed to be aligned with scaffold filaments and along the pore edges of the material. An example of a typical 2D FFT and pixel intensity plot are shown in Fig. 5A and B respectively. Orientation index decreased as post-spray elongation increased ($p < 0.05$)(Fig. 6). Lower orientation indices represent more aligned actin filament orientation. No significant differences were observed between 50% EtOH NS and 70% EtOH NS scaffolds of equal elongation.

**Table 1**
Effective modulus of elasticity in the preferred and transverse directions and corresponding ratio of anisotropy for each type of scaffold. Values are mean ± SD.

| Nonsolvent EtOH | Scaffold elongation | Modulus (PD) (MPa) | Modulus (XD) (MPa) | Mechanical anisotropy |
|---|---|---|---|---|
| 0% | 0% | 1.18 ± 0.02 | NA | NA |
| | 35% | 1.43 ± 0.07 | 1.18 ± 0.05 | 1.21 |
| | 70% | 1.53 ± 0.05 | 0.83 ± 0.05 | 1.85 |
| 50% | 0% | 0.32 ± 0.02 | NA | NA |
| | 35% | 0.46 ± 0.04 | 0.44 ± 0.033 | 1.04 |
| | 70% | 0.57 ± 0.03 | 0.27 ± 0.07 | 2.12 |
| 70% | 0% | 0.18 ± 0.03 | NA | NA |
| | 35% | 0.27 ± 0.05 | 0.22 ± 0.04 | 1.23 |
| | 70% | 0.36 ± 0.02 | 0.18 ± 0.03 | 2.05 |

### 3.4. Scaffold lamination

Five scaffolds were laminated together to create a material with an increased thickness. The overall thickness was 825 ± 102.1 μm. A cross sectional view of the scaffold reveals a highly porous structure (Fig. 7). The lamination boundaries are undetectable.

## 4. Discussion

Aligned scaffolds have been shown to facilitate organization of cells in engineered cardiac tissue constructs [6]. Properties such as anisotropy and porosity have been shown to influence cell distribution and cellular alignment within scaffolds [28,29]. We have developed a method for fabricating sheet-like polyurethane scaffolds of tunable porosity and anisotropy. We hypothesized that post spray elongation of spray phase separation (SPS) scaffolds would generate scaffold anisotropy that would induce cellular alignment.

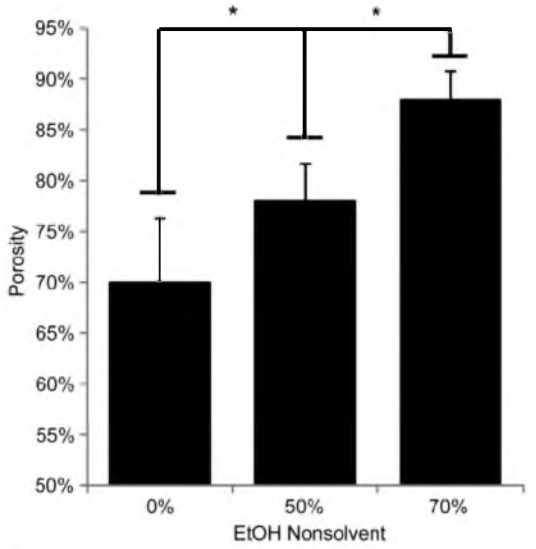


**Fig. 3.** Porosity of scaffolds fabricated with varying nonsolvent concentrations of EtOH ($n = 12$ for 0%, $n = 7$ for 50% and 70%).

Furthermore, we hypothesized that varying concentration of NS EtOH would permit alteration of scaffold porosity.

To test the hypothesis of tunable scaffold anisotropy we created frames that would elongate scaffolds after they had been sprayed. These frames were used to elongate the scaffolds 0%, 35%, or 70% of their initial length. SEM imaging revealed increasing numbers, length, and alignment of microfibers as the percent post spray elongation increased. Moreover, mechanical testing confirmed that scaffold stiffness increased in the direction of elongation as the percent elongation increased (Fig. 2). Cell culture experiments showed that cells mimicked the architecture of the scaffold filaments. Furthermore, as post spray elongation increased, the alignment of the scaffolds increased (Fig. 6).

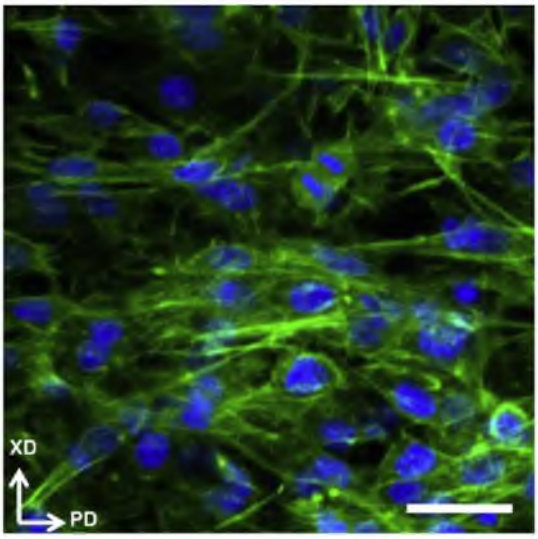


**Fig. 4.** Confocal image of aligned fibroblasts. Nulcei are stained blue with DAPI, and actin filaments are stained green with phalloidin. The preferred direction (PD) and transverse direction (XD) of the scaffold are indicated. Scale bar 20 μm.

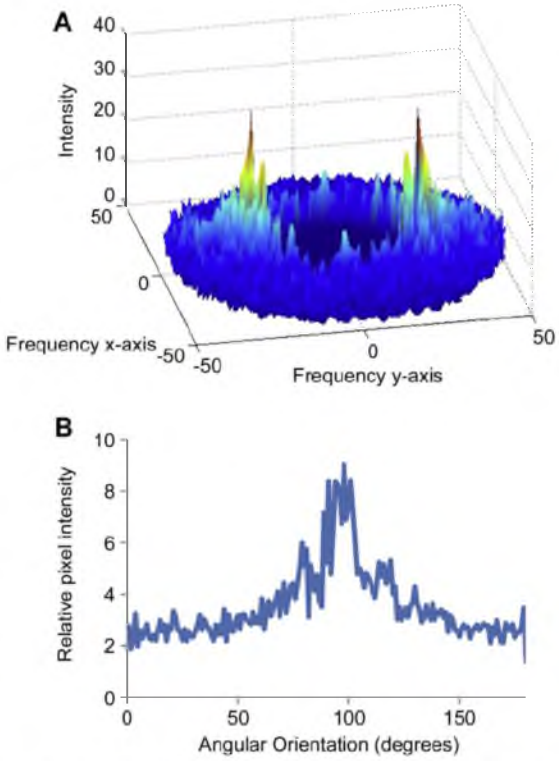


**Fig. 5.** (A) Surface plot of 2D FFT used to calculated alignment. Frequency values outside of 20–50 were removed to decrease signal artifacts. (B) Intensity angle plot. Preferred direction of the scaffold was at 90°. The intensity angle plot has been shifted by 90° to align the peak with the fiber direction.

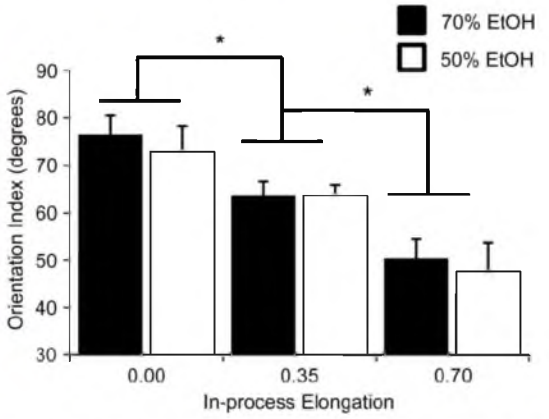


**Fig. 6.** Orientation index of porous scaffolds. Alignment in scaffolds of equal in-process elongation were similar, regardless of porosity. Scaffolds that underwent more in-process elongation had lower orientation indices indicating a higher degree of alignment.

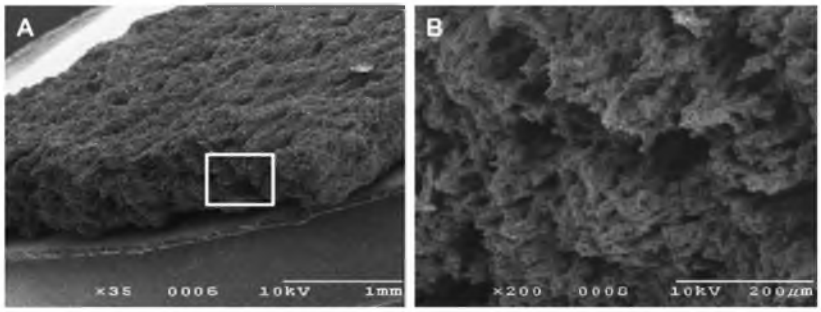


**Fig. 7.** Cross sectional SEM of laminated scaffold fabricated with 70% EtOH NS. Five sheets were laminated together to form this structure. The boxed region in A is magnified in B to show the microstructure of the scaffold.

In order to measure the effect of nonsolvent on scaffold porosity, three different nonsolvent solutions were used. Khorasani et al. reported that a 50% methanol; 50% water nonsolvent solution increased the porosity of SPS scaffolds [19]. They reported that the precipitation of polyurethane during a phase inversion is due partly to a nucleative mechanism, and partly to a spinodal mechanism. The very low solubility of polyurethane in water tends to force the mechanism towards a spinodal precipitation which forms a structure with fewer and smaller pores. A nonsolvent with alcohol allows the precipitation to follow the slower nucleative mechanism of precipitation. Our findings support those of Khorasani's group. In scaffolds fabricated with water as the NS, SEM imaging revealed relatively smooth topography with very few pores. However, increasing concentrations of EtOH in the NS showed increases in scaffold porosity as evidenced by the porosity testing (Fig. 3). Furthermore, mechanical testing showed that scaffolds made with higher EtOH NS had a lower effective modulus of elasticity, which is most likely due to the amount of space occupied by pores in the scaffold.

The composite laminated scaffold shows promise for future development of the SPS scaffold. Scaffolds were laminated together to form a thicker material. This method allows for development of scaffolds that have 3D anisotropy, similar to native cardiac tissue [30]. Further, the lamination boundaries become unidentifiable during the lamination process and the individual material does not separate at any regular boundaries.

While the results of this study are promising, there are some limitations that must be addressed in the future. We have demonstrated that this method for scaffold fabrication can be adapted to generate scaffolds that have a clinically relevant thickness for certain tissue types, however, these scaffolds will almost certainly have challenges associated with oxygen and nutrient diffusion through the scaffold [26]. Future studies will investigate development of composite laminates structures using the SPS fabrication method that include perfusion channels in the laminated structure to facilitate nutrient and oxygen diffusion. Furthermore, cellular alignment on elongated scaffolds was markedly better than on un-processed scaffolds, although the minimum orientation index measured in these studies ($50.3 \pm 5.2°$) was higher than the orientation index of right ventricular neonatal rat myocardium (approximately 39°) [6]. Higher levels of post-spray elongation may be used to increase cellular alignment and laminated structures may have individual plies aligned at different angles.

The assessment of mechanical properties is limited by the method used to quantify these properties. Stress values were used to calculate the effective modulus, however, these values are prone to error when using an elastic material that has large cross-sectional area changes as the material is elongated. Although we limited our elongation to 40% for force/displacement analysis this is still a limitation of the current study. Further, the cross-section is non-homogenous; it is comprised of polyurethane and void space, therefore the measured force can only be correlated to an effective stress of the bulk material. However, this method has been used to assess myocardial tissue [6] and one of our goals was to develop a scaffold that could approximate these values. In addition, we were interested in relative values as process parameters were changed in order to assess the impact of these changes. Therefore, an overall cross section was used to calculate relative stress values. Another limitation of our scaffold is the non-degradability of the polyurethane. However, the method described here may be adapted for use with degradable polyurethanes with only slight modification.

## 5. Conclusion

Sprayed phase separation is a simple, automated and repeatable method for fabricating sheets of porous scaffold materials. Porosity of these scaffolds may be tuned based on the percentage of EtOH in the NS. Post-spray elongation can be used to generate alignment and mechanical anisotropy within the scaffolds. Mechanical testing showed that the effective stiffness of the scaffold material may be altered based on both NS EtOH concentrations and post spray elongation. Cellular alignment can be influenced by the degree of post-spray elongation. Furthermore, we have demonstrated that this method can be used to form multilayer composite scaffold materials of varying thicknesses.

## Acknowledgments

This work was funded by the University of Utah Department of Bioengineering and by a Wayne Brown graduate research fellowship.

## Appendix

Figure with essential color discrimination. Figs. 4 and 5 of this article have parts that are difficult to interpret in black and white. The full colour images can be found in the on-line version, at doi:10.1016/j.biomaterials.2009.10.024.

## References

[1] Sands RW, Mooney DJ. Polymers to direct cell fate by controlling the microenvironment. Curr Opin Biotechnol 2007;18(5):448–53.
[2] Freed LE, Vunjak-Novakovic G, Biron RJ, Eagles DB, Lesnoy DC, Barlow SK, et al. Biodegradable polymer scaffolds for tissue engineering. Nat Biotechnol 1994;12(7):689–93.

[3] Venugopal J, Low S, Choon AT, Ramakrishna S. Interaction of cells and nanofiber scaffolds in tissue engineering. J Biomed Mater Res B Appl Biomater 2008;84(1):34–48.
[4] Ott H, Matthiesen T, Goh S, Black L, Kren S, Netoff T, et al. Perfusion-decellularized matrix: using nature's platform to engineer a bioartificial heart. Nat Med 2008;14(2):213–21.
[5] Courtney T, Sacks MS, Stankus J, Guan J, Wagner WR. Design and analysis of tissue engineering scaffolds that mimic soft tissue mechanical anisotropy. Biomaterials 2006;27(19):3631–8.
[6] Engelmayr Jr GC, Cheng M, Bettinger CJ, Borenstein JT, Langer R, Freed LE. Accordion-like honeycombs for tissue engineering of cardiac anisotropy. Nat Mater 2008;7(12):1003–10.
[7] Fromstein JD, Zandstra PW, Alperin C, Rockwood D, Rabolt JF, Woodhouse KA. Seeding bioreactor-produced embryonic stem cell-derived cardiomyocytes on different porous, degradable, polyurethane scaffolds reveals the effect of scaffold architecture on cell morphology. Tissue Eng Part A 2008;14(3):369–78.
[8] Guido S, Tranquillo RT. A methodology for the systematic and quantitative study of cell contact guidance in oriented collagen gels. Correlation of fibroblast orientation and gel birefringence. J Cell Sci 1993;105(2):317–31.
[9] Simpson D, Terracio L, Terracio M, Price R, Turner D, Borg T. Modulation of cardiac myocyte phenotype in vitro by the composition and orientation of the extracellular matrix. J Cell Physiol 1994;161(1).
[10] Goldsmith EC, Hoffman A, Morales MO, Potts JD, Price RL, McFadden A, et al. Organization of fibroblasts in the heart. Dev Dyn 2004;230(4).
[11] Eschenhagen T, Zimmermann WH. Engineering myocardial tissue. Circ Res 2005;97(12):1220–31.
[12] Charles-Harris M, del Valle S, Hentges E, Bleuet P, Lacroix D, Planell JA. Mechanical and structural characterisation of completely degradable polylactic acid/calcium phosphate glass scaffolds. Biomaterials 2007;28(30):4429–38.
[13] Radisic M, Park H, Gerecht S, Cannizzaro C, Langer R, Vunjak-Novakovic G. Biomimetic approach to cardiac tissue engineering. Philos Trans R Soc Lond B Biol Sci 2007;362(1484):1357.
[14] Huang NF, Patel S, Thakar RG, Wu J, Hsiao BS, Chu B, et al. Myotube assembly on nanofibrous and micropatterned polymers. Nano Lett 2006;6(3):537–42.
[15] Norman JJ, Desai TA. Control of cellular organization in three dimensions using a microfabricated polydimethylsiloxane-collagen composite tissue scaffold. Tissue Eng 2005;11(3–4):378–86.
[16] Zong X, Bien H, Chung CY, Yin L, Fang D, Hsiao BS, et al. Electrospun fine-textured scaffolds for heart tissue constructs. Biomaterials 2005;26(26):5330–8.
[17] Hollister SJ. Porous scaffold design for tissue engineering. Nat Mater 2005;4(7):518–24.
[18] Baker BM, Gee AO, Metter RB, Nathan AS, Marklein RA, Burdick JA, et al. The potential to improve cell infiltration in composite fiber-aligned electrospun scaffolds by the selective removal of sacrificial fibers. Biomaterials 2008;29(15):2348–58.
[19] Khorasani MT, Shorgashti S. Fabrication of microporous polyurethane by spray phase inversion method as small diameter vascular grafts material. J Biomed Mater Res A 2006;77(2):253–60.
[20] Moroni L, de Wijn JR, van Blitterswijk CA. 3D fiber-deposited scaffolds for tissue engineering: influence of pores geometry and architecture on dynamic mechanical properties. Biomaterials 2006;27(7):974–85.
[21] Kreitz MR, Webber WL, Galletti PM, Mathiowitz E. Controlled delivery of therapeutics from microporous membranes. I. Fabrication and characterization of microporous polyurethane membranes containing polymeric microspheres. Biomaterials 1997;18(8):597–603.
[22] Okoshi T, Chen H, Soldani G, Galletti PM, Goddard M. Microporous small diameter PVDF-TrFE vascular grafts fabricated by a spray phase inversion technique. ASAIO J 1992;38(3):M201–6.
[23] Rowlands AS, Lim SA, Martin D, Cooper-White JJ. Polyurethane/poly(lactic-co-glycolic) acid composite scaffolds fabricated by thermally induced phase separation. Biomaterials 2007 Apr;28(12):2109–21.
[24] Stankus JJ, Guan J, Fujimoto K, Wagner WR. Microintegrating smooth muscle cells into a biodegradable, elastomeric fiber matrix. Biomaterials 2006;27(5):735–44.
[25] Zhang C, Wen X, Vyavahare NR, Boland T. Synthesis and characterization of biodegradable elastomeric polyurethane scaffolds fabricated by the inkjet technique. Biomaterials 2008;29(28):3781–91.
[26] Papenburg B, Vogelaar L, Bolhuis-Versteeg L, Lammertink R, Stamatialis D, Wessling M. One-step fabrication of porous micropatterned scaffolds to control cell behavior. Biomaterials 2007;28(11):1998–2009.
[27] Ayres CE, Jha BS, Meredith H, Bowman JR, Bowlin GL, Henderson SC, et al. Measuring fiber alignment in electrospun scaffolds: a user's guide to the 2D fast Fourier transform approach. J Biomater Sci Polym Ed 2008;19(5):603–21.
[28] Dar A, Shachar M, Leor J, Cohen S. Cardiac tissue engineering optimization of cardiac cell seeding and distribution in 3D porous alginate scaffolds. Biotechnol Bioeng 2002;80(3):305–12.
[29] Costa K, Lee E, Holmes J. Creating alignment and anisotropy in engineered heart tissue: role of boundary conditions in a model three-dimensional culture system. Tissue Eng 2003;9(4):567–77.
[30] Helm PA, Tseng HJ, Younes L, McVeigh ER, Winslow RL. Ex vivo 3D diffusion tensor imaging and quantification of cardiac laminar structure. Magn Reson Med 2005;54(4):850.

# CHAPTER 4

# ENGINEERED CHANNELS ENHANCE CELLULAR DENSITY IN PERFUSED SCAFFOLDS

Reprinted from Acta Biomaterialia, Vol 7 Issue 11, Kennedy, J. P. McCandless, S. P. Rauf, A. Williams, L.M. Hillam, J. Hitchcock, R. W, Engineered channels enhance cellular density in perfused scaffolds 3896-3904, (2011), with permission from Elsevier

Acta Biomaterialia 7 (2011) 3896–3904

Contents lists available at ScienceDirect

Acta Biomaterialia

journal homepage: www.elsevier.com/locate/actabiomat

# Engineered channels enhance cellular density in perfused scaffolds

J.P. Kennedy, S.P. McCandless, A. Rauf, L.M. Williams, J. Hillam, R.W. Hitchcock *

*Department of Bioengineering, University of Utah, Salt Lake City, 84112 UT, United States*

ARTICLE INFO

*Article history:*
Received 8 December 2010
Received in revised form 18 May 2011
Accepted 22 June 2011
Available online 28 June 2011

*Keywords:*
Scaffold
Perfusion
Polyurethane
Shear stress
Hydraulic permeability

ABSTRACT

Scaffold-based tissue engineering provides cells with an engineered matrix to enhance and direct cell attachment, proliferation and differentiation. One critical limitation to current tissue engineering approaches is the inability to create densely populated constructs thicker than a few 100 μm. We hypothesized that development of porous, channeled scaffolds would increase cell density and uniformity of their spatial distribution through scaffold channel perfusion. Patterned polyurethane sheets were fabricated using a sprayed phase separation technique and laminated together to form 1.5 mm thick channeled scaffolds. Hydraulic permeability testing confirmed the presence of functional channels throughout the multilaminate construct. A continuous flow bioreactor was used to perfuse the construct with medium during the culture period. Cross-sectional cell densities and spatial uniformities were measured in channeled and nonchanneled scaffolds under different seeding and culture conditions. Channeled scaffolds were found to have higher densities of human mesenchymal stem cells than nonchanneled samples. Perfused scaffolds had more uniform spatial distribution of cells within the scaffold compared to statically cultured scaffolds. In conclusion, we have shown the channeled scaffolds to be a promising approach toward creating thick tissue-engineered constructs.



## 1. Introduction

The design and preparation of functional tissue is a primary goal of tissue engineering (TE). Once prepared, *in vitro* engineered tissue can be used for treatment of diseased or damaged tissue, pharmacological screening, or research on molecular mechanisms and developmental biology [1–3]. TE harnesses the regenerative capacity of cells to assemble functional tissue and utilizes the engineering paradigm to design and create appropriate environments for developing engineered tissue. Cells require stimuli such as soluble chemical signals (e.g. oxygen, cytokines, nutrients), cell–cell/cell–extracellular matrix (ECM) adhesion [4,5], mechanical forces (e.g. shear stress, strain) [6,7], surface interactions (e.g. texture, architecture, surface energy) [8,9] and electrical stimulation [10,11] to develop into functional tissue. In tissue culture environments, soluble chemical signals are found in culture media, bioreactors can provide mechanical and electrical stimulation, and scaffolds provide a provisional matrix that can be supplemented or replaced by cell expressed ECM over time. Currently, one major challenge facing tissue engineers is the limitation of relying on diffusion to deliver soluble chemical factors. Without enhanced transport, metabolically active cells deeper than about 100 μm do not receive sufficient soluble chemical signals, nutrients and oxygen [12]. They are unable to survive beyond the diffusive limits of a nutrient source, and therefore are unable to assemble functional tissue [13]. For tissue such as cardiac muscle, contractile force is directly correlated to the thickness and cellular density of the construct [14]. The limitation of construct size has hindered development and clinical application of tissue-engineered constructs.

To overcome diffusion related limitations, there are two general approaches. One approach aims to increase the effective diffusive length, which will allow cells deeper within a construct to exchange sufficient nutrients and waste for survival. The effective diffusion distance can be increased through the use of hydrogels [15] and increased porosity [16], and with the use of specialized carriers, such as perfluorocarbons, to increase the concentration of oxygen in the medium [17].

Another approach to overcoming diffusional limitations utilizes convective transport (perfusion) to bring nutrient-rich medium nearer to the cells, thus decreasing the need for long-range diffusion. Perfusion can occur either *in vivo*, through the host's cardiovascular system, or *in vitro*, through a perfusion bioreactor. In the *in vivo* case, pre-vascularized constructs have been employed to facilitate vascular perfusion [1,18,19]. Prevascularization utilizes a combination of cells, structures and signals to facilitate and accelerate functional anastamosis upon implantation [20,21]. In vitro perfusion has been accomplished by pumping medium either transmuraly, through porous scaffolds, or through channel networks [22–26]. Further development of perfusion-based TE technologies may provide a solution to the challenges associated with construct size.

* Corresponding author. Tel.: +1 801 557 7393.
*E-mail address:* r.hitchcock@utah.edu (R.W. Hitchcock).

1742-7061/$ - see front matter © 2011 Acta Materialia Inc. Published by Elsevier Ltd. All rights reserved.
doi:10.1016/j.actbio.2011.06.037

One advantage of the perfusion approach is the high degree of control that can be designed into the system. The primary variables that affect mass transport are the perfusion rate and the scaffold configuration. Scaffold perfusion models predict that oxygen gradients can be altered through judicious design of scaffold properties and perfusion rates [27–29]. One scaffold property that has been studied in these models is a network of engineered channels within the scaffold. Channels for perfusion have been proposed to provide an *in vivo*-like oxygen supply to cells [30]. Convective transport through a channel array can bring nutrients and oxygen near enough to cells to allow sufficient diffusion-based exchange to promote cell viability. This approach is inherently biomimetic as it uses a vasculature-like array to provide local exchange of metabolites and waste products to and from cells within a thick tissue [22,23]. Moreover, channels can be used to endow a scaffold with geometric and mechanical cues that direct cellular alignment [25]. In addition, channels may help shield cells from shear stresses associated with perfusion, which have been shown to be detrimental to some cell types [17,31]. Overall, engineered channels for perfusion are a promising platform for overcoming diffusion related problems in tissue engineering.

Scaffolds, in addition to their role in helping meet metabolic requirements, must meet certain performance and compatibility requirements, such as porosity, stiffness and anisotropy. Scaffolds that can be engineered to meet these requirements are key to developing platforms for creating functional engineered tissue. The ability to create a scaffold that not only facilitates sufficient transport of metabolites, but also allows the engineer to control key design requirements will likely be a necessary tool for successful scaffold-based technologies. Development of an engineered construct that is clinically useful will depend on successful engineering designs that meet all of these requirements and likely more.

Our group has recently developed thin sheet scaffolds made from polyether urethane (PU) and shown that they can be engineered with specific porosity, stiffness and anisotropy [32]. In addition, these materials induce cellular alignment via scaffold microarchitecture and can be laminated to form thick structures. In this paper we investigate a channel-based method to enhance transport and seeding efficiency within thick cell-laden constructs. Our goal is to develop a channeled scaffold for use with perfusion culture. It has been shown that perfusion seeding and culture of thick constructs will enhance the density and uniformity of tissue-engineered constructs [24,27,30]. We hypothesize that engineered channels within the scaffolds will further increase the cell density of perfused constructs. Here, we report methods to design and fabricate channels in laminate PU scaffolds, and *in vitro* testing of these channels to evaluate cell density and uniformity.

## 2. Methods

### 2.1. Scaffold fabrication

Scaffolds were fabricated using a sprayed phase separation technique. We have previously shown that PU fabricated through sprayed phase separation can provide a porous structure that facilitates cell attachment and proliferation [32]. For this study, we used 4% (w/v) PU dissolved in dimethylacetamide. To create porous sheets, 70% ethanol (EtOH) was selected as the nonsolvent [33]. This solvent was sprayed at a rate of 7.0 g $min^{-1}$ ± 10%, while the nonsolvent was sprayed simultaneously at a rate of 14.0 g $min^{-1}$ ± 10% onto a patterned silicone substrate. Spray nozzles were mounted onto an xyz control robot (MaxNC 12, Gilbert, AZ), and the spray pattern and time was controlled using a custom-written code.

Polyester frames were designed in order to enhance handleability of the scaffolds. Thin polyester film (0.25 mm thick) was cut into a 9 × 6 matrix of frames using custom code and a knife plotter (Graphtec, Santa Ana, CA). Each frame consists of a 13 × 20 mm window where the scaffold is deposited, two tabs for scaffold adherence and alignment holes for facilitating lamination (Fig. 1A). Immediately after spraying, the frames (with the scaffold attached) were removed from the substrate. Scaffolds were laminated using the alignment holes in the frame (Fig. 1B) and custom lamination tooling. After lamination, scaffolds were allowed to cure overnight in a bath of deionized water at room temperature to insure constant humidity during solvent removal.

In order to create perfusion channels within the scaffolds, the PU solution was sprayed onto a silicone substrate with the desired channel configuration patterned onto its surface. The channel configuration was designed using three-dimensional (3-D) design software (SolidWorks, Concord, MA). A mold for this configuration was then fabricated using a 3-D printer (Objet, Billerica, MA). Low viscosity, two-part Pt cure silicone (VST-50, Factor II, Lakeside, AZ) was poured into the mold and allowed to cure at 40 °C overnight. The silicone was then removed from the mold and used as the patterned spray substrate.

Two different channeled and one nonchanneled configurations were fabricated. Both channel configurations had a nominal depth and pitch of 350 and 875 μm respectively. The larger channel configuration had channels with a nominal width of 500 μm, while the smaller had a nominal channel width of 200 μm (Fig. 2). These widths were chosen based on the capability of the 3-D printer and to provide a range of channel widths comparable to other reported channeled scaffolds [24,25].

### 2.2. Scaffold characterization

Mechanical properties were measured for both channeled and nonchanneled scaffolds. A sample was removed from the center of each scaffold for mechanical testing ($n = 4$). The test specimens measured 16.0 × 5.0 mm. They were tested on an Instron 3342 (Instron, Norwood MA) with a 50 N load cell. 2 mm was gripped in each grip, resulting in a gauge length of 12 mm. The samples were tested to 40% strain at a speed of 20 mm $min^{-1}$. The effective stress for each sample was calculated by dividing the force by the overall initial cross-sectional area over the linear range of the stress–strain curve (from 10% to 40%). From the effective stress and strain data an effective modulus of elasticity was calculated.

Porosity was determined by gravimetric and dimensional analysis for both channeled and nonchanneled scaffolds ($n = 4$), as described previously [32,33]. Briefly, the total volume ($V_{total}$) of the scaffold was calculated by measuring the dimensions ($l$, $w$, $h$) of rectangular scaffold samples (approximately 15 × 5 × 1 mm). The mass of the scaffold samples ($m_{scaffold}$) was then used in conjunction with the specific gravity ($\rho_{PU}$) of Tecoflex SG80 PU (1.04 g $cc^{-1}$) to determine the volume of PU in the sample. The void volume is the difference between the total volume and the volume occupied by PU in the scaffold. The porosity was calculated by

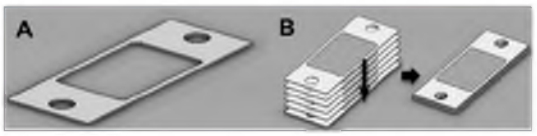


**Fig. 1.** (A) Polyester frame used to enhance handleability of scaffold. (B) Schematic of lamination procedure. Six scaffolds (approximately 0.25 mm thick each) were laminated after spraying and cured together to form a single thick scaffold (~1.5 mm).

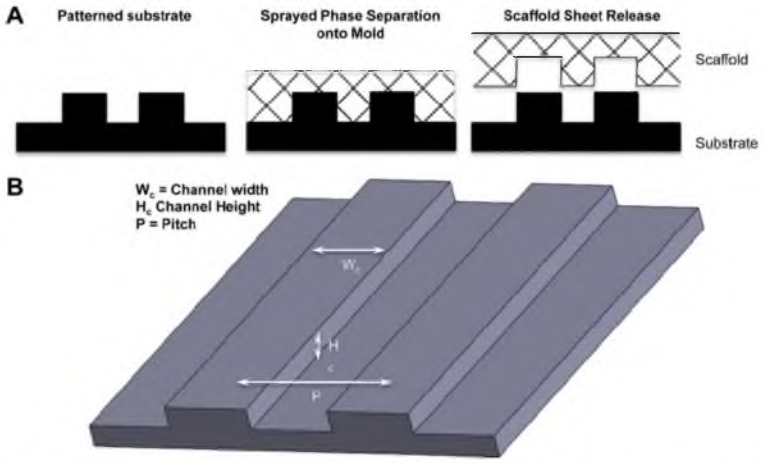


**Fig. 2.** (A) Patterned substrates were fabricated from polydimethyl siloxane cast in a mold generated by a 3-D printer. Scaffold material was deposited on top of the patterned substrate using the sprayed phase separation technique. (B) Channel properties, including channel width, height and pitch, were determined by the geometry of the substrate.

dividing the void volume by the total volume of the scaffold as shown in Eq. (1):

$$\text{Porosity} = \frac{V_{\text{total}} - \frac{m_{\text{scaffold}}}{\rho_{\text{PU}}}}{V_{\text{total}}} \quad (1)$$

### 2.3. Electron microscopy imaging of scaffolds

Perfusion channels were visualized using electron microscopy (EM). Single sheets and cross-sections were imaged. In order to image the cross-section of a scaffold, the scaffold was frozen in liquid nitrogen, and then fractured in order to not damage the internal structure. Scaffolds were then mounted on conductive carbon tape and sputter coated for 45 s with a thin layer of gold using a Pelco SC-7 sputter coater. Samples were imaged using a Hitachi S2460 scanning electron microscope at 10 kV.

### 2.4. Hydraulic permeability of scaffolds

Hydraulic permeability was measured in channeled and non-channeled scaffolds. A custom silicone (VST 50, Factor II) connector was molded to allow the scaffolds to be connected to standard Luer style fittings (Fig. 3). The scaffold was sealed in the connector using silicone in order to prevent fluid from leaking around the scaffold. The outside of the scaffold was also sealed using a PU tape coated with silicone, insuring that all of the water that entered the scaffold exited out of its distal end. The scaffold was coupled in series with a water reservoir to an ER 3000 pressure generator (Tescom, Elk River, MN) and the pressure was controlled using the ER 3000 software. Water was perfused through the scaffold and collected as it exited the scaffold. The flow rate of water was measured gravimetrically. The hydraulic permeability ($k$) is defined as the flow rate ($Q$) normalized to the pressure ($P$) and cross-sectional area ($A$) of the scaffold, similar to Kreitz et al. [34]:

$$k = \frac{Q}{P \cdot A} \quad (2)$$

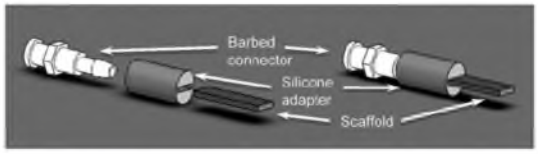


**Fig. 3.** A custom-molded silicone adapter was used to couple the scaffold with a barbed nylon connector. The scaffold was sealed into the silicone adapter to prevent leaking. The nylon connector included a female Luer fitting for facile coupling of the scaffold to both the pressure generator for HP testing and the perfusion bioreactor.

### 2.5. Perfusion bioreactor

A custom perfusion bioreactor was developed in order to perfuse scaffolds with medium during cell culture experiments. A T-75 tissue culture flask was modified using a CNC mill to include the following elements: six mounting holes for scaffolds, a window for scaffold loading and a drain hole (Fig. 4A). Barbed, female Luer connectors, which serve as inlets and as attachment points for the scaffolds, were mounted and sealed with Loctite 3311 UV cure adhesive in the six mounting holes. A polyester film with an adhesive border was mounted on the window in order to maintain sterility during culture while allowing for scaffold loading similar to Lasher et al. [35]. A piece of 7 mm inner diameter Tygon tubing was mounted to the drain hole using Loctite 3311 UV cure adhesive and an ABS collar for stress relief. The drain height was positioned such that the medium would be above the scaffolds insuring complete submersion during culture. After assembly, the modified T-flask was sterilized using ethylene oxide (ETO). The manifold comprised 2.0 mm inner diameter Tygon tubing split with a standard barbed Y connector to three outlets. Two pump heads were mounted on the peristaltic pump; each head supplied medium to three scaffolds mounted in the T-flask. The manifold was coupled to the reservoir, which was in turn fed by the drain from the T-flask; thus medium was recycled through the system (Fig. 4B). The reservoir and manifold were sterilized using ETO. The entire bioreactor, including the pump, reservoir, manifold and T-flask, was kept in an incubator at 37 °C with 5% $CO_2$.

Medium from a reservoir was pumped at a rate of 3 ml $min^{-1}$ through the manifold to six different scaffolds using a peristaltic pump with two pump heads. The fluid velocity in the channels was calculated to be 2.78 mm $s^{-1}$. This velocity corresponds to a wall shear stress of 0.31 dyn $cm^{-2}$, which is similar to values that

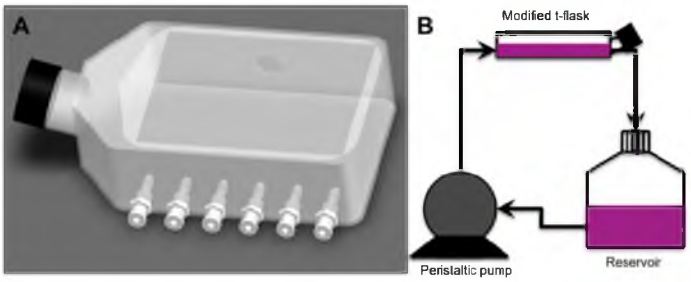


**Fig. 4.** (A) The culture chamber included six barbed connectors for mounting scaffolds. A window was cut in the top of the t-flask for loading scaffolds, and a film with a weakly adhesive border was used to close the window in order to maintain sterility. A drain was installed on the opposite side of the flask. (B) Schematic of the perfusion bioreactor. Medium was pumped from a reservoir using a peristaltic pump to the culture chamber. Drainage from the culture chamber was recycled back to the reservoir.

have been shown to be acceptable for cells sensitive to shear stress (cardiomyocytes) [17].

### 2.6. Cell seeding and culture

Human mesenchymal stem cells (hMSCs) were grown in a T-flask prior to seeding. Cell culture medium was composed of Dulbecco's modified Eagle's medium (DMEM; Fisher Scientific, Waltham, MA) supplemented with 10% fetal bovine serum (FBS), 2 nM L-glutamine and 50 μl $ml^{-1}$ streptomycin 50 U $ml^{-1}$ penicillin (Invitrogen, Carlsbad, CA) [36]. Prior to seeding, scaffolds were sterilized with ETO. Scaffolds were immersed in 70% EtOH in order to wet all the pores. Scaffolds were then rinsed three times with sterile PBS to remove the EtOH. Following wetting and rinsing, scaffolds were immersed in culture medium for 24 h in order to condition the scaffold with FBS proteins. After conditioning, the medium was removed and the cells were seeded onto the scaffolds using one of two methods. Surface-seeded scaffolds were seeded by placing 500 μl of $1.85 \times 10^6 \pm 0.43 \times 10^6$ cells $ml^{-1}$ cell suspension on the surface. Perfusion-seeded scaffolds were seeded by flowing 500 μl of $1.85 \times 10^6 \pm 0.43 \times 10^6$ cells $ml^{-1}$ cell suspension through the scaffold using a syringe coupled to the silicone connector over 1 min. Experimental groups of channeled (500 μm only) and nonchanneled scaffolds ($n = 3$ of each type) were tested for static culture surface seeding, static culture perfusion seeding, perfusion culture surface seeding and perfusion culture perfusion seeding. After a 1 h attachment period, all scaffolds were submerged in fresh medium. Static culture specimens were cultured individually in cell culture dishes with a medium volume of 9 ml. The medium was exchanged five times for the static culture samples. Two hours after seeding, perfusion of the dynamic culture was commenced at a rate of 3 ml $min^{-1}$. Perfusion cultured samples used 250 ml of medium that was recycled through the bioreactor. The total volume of medium used per scaffold in both culture conditions (static and perfused) was 45 ± 3 ml. Cells were cultured for a total of 7 days.

### 2.7. Cell distribution analysis

After the 7 day culture period cells were fixed overnight at 4 °C with 4% paraformaldehyde. The scaffolds were then equilibrated in a 30% sucrose solution (Fisher Scientific) overnight. After equilibration, scaffolds were covered with tissue-freezing medium (Triangle Biomedical Sciences Inc., Durham, NC) overnight. Thin cross-sections (100 μm) of the scaffold were obtained using a Leica 1950 CM cryostat (Leica Microsystems, Wetzlar, Germany). Nuclei of cells in the thin sections were then fluorescently stained with 4′,6-diamidino-2-phenylindole (DAPI). Cells were imaged with an Olympus FV 1000 confocal microscope (Olympus, Center Valley, PA). Custom-written Matlab code was used to quantitate the number of cells in eight equally spaced regions of the scaffold from one surface to the opposite surface. Manual cell nuclei counts were obtained and compared to output from the Matlab code in order to validate the program. Automated cell counts were within 2% of manual cell counts. Both cell number and uniformity are presented. The percentage of cells ($n_i$) in each segment was used to calculate the uniformity index (UI), as shown in Eq. (3). For this, 12.5% (the value representing a perfectly uniform distribution for eight segments) was subtracted from the percentage of cells in each segment. The data was normalized by dividing it by 175, the maximum value for a non-uniform distribution:

$$UI = 1 - \frac{\sum_{i=1}^{8} |n_i - 12.5|}{175} \tag{3}$$

### 2.8. Statistics

A single-factor analysis of variance ($\alpha = 0.05$) was used to compare cell uniformity and cell density values for the different seeding and culture conditions. Unpaired *t*-tests were used to assess the significance of the mechanical properties, porosity, cell uniformity, density and hydraulic permeability of scaffolds.

## 3. Results

### 3.1. Scaffold dimensions and mechanical testing

Six individual polyurethane sheets were laminated to create each scaffold. These laminated scaffolds were 1.17 ± 0.13 mm thick. Mechanical testing showed no difference between the modulus of 500 μm channeled and nonchanneled scaffolds with moduli of 0.251 ± 0.011 and 0.268 ± 0.048 MPa respectively ($p = 0.49$). No significant difference in overall scaffold porosity was determined (72 ± 1 vs. 70 ± 3%, 500 μm channeled and nonchanneled respectively, $p = 0.30$). EM imaging of individual sheets revealed that they were similar to the pattern of their substrate (Fig. 5). The pitch measured from EM images was 871 ± 24 μm. The larger channels were measured to be 489 ± 37 μm wide, and the smaller channels were measured to be 205 ± 8 μm wide. EM imaging of the scaffold cross-sections did not obviously reveal the presence of channels. The scaffolds were excised from the frames after lamination, and cut in half for testing. The final scaffold dimensions were 6 × 16 mm.

### 3.2. Hydraulic permeability

Hydraulic permeability was assessed using three different channel configurations: nonchanneled scaffolds, 200 μm wide channels

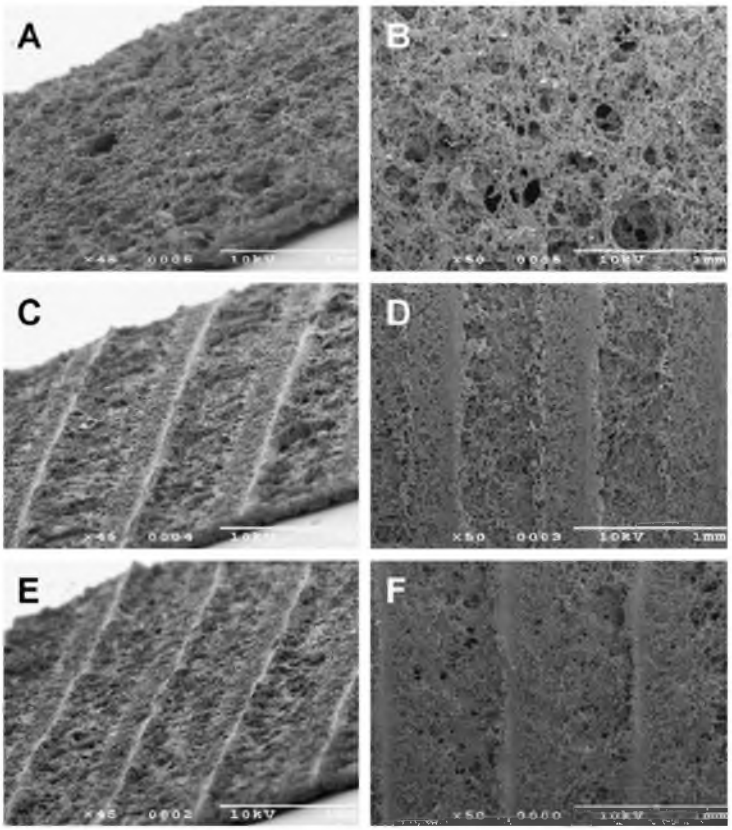


**Fig. 5.** SEM imaging of scaffold sheets sprayed with no channels (A, B), 250 μm channels (C, D) and 500 μm channels (E, F). The channel dimensions match those of the patterned substrate. Scale bars are 1 mm.

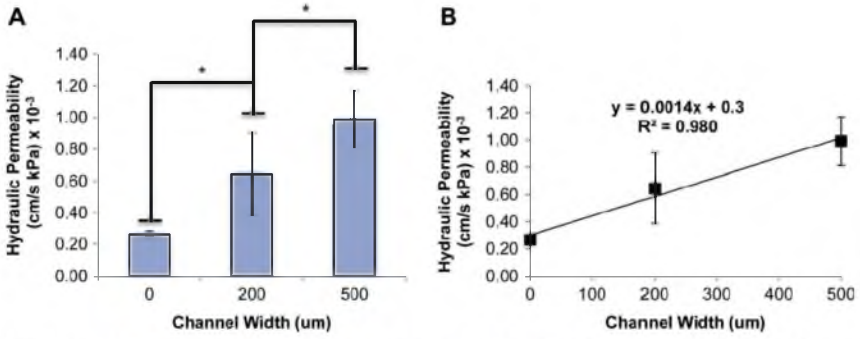


**Fig. 6.** (A) HP for the three different scaffolds that were tested. (B) A linear plot of this data indicates that the HP is linearly related to the channel width ($R^2 = 0.980$).

and 500 μm wide channels. A pressure of 6.8 kPa (1 psi) was used to perfuse scaffolds with DI water. The hydraulic permeability of the scaffolds increased as channels were added, and as the channel width increased ($p < 0.05$, Fig. 6A). Hydraulic permeability appeared to increase linearly with channel width ($R^2 = 0.980$, Fig. 6B) over the range of channel width that was measured.

### 3.3. Cell uniformity

Thin scaffold cross-sections were prepared as described and stained with DAPI to image the cell nuclei (Fig. 7). Cell uniformity was quantified and assessed using a cell uniformity index. The cell uniformity increased ($p < 0.05$) from static culture (both surface

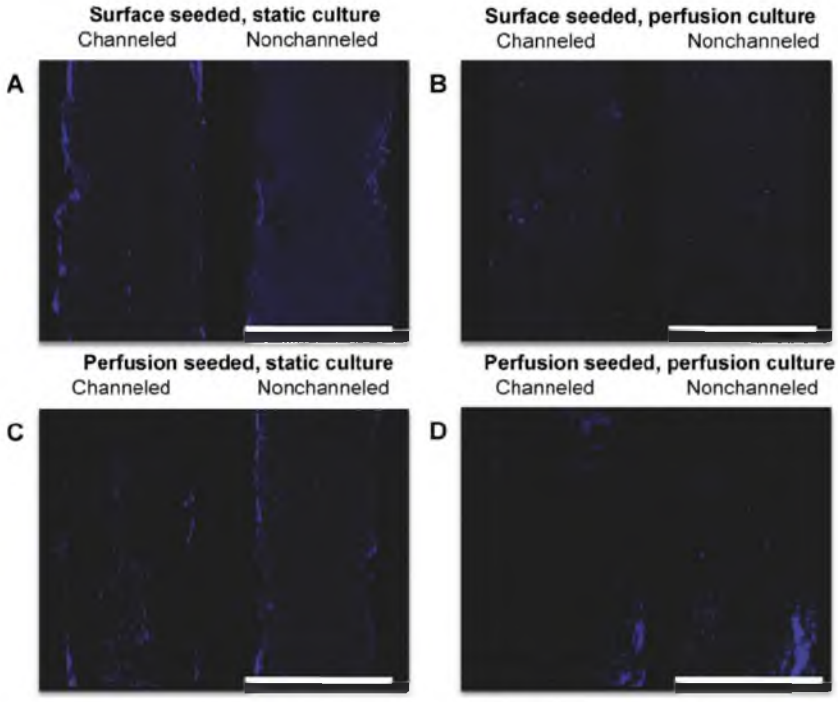


**Fig. 7.** Cross-sectional images of constructs. Cell nuclei were stained with DAPI. Cells were either surface seeded (A, B) or perfusion seeded (C, D). Cells were cultured for 7 days statically (A, C) and in a perfusion bioreactor (B, D). Scale bars are 1.5 mm.

and perfusion seeding methods) to perfusion culture for channeled scaffolds. Cells were detected on both sides of the surface-seeded scaffolds. This can be attributed in part to the flow of the cell suspension upon seeding. Since the scaffolds were wetted before seeding, the addition of a 500 μl cell suspension resulted in the relatively uniform distribution of the suspension around the entire surface of the scaffold. Among the statically cultured samples, the uniformity was higher, though not significantly, in the perfusion-seeded samples than in the surface-seeded samples. The uniformity of cell distribution did not change between the channeled and nonchanneled scaffolds in each group.

The percentage of total cells found in each region of the scaffolds was also evaluated. In all cases, the largest percentage of cells was found closer to the surface, while the centermost regions generally contained the smallest percentage of cells. In surface-seeded scaffolds, the outermost regions contained 74.0% of total cells. In perfusion-seeded, statically cultured scaffolds, this percentage dropped to 57.4%. Perfusion-seeded scaffolds that were perfused with medium during culture contained only 39.3% of total cells in the two outermost regions (Fig. 8B).

### 3.4. Cell density

The number of cells in each scaffold segment was calculated using custom Matlab code, allowing for comparison of cell density between different cell seeding and culture conditions. In perfusion-seeded, channeled scaffolds, the number of cells increased from static culture to perfusion culture by 30%, though this increase was not significant ($p = 0.139$) (Fig. 9). Surface-seeded scaffolds had significantly lower cell densities than perfusion-seeded constructs at the end of the 7 day culture period (Fig. 9). In all cases, channeled scaffolds contained more cells than nonchanneled scaffolds. Specifically, channels improved cell density in perfusion-seeded scaffolds by 105% and 70% in perfusion culture and static culture, respectively ($p < 0.05$).

## 4. Discussion

Creating thick tissue-engineered constructs is paramount for developing useful TE technologies. An overwhelming limitation of current TE platforms is the inability to transport sufficient nutrients and waste through diffusion only. In order to enhance mass transport, several groups have perfused cell-seeded constructs with cell culture medium [26,27]. We hypothesized that development of scaffolds designed for perfusion may further increase the advantages of these perfusion systems.

In order to create scaffolds designed for perfusion, we used a sprayed phase separation technique to create thin patterned sheets. The pattern from the molded substrate was shown by EM microscopy to be effectively transferred to the scaffold sheet by the spray phase separation technique (Fig. 5). However, when the patterned sheets are laminated, channels are not obviously visible using EM techniques. In order to verify that the channels in fact exist, hydraulic permeability testing methods were employed. Hydraulic permeability (HP) measures the inverse of resistance to flow within the scaffold, which is expected to be directly related to channel dimensions and porosity. Indeed, we found that as the channel dimensions increased, so did the HP. We observed that HP was anisotropic, that is, the scaffold was much more permeable in the direction of the channels than through the interconnected porous matrix. This leads to two important conclusions: (i) the channels create hydraulic anisotropy after lamination; and (ii) we are able to engineer the HP of these scaffolds based on the original mold dimensions.

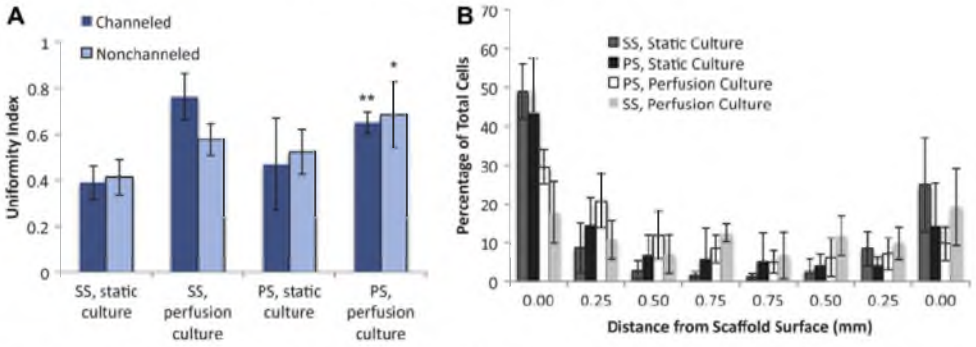


**Fig. 8.** Spatial image analysis was performed on the cross-sectional cell images using custom-written Matlab code. (A) Uniformity index value range from 0 to 1, with 1 being a perfectly uniform spatial distribution. There were no significant differences in statically cultured samples. **Significant difference from all preceding samples. *Significant difference between surface-seeded, static-cultured samples. (B) The percentage of total cells found in eight regions of the scaffold (ranging from one surface to the opposite surface). There was no difference between channeled and nonchanneled.

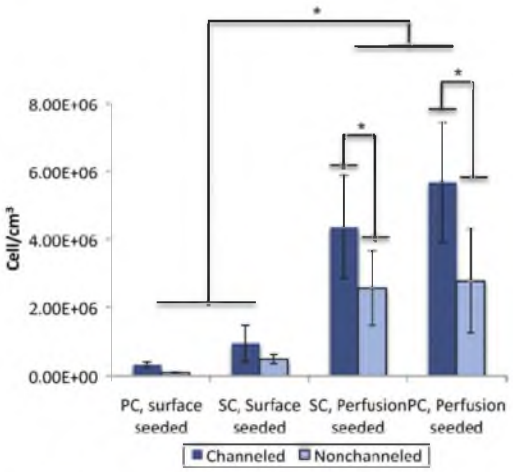


**Fig. 9.** The cell density was calculated using a custom Matlab program. The cells in each cross-section were counted and divided by the volume of the cross-section. Perfusion seeding results in higher cell densities than surface seeding. Channeled scaffolds, when perfusion seeded, were found to have significantly higher cell numbers than nonchanneled scaffolds.

When normalized to the length of the material, the HP of the scaffolds we report ranges from $2.40 \times 10^{-8}$ to $1.14 \times 10^{-7}$ $m^4N^{-1}s^{-1}$. Kreitz et al. [34] measured the HP of a sprayed phase-separated polyurethane film. Based on the spray parameters, they were able to achieve HP ranging from $1.31 \times 10^{-8}$ to $7.83 \times 10^{-8}$ $m^4N^{-1}s^{-1}$. Okoshi [37] used a sprayed phase-separation method to create polyurethane–polydimethylsiloxane scaffolds. These thin sheets had HP ranging from 0 to $1.02 \times 10^{-7}$ $m^4N^{-1}s^{-1}$. A woven PGA scaffold reported by Moutos et al. had HP ranging from $4.00 \times 10^{-16}$ to $1.00 \times 10^{-15}$ $m^4N^{-1}s^{-1}$.

The effective modulus of the laminate scaffold we report is 0.25 and 0.27 MPa for channeled and nonchanneled scaffolds respectively (the difference is not significant). The corresponding modulus for anisotropic sheets fabricated by the same method prior to lamination is 0.18 MPa [32]. The reason for the difference is likely due to changes in porosity. Indeed, the individual sheets measured previously had a porosity of 88%, whereas the laminated scaffolds used in this publication had an average porosity of 71%. Extruded (nonporous) Tecoflex polyurethane is reported by the manufacturer to have a modulus of 2.08 MPa at 100% elongation.

Radisic et al. [17] developed a model that predicts the oxygen distribution within perfused scaffolds. One important conclusion drawn from this model is that fluid velocity is an important variable in determining the spatial distribution of oxygen within a tissue-engineered construct. For Poiseuille flow in tubes, the shear stress ($\tau$) can be calculated as:

$$\tau = \eta \frac{4V_{fluid}}{R} \tag{4}$$

Increasing the radius ($R$) of the space through which the fluid is passing (i.e. the channel diameter or the pore size) allows for increased fluid velocity, while maintaining a constant shear stress. This indicates that one approach to meet the metabolic demands of a large tissue construct involving cells that are sensitive to shear stress may be to create channels of relatively greater diameter than that of pores in the matrix. This would effectively allow for increased fluid velocity, which would in turn enhance the convective transport of metabolites within the construct.

Cell density was shown to be affected by the HP of the scaffold and the seeding conditions, but, notably, not by the culture conditions. Perfusion seeding was shown to increase cell density in both channeled and nonchanneled scaffolds. It has previously been demonstrated that enhanced seeding techniques can result in much higher seeding efficiencies than surface seeding [7,24,38,39].

Surface seeding, whether in static culture or perfusion culture, resulted in relatively low cell densities. For perfusion cultured samples, the uniformity was high; however, this value is subject to large changes based on few cells since the cellular density was low.

Perfusion seeding resulted in increased cell density at the end of culture, but notably the difference between the perfused and statically cultured samples was not significant. This may be due to the relatively short culture time (7 days). The average density increased by 30% ($p = 0.139$) from static to perfusion culture.

Further, scaffolds with 500 μm channels had significantly higher cell density than nonchanneled scaffolds. Since the overall porosity of the scaffolds was not different, there may be other factors involved. One factor may be local shear stresses in the scaffold. As shown in Eq. (4), the shear stress increases with decreasing radius of the flow path. Perfusion of channeled scaffolds involves medium flowing through both the channels and the pore network, while perfusion of nonchanneled scaffolds results in flow through only the pore network. The dimensions of the channels are much larger than the dimensions of the interconnected pore network;

therefore, the shear stress associated with perfusion in channeled scaffolds may be much less than in nonchanneled scaffolds. Channeled scaffolds may result in lower local shear stresses during perfusion, which may then be responsible for conditions more amenable to cell attachment, proliferation and survival. During perfusion of a nonchanneled scaffold, the cells may experience higher shear stresses that hamper attachment, proliferation or survival, or a combination of these.

Cellular distribution uniformity was significantly affected by culture conditions, but surprisingly not by scaffold configuration. Scaffolds with and without channels had no recognizable change in cell uniformity in spite of the large difference in cell number. This seems to indicate that the perfusion of nonchanneled scaffolds creates suitable conditions for cell survival uniformly within the scaffold. However, channels may affect cell attachment, proliferation or nutrient diffusion, or a combination of these.

These studies were performed using mesenchymal stem cells. Constructs were conditioned with FBS proteins in order to enhance cell adhesion. The flow rate for seeding and perfusion was based on nominal literature values and system limits; however, these variables may have profound effects on the cell uniformity and cell density within the engineered constructs. The system that is described in this paper can be used to explore the effect of flow rate on many different cell types. Moreover, different conditioning procedures may be utilized, and their effects on construct density and uniformity can be evaluated.

## 5. Conclusion

In this paper we report the use of perfusion in thick tissue constructs to enhance cell distribution and increase cell density. We discovered that, in addition to perfusion, the presence of perfusion channels in the scaffolds has a significant effect on cell density and distribution independent of seeding and perfusion culture conditions. This finding provides additional insight into the role of channels and networks to seed and sustain *in vitro* tissue constructs.

Our ability to seed, grow and maintain engineered tissue is limited by diffusional gradients across sections of tissue thicker than a few 100 μm. In native tissue this is overcome with vascularized networks. In cultured tissue, however, vascular networks are not always present or even desired. We present a means to engineer and specify channel geometry in 3-D scaffold materials as a design variable that can play an important role in the ultimate structure and function of engineered tissue. This design capability provides engineers with the ability to manipulate the environmental conditions as well as the flow, perfusion and clearance of thick 3-D constructs. Scaffold perfusion requires specialized bioreactors that can house, protect and provide flow to the scaffold perfusion network. Because of the intimate relationship between perfusion scaffolds and bioreactors, these two elements should be designed as a system with the required specifications directed not only towards the final application but also to the culture environment.

## Acknowledgements

This work was funded by the University of Utah, Department of Bioengineering and by the Wayne Brown graduate research fellowship.

## Appendix A. Figures with essential color discrimination

Certain figures in this article, particularly Figures 4 and 6–9, are difficult to interpret in black and white. The full color images can be found in the on-line version, at doi:10.1016/j.actbio.2011.06.037.

## References

[1] Taylor DA. From stem cells and cadaveric matrix to engineered organs. Curr Opin Biotechnol 2009;20:598.
[2] Zimmermann W, Eschenhagen T. Cardiac tissue engineering for replacement therapy. Heart Failure Reviews 2003;8:259.
[3] Hollister S, Wang Y, Wang G, Chen L, Li H, Yin T, et al. Scaffold engineering: a bridge to where? Biofabrication 2009.
[4] Elliott NT, Yuan F. A review of three-dimensional in vitro tissue models for drug discovery and transport studies. J Pharm Sci 2010.
[5] Gumbiner BM. Cell adhesion: the molecular basis of tissue architecture and morphogenesis. Cell 1996;84:345.
[6] Barron V, Lyons E, Stenson-Cox C, McHugh PE, Pandit A. Bioreactors for cardiovascular cell and tissue growth: a review. Ann Biomed Eng 2003;31:1017.
[7] Carrier RL, Papadaki M, Rupnick M, Schoen FJ, Bursac N, Langer R, et al. Cardiac tissue engineering: cell seeding, cultivation parameters, and tissue construct characterization. Biotechnol Bioeng 1999;64:580.
[8] Aubin H, Nichol JW, Hutson CB, Bae H, Sieminski AL, Cropek DM, Akhyari P, Khademhosseini A. Directed 3D cell alignment and elongation in microengineered hydrogels. Biomaterials; 31: 6941.
[9] Huang NF, Patel S, Thakar RG, Wu J, Hsiao BS, Chu B, et al. Myotube assembly on nanofibrous and micropatterned polymers. Nano Lett 2006;6:537.
[10] Radisic M, Park H, Shing H, Consi T, Schoen FJ, Langer R, et al. Functional assembly of engineered myocardium by electrical stimulation of cardiac myocytes cultured on scaffolds. Proceedings of the National Academy of Sciences 2004;101:18129.
[11] Tandon N, Cannizzaro C, Chao PHG, Maidhof R, Marsano A, Au HTH, et al. Electrical stimulation systems for cardiac tissue engineering. Nature Protocols 2009;4:155.
[12] Vunjak-Novakovic G, Tandon N, Godier A, Maidhof R, Marsano A, Martens T, et al. Challenges in cardiac tissue engineering. Tissue Engineering Part B: Reviews 2009:140.
[13] Eschenhagen T, Zimmermann WH. Engineering myocardial tissue. Circ Res 2005;97:1220.
[14] Pelliccia A, Spataro A, Caselli G, Maron BJ. Absence of left ventricular wall thickening in athletes engaged in intense power training. Am J Cardiol 1993;72:1048.
[15] Zimmermann WH, Cesnjevar R. Cardiac tissue engineering: implications for pediatric heart surgery. Pediatr Cardiol 2009;30:716.
[16] Baker BM, Gee AO, Metter RB, Nathan AS, Marklein RA, Burdick JA, et al. The potential to improve cell infiltration in composite fiber-aligned electrospun scaffolds by the selective removal of sacrificial fibers. Biomaterials 2008;29:2348.
[17] Radisic M, Deen W, Langer R, Vunjak-Novakovic G. Mathematical model of oxygen distribution in engineered cardiac tissue with parallel channel array perfused with culture medium containing oxygen carriers. American Journal of Physiology - Heart and Circulatory Physiology 2005;288:1278.
[18] Ott H, Matthiesen T, Goh S, Black L, Kren S, Netoff T, et al. Perfusion-decellularized matrix: using nature's platform to engineer a bioartificial heart. Nature Medicine 2008;14:213.
[19] Asakawa N, Shimizu T, Tsuda Y, Sekiya S, Sasagawa T, Yamato M, et al. Pre-vascularization of in vitro three-dimensional tissues created by cell sheet engineering. Biomaterials 2010;31:3903.
[20] Ghajar CM, Blevins KS, Hughes CC, George SC, Putnam AJ. Mesenchymal stem cells enhance angiogenesis in mechanically viable prevascularized tissues via early matrix metalloproteinase upregulation. Tissue Eng 2006;12:2875.
[21] Chen X, Aledia AS, Ghajar CM, Griffith CK, Putnam AJ, Hughes CC, et al. Prevascularization of a fibrin-based tissue construct accelerates the formation of functional anastomosis with host vasculature. Tissue Eng Part A 2009;15:1363.
[22] Kaihara S, Borenstein J, Koka R, Lalan S, Ochoa E, Ravens M, et al. Silicon micromachining to tissue engineer branched vascular channels for liver fabrication. Tissue Engineering 2000;6:105.
[23] Kim SS, Utsunomiya H, Koski JA, Wu BM, Cima MJ, Sohn J, et al. Survival and function of hepatocytes on a novel three-dimensional synthetic biodegradable polymer scaffold with an intrinsic network of channels. Annals of surgery 1998;228:8.
[24] Maidhof R, Marsano A, Lee EJ, Vunjak-Novakovic G. Perfusion seeding of channeled elastomeric scaffolds with myocytes and endothelial cells for cardiac tissue engineering. Biotechnol Prog 2010.
[25] Papenburg BJ, Liu J, Higuera GA, Barradas AM, de Boer J, van Blitterswijk CA, et al. Development and analysis of multi-layer scaffolds for tissue engineering. Biomaterials 2009;30:6228.
[26] Sakai Y, Otsuka M, Hanada S, Nishiyama Y, Konishi Y, Yamashita A. A novel poly-L-lactic acid scaffold that possesses a macroporous structure and a branching/joining three-dimensional flow channel network: its fabrication and application to perfusion culture of human hepatoma Hep G2 cells. Materials Science & Engineering C 2004;24:379.
[27] Carrier RL, Rupnick M, Langer R, Schoen FJ, Freed LE, Vunjak-Novakovic G. Perfusion improves tissue architecture of engineered cardiac muscle. Tissue Engineering 2002;8:175.
[28] Truslow JG, Price GM, Tien J. Computational design of drainage systems for vascularized scaffolds. Biomaterials 2009;30:4435.

[29] Porter B, Zauel R, Stockman H, Guldberg R, Fyhrie D. 3-D computational modeling of media flow through scaffolds in a perfusion bioreactor. Journal of Biomechanics 2005;38:543.
[30] Radisic M, Marsano A, Maidhof R, Wang Y, Vunjak-Novakovic G. Cardiac tissue engineering using perfusion bioreactor systems. Nat Protoc 2008;3:719.
[31] Fukuda S, Yasu T, Predescu DN, Schmid-Schonbein GW. Mechanisms for regulation of fluid shear stress response in circulating leukocytes. Circ Res 2000;86:E13.
[32] Kennedy JP, McCandless SP, Lasher RA, Hitchcock RW. The mechanically enhanced phase separation of sprayed polyurethane scaffolds and their effect on the alignment of fibroblasts. Biomaterials 2010;31:1126.
[33] Papenburg B, Vogelaar L, Bolhuis-Versteeg L, Lammertink R, Stamatialis D, Wessling M. One-step fabrication of porous micropatterned scaffolds to control cell behavior. Biomaterials 2007;28:1998.
[34] Kreitz MR, Webber WL, Galletti PM, Mathiowitz E. Controlled delivery of therapeutics from microporous membranes. I. Fabrication and characterization of microporous polyurethane membranes containing polymeric microspheres. Biomaterials 1997;18:597.
[35] Lasher RA, Wolchok JC, Parikh MK, Kennedy JP, Hitchcock RW. Design and characterization of a modified T-flask bioreactor for continuous monitoring of engineered tissue stiffness. Biotechnol Prog 2010;26(3):857.
[36] Li W, Tuli R, Huang X, Laquerriere P, Tuan R. Multilineage differentiation of human mesenchymal stem cells in a three-dimensional nanofibrous scaffold. Biomaterials 2005;26:5158.
[37] Okoshi T. New concept of microporous structure in small diameter vascular prostheses. Artif Organs 1995;19:27.
[38] Dar A, Shachar M, Leor J, Cohen S. Cardiac tissue engineering Optimization of cardiac cell seeding and distribution in 3D porous alginate scaffolds. Biotechnol Bioeng 2002;80:305.
[39] Wendt D, Stroebel S, Jakob M, John GT, Martin I. Uniform tissues engineered by seeding and culturing cells in 3D scaffolds under perfusion at defined oxygen tensions. Biorheology 2006;43:481.

# CHAPTER 5

# MSC COCULTURE INCREASES TISSUE STIFFNESS IN THREE-DIMENSIONAL CARDIAC FIBROBLAST MODEL

## 5.1 Abstract

Cardiac fibroblasts (CFb) are responsible for controlling passive cardiac stiffness through extracellular matrix (ECM) synthesis, degradation, and modification. Maladaptive cardiac remodeling leads to heart failure through a series of structural changes to the heart. These structural changes are effected through CFb-mediated changes in passive stiffness. Mesenchymal stem cell (MSC) therapy is promising treatment for heart failure; however, the mechanism behind efficacy of MSC treatment in animal models is poorly understood. It is hypothesized that MSC interaction with CFb can prevent or reverse maladaptive remodeling; however, the model systems that exist to test this hypothesis rely on assessment of protein expression to indirectly assess CFb-mediated changes in stiffness. Here we describe the design and validation of 3D tissue model that allows direct assessment of fibroblast mediated changes in stiffness. A perfusion culture platform is described that can sustain a uniform distribution of CFb in a porous polyurethane substrate that is 1 mm thick. After cell culture, tensile testing was used to evaluate CFb-mediated stiffness. MSC were cocultured with CFb for 10 days.

MSC coculture resulted in a significant increase in construct stiffness. Histological analysis showed MSC distributed throughout the coculture samples and an increase in type III collagen in coculture samples.

## 5.2 Introduction

Heart failure (HF) is a chronic condition that constitutes a major socio-economic burden to national healthcare systems, and a significant personal burden to families and individuals. Many common cardiovascular diseases including infarction, hypertension, valvular diseases, and congenital heart disease share HF as the end stage outcome [1]. Rates of HF are increasing in developed countries due to longer life-spans and increased likelihood of surviving of acute myocardial injury (primarily infarction) [2]. Studies of the biomechanical response of the left ventricle to myocardial infarction have identified two phenomena that lead to heart failure: (1) ventricular wall expansion in the infarct region (i.e., stretching) and (2) infarct-induced fibrosis of remote tissue. These two failure mechanisms both initiate and sustain a progressive pathologic process that ultimately results in deleterious structural and functional changes to the heart [3, 4]. These changes, termed maladaptive remodeling, are caused by abnormal myocardial stress patterns and cardiac fibroblast (CFb) mediated ECM remodeling [5]. In general, maladaptive ECM remodeling leads to undesirable passive mechanical properties that decrease cardiac output. Infarct expansion caused by insufficient passive stiffness leads to heart failure through increased wall stress on the surviving myocytes, absorption of the mechanical energy of contraction through dyskinesis of the injured region, and decreased ejection fraction [5]. Diastolic heart failure, on the other hand, generally leads to increased passive

stiffness due to fibrosis which prevents proper filling of the ventricle. Clinically, ventricular remodeling is a primary indicator of adverse outcomes such as chronic heart failure and death [6].

Cardiac fibroblasts (CFb) and acute phase inflammatory cells such as neutrophils and macrophages are jointly responsible for wound healing after MI. Due to chronic persistence of activated CFb in the heart after MI the long-term successful recapitulation of cardiac function after the initial insult is largely dependent specifically on the activity of CFb [7]. Stiffness is an important functional performance characteristic of the heart, and changes in stiffness are regulated by a precise balance of ECM degradation, synthesis and modification. Upon infarction, CFb expression and zyomgenic release of matrix metalloproteinases (MMP) has been shown to increase dramatically [8]. The activation of quiescent CFb and upregulation of MMP expression results in a local and significant degradation of collagen. Takahashi et al. demonstrated that within 3 hrs after infarction, 50% of the collagen in the infarct region was degraded in rats [9]. Increased MMP activity and resultant decreases in the collagen volume fraction in the heart have been correlated with ventricular dilatation and systolic dysfunction [10]. It has been hypothesized that this decrease in collagen volume fraction results in decreased stiffness of the ventricle, and promotes infarct expansion. In an apparent paradox, while MMP are mobilized to degrade the ECM, it has been shown that CFb simultaneously increase collagen production after infarction [11]. In addition to ECM synthesis and degradation, CFb also modify matrix stiffness through production and secretion of lysyl oxidase (LOX). LOX is responsible for cross-linking collagen, and studies have correlated increases in collagen cross-linking with increases in apparent myocardial stiffness

without necessarily a change in collagen content [12, 13]. The role of the CFb in ECM regulation makes this cell type the key determinant of passive tissue stiffness and therefore maladaptive remodeling after MI.

The complex biologic and mechanical impetus of maladaptive remodeling makes it a challenging pathology to treat. Medical device and pharmacologic treatments are used to provide palliative care and minimize cardiac remodeling, but are generally unable to reverse its course [4]. Heart transplantation remains the most effective method for treating maladaptive remodeling but is limited by a persistent shortage of donors. Recently, cardiac cell therapy has shown inconclusive yet promising results that may lead to a new treatment to prevent, and even reverse maladaptive cardiac remodeling [14, 15].

Cell therapy utilizes exogenous cells to stimulate cardiac regeneration. Recently the cardiac cell therapy paradigm has shifted largely away from replacement of myocytes, to cytoprotective and regenerative support of cardiac function [16, 17]. Utilization of mesenchymal stem cells (MSC) in animal models has been shown to be effective at preventing maladaptive postinfarction remodeling [18, 19]. Moreover, the low immunogenicity of MSC allow the use of allogenic donor cells and potential for proprietary expansion methods of MSC make this cell type a possible candidate for commercialization [20].

The mechanism behind MSC therapy is not fully understood. This lack of mechanistic understanding becomes significant in light of early human clinical trials. A meta analysis of 13 clinical trials with a total of 811 patients revealed that MSC therapy did not improve postinfarction remodeling [20]. Differences in cell therapy in human trials have been attributed to variation in processing methods of therapeutic cells, dosage,

and timing of delivery [20]. The multipotency of stem cells, while one of their strengths, also presents a significant hurdle. Different processing techniques can result in essentially different types of cells, even if they were identical to begin with. Appropriate dosing requires that both the safety and efficacy associated with various therapeutic dosages are known. The dynamic nature of maladaptive remodeling means that timing of cell therapy treatment is critical. Treatments that decrease cardiac tissue stiffness may be appropriate to prevent fibrosis, but if given too early, these treatments can cause infarct expansion or even cardiac rupture. Further mechanistic understanding will define parameters that can help move cell therapies from the trial phase to standard treatment in the clinic.

Current approaches to understanding MSC and CFb interactions have typically relied on cell culture experiments using tissue culture plastic. However, these studies are unable to directly correlate MSC treatment with CFb mediated changes in stiffness. We hypothesized that a 3D cell culture platform would allow us to investigate the effect of MSC coculture with CFb on changes in cell / scaffold composite stiffness. Here, we describe development of a simple culture platform that allows production of a 3D cell culture of CFb. This model allows us to correlate changes in bulk mechanical properties based on pharmacologic or stem cell interventions. We validated the utility of the system by culturing and evaluating 3T3 fibroblasts. We then utilized this culture platform to detect changes in CFb mediated stiffness based on cytokine supplementation and pharmacologic intervention. Moreover, this system was used to evaluate changes in stiffness with and without MSC coculture. We believe that this type of model will accelerate our ability to design treatments that more effectively prevent or reverse maladaptive remodeling of the heart.

## 5.3 Materials and Methods

### 5.3.1 Culture Platform Design

#### 5.3.1.1 Biomaterial Substrate

A nondegradable poly (ether-urethane) (PU) substrate was custom fabricated using a sprayed phase separation technique that has been described previously [21]. Briefly, a 4% PU dissolved in dimethylacetamide (Thermo Fisher Scientific, Waltham, MA) solution was sprayed onto a molded PDMS (VST-50, Factor II, Lakeside, AZ) surface with 500 μm corrugations and laminated with a total of six sheets. The resulting material was approximately 1 mm thick with enhanced hydraulic permeability due to the aligned corrugations between layers (Fig 5.1B) [22]. It was then die cut into 4 x 29 mm units for use in these experiments.

#### 5.3.1.2 Culture Chamber

The culture chamber is comprised of a pocketed polycarbonate base, a polycarbonate top plate with inlet / outlet ports, and a platinum-cure silicone gasket (durometer 30 A, VST-50, Factor II, see Fig 5.1A). The pocket depth was 1.00 ± .02 mm as measured using an automated optical measurement apparatus (Vertex, MicroVu, Windsor, CA). The tight depth tolerance is necessary to ensure that (1) the substrate is not compressed, changing the effective porosity, and (2) "nonperfusing flow" [23] does not occur either above or below the substrate in the pocket . As the gasket is compressed between the two polycarbonate plates, it expands inward to gently grip the substrate to prevent motion during perfusion. Poisson's ration (v, measured to be 0.47 for the platinum cure silicone used to mold the gasket), and the initial thickness (t) of the gasket

were used to calculate the interference (i) between the substrate and the gasket as shown in (1) below.

$$i = w_{pocket} - 2(w_{gasket} - 2(v \cdot \Delta t)) - w_{substrate} \qquad (1)$$

Gasket dimensions were designed to provide an interference of 0.50 - 0.02 mm. This interference was observed empirically to provide sufficient grip to prevent the substrate from moving during perfusion at flow rates used in these studies.

**5.3.1.3 Reservoir and tubing**

A modified 15 ml centrifuge tube serves as the media reservoir (See Fig 5.1 C). Peroxide-cured silicone tubing (ID 1/6", OD 1/8", Cole Parmer, Vernon Hills, IL) couples the opposite side of the culture chamber to a 12 ml disposable syringe (Fisher) using standard Luer Lock connectors (Qosina, Edgewood, NY). The tubing geometry was designed for oxygen exchange between the media and atmosphere. The gas flux (N) based on the permeability of the tubing ($\rho$), the atmospheric partial pressure ($p_{atm}$), maximum partial pressure of gas in solution ($p_{media}$), and the tubing geometry (ID circumference and wall thickness) was calculated as shown below.

$$N = \frac{\rho \cdot C_{ID} \cdot (p_{atm} - p_{media})}{t_{wall}} \qquad (2)$$

Based on gas flux (N), atmospheric pressure, the desired gas concentration in solution ([C]), and the fluid velocity (V), the necessary length of the tubing (L) can be determined by using equation 3:

$$[C] = P_{atm} \frac{\int_0^L N \cdot dl}{V \cdot R \cdot T} \quad (3)$$

A tubing length of 100 mm was determined to allow sufficient gas exchange for flow rates less than 1 ml/min. A computer controlled, 10-channel syringe pump was used to control the cyclic flow pattern through the cell substrate. The assembled culture chamber and centrifuge tube reservoir were sterilized with gas-plasma hydrogen peroxide; the tubing and connectors were sterilized with steam.

5.3.2 Cell Sources

**5.3.2.1 3T3 Fibroblasts**

The murine derived 3T3 fibroblast cell line (passage 5) was thawed from frozen stocks. Cells were resuspended in fibroblast culture media (used for both 3T3 and cardiac fibroblast culture): Dulbecco's modified Eagle's medium (DMEM F-12; Thermo Fisher Scientific) supplemented with 10% fetal bovine serum (FBS), 2 nM L-glutamine, 50 µl/ml streptomycin, and 50 U/ml penicillin (Invitrogen, Carlsbad, CA). Cells were centrifuged, the supernatant was removed, the cell pellet was resuspended in fresh fibroblast culture medium, and plated on a T-75 flask.

#### 5.3.2.2 Cardiac Cell Isolation

All animal procedures were performed in accordance with an approved protocol by the University of Utah Institutional Animal Use and Care Committee. Ventricular cardiac cells were harvested from one-day-old Sprague Dawley rats (Charles River, MA) using a protocol and supplies from Worthington Biochemical (Lakewood, NJ). Briefly, hearts were aseptically removed and rinsed with calcium- and magnesium-free Hank's balanced salt solution. The hearts were minced to approximately 1 $mm^3$ sections and digested in 50 μg/mL trypsin at 4°C overnight. Further digestion was performed the following day with collagenase (1500 units) in Leibovitz L-15 media. Cell suspensions were triturated, filtered, centrifuged, and plated in culture medium. Nonadherent cells were removed after 2 hrs to enrich the fibroblast population.

#### 5.3.2.3 Mesenchymal stem cells

Single donor human mesenchymal stem cells (MSC; ReachBio Seattle, WA) were passaged 2-3, and expression of CD29, CD73, CD105 CD34, and CD45 surface markers was evaluated by FACS (flow cytometry performed by manufacturer). Upon arrival, cells were thawed and grown to 90% confluence on tissue culture plastic using basal MSC medium (ReachBio), and then harvested with 0.05% trypsin-EDTA (Invitrogen, Carlsbad, CA) immediately prior to seeding.

#### 5.3.2.4 Preseeding Characterization

Confocal imaging was used to characterize the both the cardiac cell population and the MSCs prior to seeding. Adherent cardiac cells and MSCs were plated onto separate serum-treated coverslips (n=8 each), incubated for 48 hrs at 37°C, fixed with 2% paraformaldehyde overnight at room temperature, and triaged for immunostaining.

### 5.3.3 Seeding Optimization

Two different cell types were used for seeding optimization: 3T3 fibroblasts were used initially, subsequently followed by fibroblast enriched cardiac cell populations (CFb).

#### 5.3.3.1 3T3 Fibroblast Seeding

Cells were trypsinized after they reached 90% confluency and $1 \times 10^6$ cells in 11 ml of culture media were loaded into each bioreactor reservoir. Substrates were perfused at 1500 mm/min with either PBS only ($Fn^-$) or 5 ug $ml^{-1}$ of fibronectin in PBS ($Fn^+$) for 24 hrs prior to use to increase cell attachment. The preconditioning solution was removed immediately prior to seeding. Cells were cyclically perfusion seeded from the reservoir through the PU substrate at a flow velocity of either 100 mm/min (0.43 ml/min), 1000 mm/min (4.25 ml/min), or 2000 mm/min (8.50 ml/min) for 120 min (n=3 for each flow rate). The substrates were then immediately removed and fixed in 4% paraformaldehyde (PFA) overnight and triaged for density analysis. Based on initial results, all further samples underwent $Fn^+$ preconditioning as described above.

#### 5.3.3.2 Cardiac Cell Seeding

New seeding velocities were selected based on output from 3T3 seeding optimization. CFb were seeded ($0.4 \times 10^6$ cells in 11 ml culture medium) onto each construct. Three different velocities were evaluated: 1000 mm/min (4.25 ml/min), 2000 mm/min (8.50 ml/min), and 4000 mm/min (17.00 ml/min). During each experiment, samples were removed at 30 min, 60 min or 120 min (n=3 at each time point for each flow velocity), fixed in 4% PFA, and triaged for density and distribution analysis.

### 5.3.4 Treatment Induced Changes in Stiffness

#### 5.3.4.1 Ascorbic Acid Supplementation

To ensure the model was capable of detecting treatment induced *increases* in stiffness constructs were cultured in standard fibroblast culture medium (n=5) and 1 mM ascorbic acid supplemented ($aa^+$) medium (n=5). A suspension of $1\times10^6$ 3T3 fibroblasts was loaded into each reservoir with either standard or $aa^+$ media. Cells were perfusion seeded at 2000 mm/min (8.50 ml/min) for 2 hrs. Following seeding, the flow velocity was decreased to 20 mm/min (0.09 ml/min) for the remainder of the 7 day culture period to ensure sufficient gas exchange through the silicone tubing and to decrease long-term shear stress. Culture media was changed twice by pumping 90% of the media into the reservoir, removing it, and adding fresh media. Following culture, all samples were triaged for tensile testing.

### 5.3.4.2 Angiotensin Converting Enzyme (ACE) Inhibitor Supplementation

To ensure the model is capable of detecting treatment induced *decreases* in stiffness, constructs were cultured in standard fibroblast culture medium and 0.30 μg/ml $N^2$-[(1S)-1-carboxy-3-phenylpropyl]-L-lysyl-L-proline (lisinopril, TCI America, Portland, OR) supplemented medium. A suspension of $0.4\times10^6$ cardiac fibroblasts was loaded into each reservoir with either standard (n=10) or ACE inhibitor supplemented medium (n=4). Cells were perfusion seeded at 4000 mm/min (17.00 ml/min) for 2 hrs. The flow rate was subsequently decreased to 20 mm/min (0.09 ml/min) for the remainder of the 10 day culture. Medium was changed twice during the culture period as described above. Following culture, all samples were triaged for tensile testing.

5.3.5 MSC Coculture with CFb

A total of $0.3 \times 10^6$ CFb were suspended in 11 ml of fibroblast culture medium and seeded on each sample at 4,000 mm/min for 2 hrs. Flow rate following the seeding phase was 20 mm/min. Individual samples were removed and triaged for immunostaining at 3 hrs and 3 days after seeding. After 3 days, either $0.2 \times 10^6$ MSC (n=4) or $0.2 \times 10^6$ CFb (n=3) in suspension were added to the reservoir. These cells were then seeded at 4000 mm/min for 2 hrs prior to returning to 20 mm/min for the remaining 7 days of culture. Medium was exchanged twice per week on all samples. After 10 days of culture, samples were removed and triaged for tensile testing and immunostaining.

5.3.6 Tensile Testing

Tensile testing of samples was performed immediately upon removal of samples from the bioreactor. Samples were gripped at a gauge length of 19.1 mm and strained at a rate of 1 mm/min to an extension of 40% while monitoring force with a 50 N load cell (Instron, Norwood MA). Cross-sectional dimensions of each scaffold were obtained using digital calipers and were used to calculate the Young's tensile modulus of the substrate from 10% (to compensate for slight differences in pretension) to 30% extension.

5.3.7 Cell Density and Distribution Analysis

Cell nuclei were stained with 4' ,6-diamidino-2-phenylindole dihydrochloride (DAPI) for 30 min in 0.1% triton X-100 prior to imaging. An Olympus FV 1000 confocal microscope (Olympus, Center Valley, PA) with a 4X objective and motorized stage was used to obtain mosaic images of the entire substrate surface. Mosaic images were stitched using a stitching plugin for Fiji [24], and were cropped and filtered for noise using Fiji (NIH, Bethesda, MD). Cellular density and distribution were assessed using a method modified from Tang and colleagues [25]. Briefly, custom Matlab code was applied to the images to sum the number of DAPI positive pixels along the length of the substrate. The number of DAPI positive pixels was normalized to the total number of pixels and averaged along the length of the substrate. This value is reported as the relative cell density. The cell uniformity is quantified by measuring the standard deviation of DAPI positive pixels along the length of the substrate. The standard deviation of pixel intensity along the length of the substrate was normalized to the intensity to provide a relative

uniformity index, therefore, a lower uniformity index represents a more even distribution of cells throughout the substrate.

5.3.8 Immunostaining

Samples were divided into two groups for immunostaining: (1) Cardiac cell phenotyping, and (2) ECM characterization. The cardiac cell phenotyping group was trilabeled with vimentin to identify nonmyocyte cardiac cells (mostly fibroblasts), α-smooth muscle actin (SMA) to distinguish activated myofibroblasts (vimentin and SMA positive), and DAPI to identify nuclei. When cocultured with MSC, this group was quadlabeled with human nuclei antibodies (HNA) to differentiate between human MSC and rat cardiac cells. ECM was characterized through antibody staining for collagen type III and DAPI. Controls for autofluoresence and nonspecific secondary adsorption were run to control for nonspecific fluorescence.

All labeling was performed on a laboratory platform rocker at room temperature (Thermo Fisher Scientific). SMA, vimentin, and HNA antibodies were diluted in blocking solution consisting of 4% goat serum (Invitrogen) and 0.5% Triton X-100 (Fisher Scientific) diluted in PBS. Collagen type IIII is an extracellular marker, and was therefore diluted in the same solution without triton X-100. Rinsing was performed between all incubation steps and included three PBS wash outs, and three 15 min PBS rinses.

For cardiac cell phenotyping, samples were incubated for 18 hrs with mouse IgG2a anti-α-SMA (1:200 μg/mL in blocking solution; A5228; Sigma-Aldrich, St. Louis, MO), followed by 6 hrs with goat anti-mouse IgG2a-conjugated Alexa Fluor 633 (1:200;

A21136; Invitrogen), 16 hrs with mouse IgG1 anti-HNA (MSC coculture samples only; 1:400; MAB1281; Millipore-EMD, Billerica, MA) followed by 6 hrs with goat anti-mouse IgG1-conjugated Alexa Fluor 488 (1:200; A21121; Invitrogen), 16 hrs with mouse IgG1 anti-vimentin-conjugated with Cy3 (1:20; C9080; Sigma–Aldrich), and 3 hrs with DAPI (1:400; Sigma–Aldrich).

For ECM characterization, samples were incubated for 16 hrs with mouse IgG1 anti-type I collagen (1:200; C2456; Sigma-Aldrich) followed by 6 hrs with goat anti-mouse IgG1-conjugated Alexafluor 555 (1:400; A21127; Invitrogen), 16 hrs with mouse IgM anti-type III collagen (1:200; MAB2515; Millipore EMD) followed by 6 hrs with goat anti-mouse IgM-conjugated Alexa Fluor 633 (1:400; A21046; Invitrogen), and 3 hrs with DAPI (1:400; Sigma–Aldrich). All samples were stored in PBS at 4 °C.

### 5.3.9 Imaging

Imaging was performed on a confocal microscope (Zeiss LSM 5 Duo, Zeiss, Jena , Germany). For ECM characterization and images collected on glass coverslips, single image slices were obtained using a 10X objective and pinhole of 1.83 airy units. For fibroblast phenotyping on the substrate, image stacks were collected over 50 microns with a 2.5 micron step size using a 40X objective. The image stacks were z-projected using Fiji (NIH) and filtered for noise.

### 5.3.10 Statistics

Data are reported as averages ± standard deviation. Student t-tests were used evaluate significance ($\alpha$=0.05). For tensile studies, t-tests were used to evaluate differences in mean stiffness.

## 5.4 Results

### 5.4.1 Culture Platform

Pocket depth in all culture chambers was observed to fall within 1.00 ± 0.02 mm using an optical dimensioning system. The porosity of the substrate was 79.6 ± 1.5%. Dry substrate thickness was measured to be 0.99 ± 0.04 mm. The dry tensile modulus was 231.3 ± 27.6 kPa.

### 5.4.2 Cell Phenotyping

Cardiac cell populations were observed to stain positive for vimentin, and highly positive for α-SMA. Morphologic assessment confirmed that >90% of cells observed appear to be fibroblasts (Fig 5.3). Flow cytometry confirmed MSC were positive for CD29, CD73, and CD105 and negative for CD34, and CD45.

### 5.4.3 Seeding Optimization

Preliminary seeding optimization was performed first using 3T3 Fb to narrow seeding parameters and to evaluate fibronectin surface preconditioning. A significant increase in cell density was observed as the flow rate increased (Fig 5.4). Further,

fibronectin coating resulted in a higher mean cell density at each flow velocity; however, this difference was only significant at a flow rate of 2000 mm/min (Fig 5.4). Based on these results, all further samples were preconditioned with fibronectin.

A second seeding optimization was performed with CFb to corroborate the results of the 3T3 study, and to evaluate seeding duration. At 1000 mm/min, cells were qualitatively observed to be primarily distributed around the inlet and outlet (Fig 5.5D). Image analysis confirmed that at 30, 60 and 120 min seeding durations, the standard deviation of cell distribution was significantly lower for flow velocities of 4000 mm/min compared to 1000 mm/min ($p<0.05$, Fig 5.5A-C).The mean cell density when seeded at 4000 mm/min was highest after 120 min ($p<0.05$, Fig 5.6A). Moreover, after 120 min the mean cell density was higher for samples seeded at 4000 mm/min than samples seeded at 1000 or 2000 mm/min ($p<0.05$, Fig 5.6B).

### 5.4.4 Treatment Induced Changes in Stiffness

3T3 fibroblasts were seeded and cultured with standard culture medium, and ascorbic acid (aa) supplemented medium to validate the model's ability to detect treatment induced *increases* in stiffness. The tensile stress was approximately linear from 10% to 30% strain (data not shown). Acellular controls (cultured identically, without cells) had a modulus of 147.6 ± 10.2 kPa (n=5). Samples cultured with standard media had a higher average modulus of 161.7 ± 8.1 kPa ($p=0.027$, n=5). Samples cultured with aa+ medium had a significantly higher modulus than untreated constructs (178.1 ± 6.8 kPa, $p=0.004$, n=5, see Fig 5.7A).

CFb response to an angiotensin converting enzyme (ACE) inhibitor was used to evaluate the capability of the system to detect treatment-induced *decreases* in stiffness using cardiac fibroblasts. Compared with acellular substrates, the stiffness of CFb seeded constructs was significantly higher at 184.2 ± 11.6 kPa ($p=0.008$, $n=10$). The stiffness of ACE inhibitor (lisinopril) treated constructs was significantly less than untreated CFb substrates at 156.3 ± 12.55 kPa ($p=0.007$, $n=4$) but not significantly different from acellular samples (Fig 5.7B). Imaging and image analysis revealed no significant difference in cell distribution or density between standard and ACE inhibitor supplemented samples (data not shown).

### 5.4.5 Coculture of CFb and MSC

Coculture of CFb and MSC resulted in a significantly higher tensile modulus when compared to CFb only samples ($p=0.032$, Fig 5.8). The number of CFb increased over the duration of culture, with maximum number of cells observed on day 10 (Fig 5.9, A-C). In coculture samples, human MSC were observed to be distributed throughout groups of the CFb population (Fig 5.9D). Very little collagen type III was observed at t=3hrs. Type III collagen was observed to increase in abundance at t=3 days and again at t=10 days (Fig 5.10 A-C). Very low levels of type I collagen were detected at all time points (E-H). Moreover, compared to CFb only samples, coculture samples appeared to have higher levels of type III collagen (Fig 5.10 C-D).

## 5.5 Discussion

The complexity of fibroblast-mediated changes in passive stiffness makes indirect assessment of stiffness using histological or biochemical techniques extremely challenging. Here, we developed and validated a 3D cell culture model for direct evaluation of CFb-mediated changes in stiffness in response to pharmacologic or cellular treatment.

Here, flow is presented in terms of fluid velocity, mm/min. Fluid flow has been shown to affect fibroblast expression of MMP, TIMP, and migration [26]. Fibroblast mechanotransduction of fluid flow occurs as a surface phenomenon where local shear stresses interact with ECM and integrins resulting in intracellular signaling through the mitogen activated protein kinase pathway [27]. Since, shear stress estimations of composite cellularized biomaterials are dependent on local fluid velocities rather than bulk flow [27, 28]. We believe that for this perfusion system, reporting fluid velocity is more pertinent than volumetric flow.

We chose fluid velocities for the seeding phase and culture phase based on initial work with both 3T3 Fb and CFb. Corresponding data regarding appropriate flow for mixed cardiac cell populations vary considerably. Madihof et al. tested cyclic fluid velocities ranging from 6 - 60 mm/min using a population of cardiac cells that had been enriched for myocytes [29]. They determined that the fastest velocity tested (60 mm/min) resulted in the highest seeding efficiency. Moreover, they determined that seeding efficiency was slightly higher after 2 hrs of seeding compared to one. Our results agree with the seeding time of 2 hrs being slightly better than 1 hr. However, the flow rates used during seeding in this work are many times faster than previous studies. Fibroblasts

attach to surface in 10-30 min, while myocytes can require hours to attach to synthetic polymer surfaces [30]. In these studies, perfusion rates below 2000 mm/min resulted in inhomogeneous attachment of CFb throughout the substrate (Fig 5.4A-C). At a velocity of 1000 mm/min, most of the CFb were located immediately below the inlet (Fig 5.4D). It appears that CFb cell populations may require significantly higher seeding velocities than myocyte-containing cardiac cell populations likely attributable to the difference in rate of attachment of the two cell types.

The qualitative appearance of cells in the polyurethane substrate was different from cells cultured on glass coverslips. It is well known that fibroblast morphology and phenotype can be altered by differences in 2D versus 3D substrates, stiffness of substrates and substrate chemistry [31-33]. In our experiments, the polyurethane material may be preferentially selecting for certain cardiac cell populations although this was not specifically examined. The polyurethane material used in these experiments has been extensively characterized in its ability to support primary Fb under different culture conditions [34-37]. Despite the qualitative differences in cell morphology between the glass coverslips and the polyurethane scaffold, we believe it is unlikely that the culture conditions are preferentially enriching a nonfibroblast population of cardiac cells. This is because primary fibroblasts are known to proliferate on these substrates, the starting population contains a high percentage of fibroblasts and our qualitative observations over the time course of the experiments provides visual evidence that the fibroblasts have proliferated and attached to the polyurethane substrate.

Murine 3T3 fibroblasts were used to evaluate the ability of the culture platform to detect treatment-induced increases in stiffness. Previous work has shown that ascorbic

acid (aa) enables the assembly of ECM proteins [38] and increases stiffness [36]. ACE inhibitor treatment, on the other hand, was shown to decrease the stiffness of CFb populated constructs after 10 days. This corresponds to the well established role of ACE inhibitors in preventing fibroblast mediated fibrosis [39]. Our validation demonstrates that the culture platform is capable of observing aa induced increases in stiffness, and ACE inhibitor induced decreases in stiffness compared to untreated cellular groups.

MSC and CFb coculture resulted in a significant increase in stiffness when compared to cell number controlled CFb only samples (Fig 5.8). HNA staining demonstrated that human MSC were present among CFb after 10 days of coculture (Fig 5.9). We believe that this increase in stiffness is in part due to an increase in type III collagen in coculture samples compared to CFb only samples (Fig 5.10 C-D). It is not evident from the data whether the MSC contribute to the accumulation of type III collagen directly through collagen synthesis, or whether they contribute indirectly through paracrine or juxtacrine influence of CFb behavior. One study shows that MSC cultured on substrates increased type III collagen production and stiffness in response to mechanical stimulation [40]. It is likely that shear stress in the model could contribute to mechanical stimulation of MSC, which would support the hypothesis regarding the direct role of MSC in collagen synthesis. This hypothesis is further supported by studies that have shown *in vitro* paracrine signaling of MSC downregulates CFb expression of type III collagen [41]. Future studies evaluating the species origin of the type III collagen could help further elucidate the direct and indirect contributions of MSC to the observed changes in stiffness. The lack of type I collagen type is surprising, and may be due to collagen passing into the culture media before it is able to assemble as has been observed

in 2D cell culture [42]. The culture medium did not have ascorbic acid, which is necessary for assembly of mature collagen fibers which may help to explain why little type I collagen was observed [43].

This model is limited in its ability to detect changes in stiffness by the use of a nondegradable substrate. The observed changes in bulk stiffness are due to a complex interaction of interstitial fluid flow, cytoplasmic rearrangement, and bending, flexing, and elongation of intra and extracellular filaments. Modulus of collagen molecule ranges from 2.9 to 9.0 GPa as measured by X-ray diffraction technique [44]. Collagen fibers are considerably softer, measured at 0.7-3.7 MPa using tensile stress-strain analysis [45]. In the myocardium, it appears that perimysial collagen fibers are not elongated during strain, but rather undergo helical bending and uncrimping that accounts for the majority of the measured stiffness in the myocardium [46]. In a mathematical model these forces have been calculated to be on the order of 135-160 MPa [46]. In addition to collagen, several groups have demonstrated that cytoskeletal filaments of fibroblasts themselves can exert tractional forces in the range of tens of nanonewtons per focal adhesion that resist extension and potentially contribute to bulk stiffness [47, 48].

The general rule of mixtures states that the overall modulus can be approximated by summing the product of the modulus and volume fraction of each constituent. This approximation provides an upper bound for stiffness by modeling the individual elements in series. The general rule of mixtures assumes that coupling of all elements is ideal and that no interfacial failure occurs. The inverse rule for mixtures, on the other hand, assumes no interfacial coupling between the different material constituents, and provides a lower bound for the overall stiffness by modeling a parallel alignment of the various

elements comprising the material. In reality, the modulus of the cellularized substrate falls somewhere between the upper bound determined by the rule of mixtures, and the lower bound determined by the inverse rule. The degree of coupling of cells and ECM to the substrate is the primary determinant of whether the material stiffness approaches the upper or lower bound for tensile stiffness.

Cells serve as the primary binding element that couples matrix components and internal cellular skeletal filaments to the substrate. Focal adhesion complexes attach cells to proteins adsorbed to the surface of the substrate as well as to surrounding matrix elements. The adhesion of 3T3 fibroblasts to fibronectin coated silicon has been measured to be approximately 450 dynes/cm$^2$ (45 Pa) [49]. Uncoupling of the cellular material from the substrate will obscure cellular contributions to stiffness. Indeed, this model is only capable of assessing *bulk* changes in stiffness; local uncoupled contributions to stiffness are overshadowed by the modulus of the substrate. Moreover, measured against a constant, and relatively large stiffness of the substrate itself, the ability of this system is limited in its ability to detect cell-mediated changes in stiffness that are too soft to be detected over the baseline stiffness of the substrate (~150 kPa). Despite these limitations, the ability to measure bulk stiffness gives insight a tissue-level functional property that, *in vivo,* directly influences the performance of the heart.

Another limitation is the use of vimentin to identify fibroblasts from the cardiac cell population. While myocytes do not stain positive for vimentin, this marker also identifies endothelial and neuronal cells found in the heart. However, since >90% of nonmyocytes in the heart are fibroblasts, until more specific methods for fibroblast identification are established, vimentin staining coupled with cyto-morphologic

evaluation is generally accepted as a method to identify fibroblasts in mixed cardiac cell populations [50] .

Another limitation to this study is the use of human MSC with rat CFb. There is a high degree of conserved function between human and rat CFb; however, there are differences including expression of MMP-1, and integrin expression in response to angiotensin II. In this study, the species difference allowed for differentiation of human and rat cells through antibody labeling. For future studies using human CFb, alternative methods for differentiating the cells will be required. In addition, we believe that future application of the model described here can be used to rapidly identify MSC preconditioning or modification that will lead to positive outcomes *in vivo*.

## 5.6 Acknowledgements

The authors would like to acknowledge Chris Hunter and Dr. Alonso Moreno for their generous donation of cardiac fibroblasts for this research. This research was supported by funding from the Department of Bioengineering at the University of Utah.

## 5.7 References

[1] Cutler MJ, Rosenbaum DS, Dunlap ME. Structural and electrical remodeling as therapeutic targets in heart failure. J Electrocardiol. 2007;40:S1-7.

[2] Leonard BL, Smaill BH, Legrice IJ. Structural remodeling and mechanical function in heart failure. Microsc Microanal. 2012;18:50-67.

[3] Connelly CM, Vogel WM, Wiegner AW, Osmers EL, Bing OH, Kloner RA, et al. Effects of reperfusion after coronary artery occlusion on post-infarction scar tissue. Circ Res. 1985;57:562-77.

[4] Gorman RC, Jackson BM, Burdick JA, Gorman JH. Infarct restraint to limit adverse ventricular remodeling. J Cardiovasc Transl Res. 2011;4:73-81.

[5] Pfeffer MA, Braunwald E. Ventricular remodeling after myocardial infarction. Experimental observations and clinical implications. Circulation. 1990;81:1161-72.

[6] Udelson JE, Konstam MA. Relation between left ventricular remodeling and clinical outcomes in heart failure patients with left ventricular systolic dysfunction. J Card Fail. 2002;8:S465-71.

[7] Sun Y, Weber KT. Infarct scar: a dynamic tissue. Cardiovasc Res. 2000;46:250-6.

[8] Wilson EM, Moainie SL, Baskin JM, Lowry AS, Deschamps AM, Mukherjee R, et al. Region- and type-specific induction of matrix metalloproteinases in post-myocardial infarction remodeling. Circulation. 2003;107:2857-63.

[9] Takahashi S, Barry AC, Factor SM. Collagen degradation in ischaemic rat hearts. Biochem J. 1990;265:233-41.

[10] Janicki JS, Brower GL, Henegar JR, Wang L. Ventricular remodeling in heart failure: the role of myocardial collagen. Adv Exp Med Biol. 1995;382:239-45.

[11] Cleutjens JP, Verluyten MJ, Smiths JF, Daemen MJ. Collagen remodeling after myocardial infarction in the rat heart. Am J Pathol. 1995;147:325-38.

[12] Norton GR, Tsotetsi J, Trifunovic B, Hartford C, Candy GP, Woodiwiss AJ. Myocardial stiffness is attributed to alterations in cross-linked collagen rather than total collagen or phenotypes in spontaneously hypertensive rats. Circulation. 1997;96:1991-8.

[13] Woodiwiss AJ, Tsotetsi OJ, Sprott S, Lancaster EJ, Mela T, Chung ES, et al. Reduction in myocardial collagen cross-linking parallels left ventricular dilatation in rat models of systolic chamber dysfunction. Circulation. 2001;103:155-60.

[14] Segers VF, Lee RT. Stem-cell therapy for cardiac disease. Nature. 2008;451:937-42.

[15] Passier R, van Laake LW, Mummery CL. Stem-cell-based therapy and lessons from the heart. Nature. 2008;453:322-9.

[16] Menasche P. Stem cell therapy for chronic heart failure: lessons from a 15-year experience. C R Biol. 2011;334:489-96.

[17] Forrester JS, White AJ, Matsushita S, Chakravarty T, Makkar RR. New paradigms of myocardial regeneration post-infarction: tissue preservation, cell environment, and pluripotent cell sources. JACC Cardiovasc Interv. 2009;2:1-8.

[18] Lian WS, Cheng WT, Cheng CC, Hsiao FS, Chen JJ, Cheng CF, et al. In vivo therapy of myocardial infarction with mesenchymal stem cells modified with

prostaglandin I synthase gene improves cardiac performance in mice. Life Sci. 2011;88:455-64.

[19] Mias C, Lairez O, Trouche E, Roncalli J, Calise D, Seguelas MH, et al. Mesenchymal stem cells promote matrix metalloproteinase secretion by cardiac fibroblasts and reduce cardiac ventricular fibrosis after myocardial infarction. Stem Cells. 2009;27:2734-43.

[20] Menasche P. Cardiac cell therapy: lessons from clinical trials. J Mol Cell Cardiol. 2010;50:258-65.

[21] Kennedy JP, McCandless SP, Lasher RA, Hitchcock RW. The mechanically enhanced phase separation of sprayed polyurethane scaffolds and their effect on the alignment of fibroblasts. Biomaterials. 2010;31:1126-32.

[22] Kennedy JP, McCandless SP, Rauf A, Williams LM, Hillam J, Hitchcock RW. Engineered channels enhance cellular density in perfused scaffolds. Acta Biomater. 2011;7:3896-904.

[23] Bancroft GN, Sikavitsas VI, Mikos AG. Design of a flow perfusion bioreactor system for bone tissue-engineering applications. Tissue Eng. 2003;9:549-54.

[24] Preibisch S, Saalfeld S, Tomancak P. Globally optimal stitching of tiled 3D microscopic image acquisitions. Bioinformatics. 2009;25:1463-5.

[25] Thevenot P, Nair A, Dey J, Yang J, Tang L. Method to Analyze Three-Dimensional Cell Distribution and Infiltration in Degradable Scaffolds. Tissue Engineering Part C Methods. 2008;14:319-31.

[26] Shi ZD, Ji XY, Qazi H, Tarbell JM. Interstitial flow promotes vascular fibroblast, myofibroblast, and smooth muscle cell motility in 3-D collagen I via upregulation of MMP-1. Am J Physiol Heart Circ Physiol. 2009;297:H1225-34.

[27] Shi ZD, Tarbell JM. Fluid flow mechanotransduction in vascular smooth muscle cells and fibroblasts. Ann Biomed Eng. 2011;39:1608-19.

[28] Radisic M, Deen W, Langer R, Vunjak-Novakovic G. Mathematical model of oxygen distribution in engineered cardiac tissue with parallel channel array perfused with culture medium containing oxygen carriers. American Journal of Physiology-Heart and Circulatory Physiology. 2005;288:1278-89.

[29] Maidhof R, Marsano A, Lee EJ, Vunjak-Novakovic G. Perfusion seeding of channeled elastomeric scaffolds with myocytes and endothelial cells for cardiac tissue engineering. Biotechnol Prog. 2010;26:565-72.

[30] Horio T, Nishikimi T, Yoshihara F, Matsuo H, Takishita S, Kangawa K. Effects of adrenomedullin on cultured rat cardiac myocytes and fibroblasts. European Journal of Pharmacology. 1999;382:1-9.

[31] Cukierman E, Pankov R, Stevens DR, Yamada KM. Taking cell-matrix adhesions to the third dimension. Science. 2001;294:1708-12.

[32] Galie PA, Westfall MV, Stegemann JP. Reduced serum content and increased matrix stiffness promote the cardiac myofibroblast transition in 3D collagen matrices. Cardiovasc Pathol. 2011;20:325-33.

[33] Woods A, Couchman JR, Johansson S, Hook M. Adhesion and cytoskeletal organisation of fibroblasts in response to fibronectin fragments. The EMBO Journal. 1986;5:665-70.

[34] Lasher RA, Wolchok JC, Parikh MK, Kennedy JP, Hitchcock RW. Design and characterization of a modified T-flask bioreactor for continuous monitoring of engineered tissue stiffness. Biotechnol Prog. 2010;26:857-64.

[35] Wolchok JC, Brokopp C, Underwood CJ, Tresco PA. The effect of bioreactor induced vibrational stimulation on extracellular matrix production from human derived fibroblasts. Biomaterials. 2009;30:327-35.

[36] Webb K, Hitchcock RW, Smeal RM, Li W, Gray SD, Tresco PA. Cyclic strain increases fibroblast proliferation, matrix accumulation, and elastic modulus of fibroblast-seeded polyurethane constructs. J Biomech. 2006;39:1136-44.

[37] Webb K, Li W, Hitchcock RW, Smeal RM, Gray SD, Tresco PA. Comparison of human fibroblast ECM-related gene expression on elastic three-dimensional substrates relative to two-dimensional films of the same material. Biomaterials. 2003;24:4681-90.

[38] Peterkofsky B. The effect of ascorbic acid on collagen polypeptide synthesis and proline hydroxylation during the growth of cultured fibroblasts. Arch Biochem Biophys. 1972;152:318-28.

[39] Lijnen PJ, Petrov VV, Fagard RH. Collagen production in cardiac fibroblasts during inhibition of angiotensin-converting enzyme and aminopeptidases. J Hypertens. 2004;22:209-16.

[40] Juncosa-Melvin N, Matlin KS, Holdcraft RW, Nirmalanandhan VS, Butler DL. Mechanical stimulation increases collagen type I and collagen type III gene expression of stem cell-collagen sponge constructs for patellar tendon repair. Tissue Eng. 2007;13:1219-26.

[41] Ohnishi S, Sumiyoshi H, Kitamura S, Nagaya N. Mesenchymal stem cells attenuate cardiac fibroblast proliferation and collagen synthesis through paracrine actions. FEBS Letters. 2007;581:3961-6.

[42] Nusgens B, Merrill C, Lapiere C, Bell E. Collagen biosynthesis by cells in a tissue equivalent matrix in vitro. Collagen and Related Research. 1984;4:351-63.

[43] Grinnell F, Fukamizu H, Pawelek P, Nakagawa S. Collagen processing, crosslinking, and fibril bundle assembly in matrix produced by fibroblasts in long-term cultures supplemented with ascorbic acid. Exp Cell Res. 1989;181:483-91.

[44] Sasaki N, Odajima S. Stress-strain curve and Young's modulus of a collagen molecule as determined by the X-ray diffraction technique. J Biomech. 1996;29:655-8.

[45] Christiansen DL, Huang EK, Silver FH. Assembly of type I collagen: fusion of fibril subunits and the influence of fibril diameter on mechanical properties. Matrix Biology : Journal of the International Society for Matrix Biology. 2000;19:409-20.

[46] MacKenna DA, Vaplon SM, McCulloch AD. Microstructural model of perimysial collagen fibers for resting myocardial mechanics during ventricular filling. Am J Physiol. 1997;273:H1576-86.

[47] Grinnell F. Fibroblasts, myofibroblasts, and wound contraction. J Cell Biol. 1994;124:401-4.

[48] Wang JH, Lin JS. Cell traction force and measurement methods. Biomechanics and Modeling in Mechanobiology. 2007;6:361-71.

[49] Gallant ND, Michael KE, Garcia AJ. Cell adhesion strengthening: contributions of adhesive area, integrin binding, and focal adhesion assembly. Mol Biol Cell. 2005;16:4329-40.

[50] Camelliti P, Borg TK, Kohl P. Structural and functional characterisation of cardiac fibroblasts. Cardiovasc Res. 2005;65:40-51.

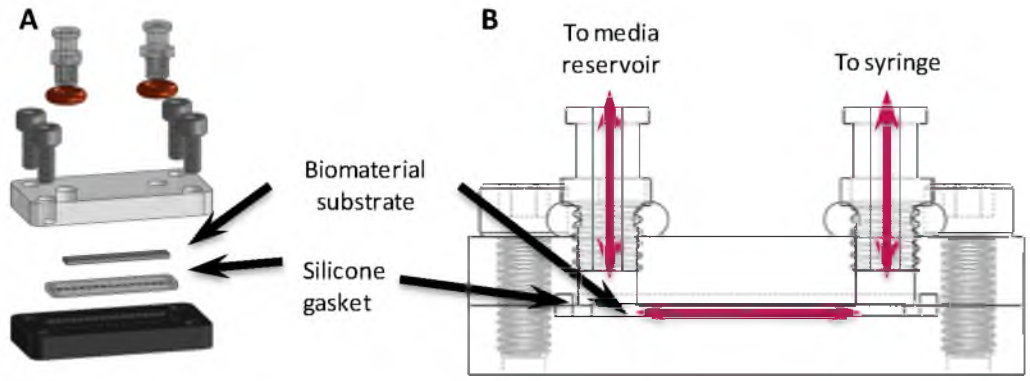


Fig 5.1. Culture platform schematic. (A) An exploded view of the culture chamber. This view describes the assembly of each culture cassette including the substrate and silicone gasket that ensure perfusing media flow. (B) Cross section of culture cassette with arrows to demonstrate the flow path.

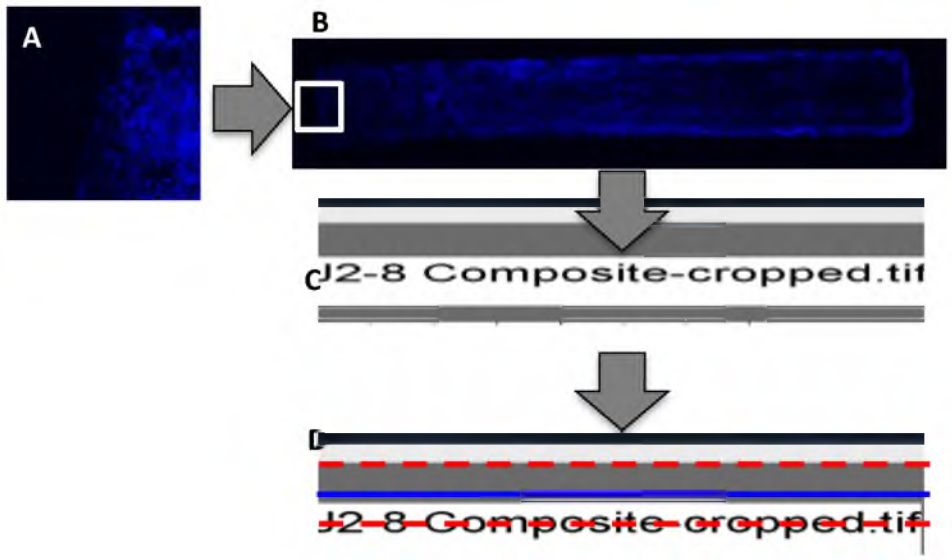


Fig 5.2. Image processing method. (A) Individual DAPI images were collected and stitched together to form mosaic images (B). (C) Column summing of DAPI positive pixels along the length of the tissue was used to evaluate cell distribution along the length of substrate. (D) Moving average (solid-black), overall mean (solid-blue) and overall standard deviation (dashed-red) were calculated to quantify cell density and uniformity.

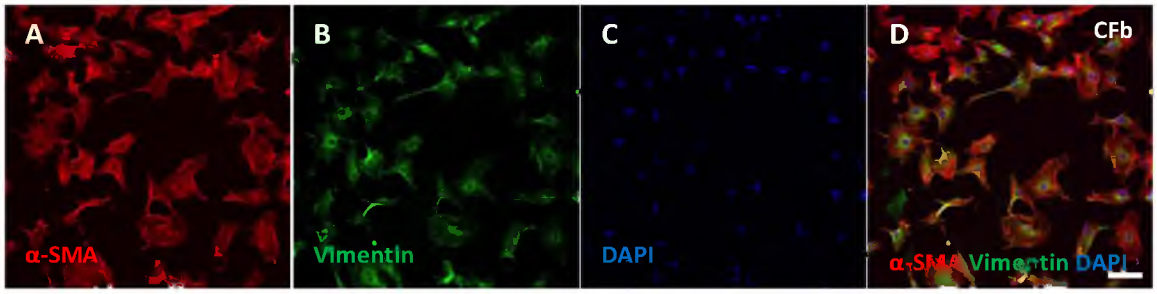


Fig 5.3. Initial phenotyping of cardiac cell population. CFb were identified morphologically from vimentin positive cells. Cardiac cells at t=0 highly expressed α-SMA (A), vimentin (B), and DAPI (C, composite image, D). Scale bar is 100 μm.

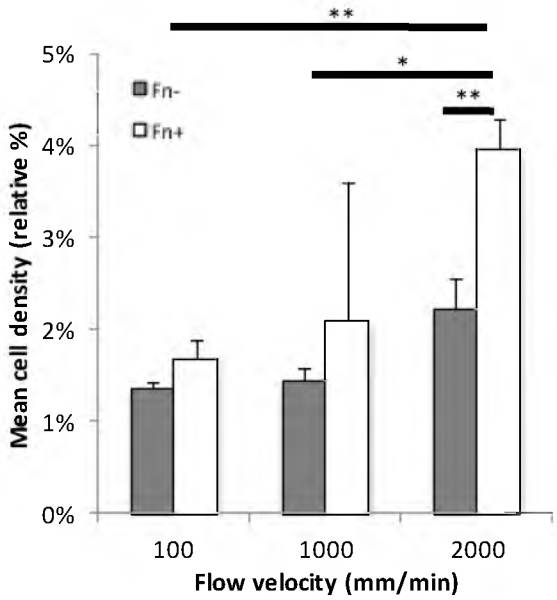


Fig 5.4. 3T3 Fb density with different seeding velocities and substrate coatings. Cell density increased after 2 hrs of seeding using 3T3 Fb with fibronectin preconditioning (Fn+) compared to without (Fn-). Further, density of 3T3 cells increased as perfusion velocity increased from 100mm/min to 2000 mm/min. *$p<0.05$ ** $p<0.01$. n=3 for each group.

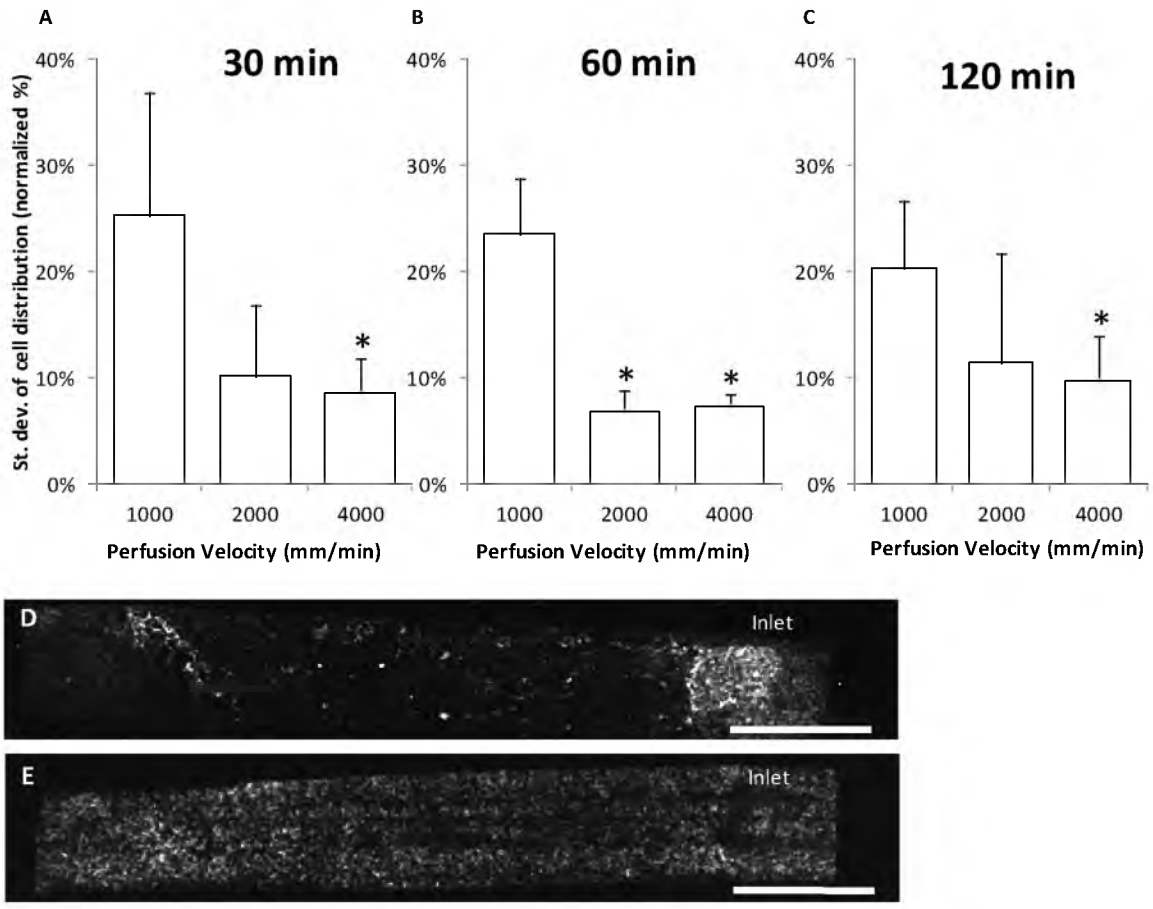


Fig 5.5. CFb uniformity with different seeding velocities and duration. CFb were seeded onto substrates at 1000 mm/min (4.25 ml/min), 2000 mm/min (8.50 ml/min), and 4000 mm/min (17.00 ml/min). The standard deviation of cell distribution was assessed for each flow velocity at 30 min (A), 60 min (B), and 120 min (C, n=3 for each velocity and duration). *$p<0.05$ when compared to 1000 mm/min velocity. (D) Representative image of a substrate after 2 hrs of seeding at 1000 mm/min with cardiac fibroblasts. Distribution is highly nonhomogeneous with more cells located in the inlet region. (E) Substrate after 2 hrs of seeding at 4000 mm/min with cardiac fibroblasts. Scale bar is 5 mm.

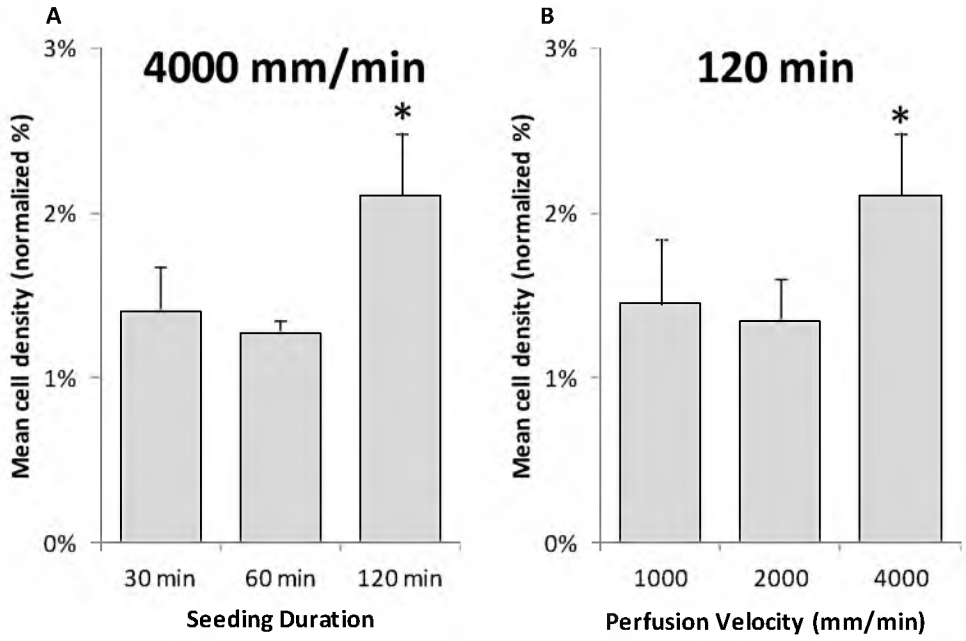


Fig 5.6. Mean CFb density with different seeding velocities and duration. (A) Mean cell density of cardiac fibroblasts seeded at 4000 mm/min for 30, 60 and 120 min (n=3 each). *$p<0.05$ from 30 min and 60 min seeding durations. (B) Mean cell density of cardiac fibroblasts seeded at 1000, 2000, and 4000 mm/min for 120 min (n=3 each). *$p<0.05$ from 1000 mm/min and 2000 mm/min seeding durations.

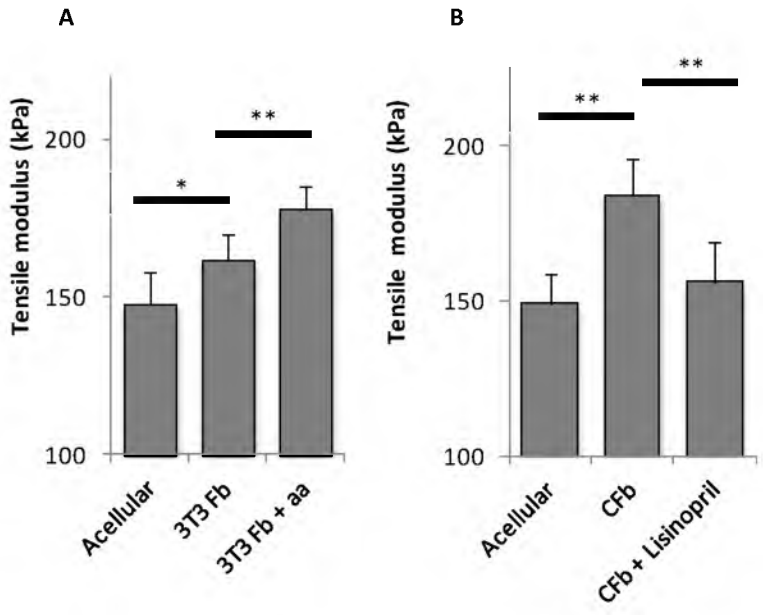


Fig 5.7. Treatment induced changes in stiffness. (A) Tensile modulus of acellular, 3T3 Fb in standard culture medium, and 3T3 Fb in aa supplemented medium after perfusion culture (n=5 each). (B) Tensile modulus of acellular, Cardiac Fb in standard culture medium, and cardiac Fb in ACE inhibitor (lisinopril) supplemented medium after perfusion culture (n=5 acellular, n=10 CFb, n=4 CFb+lisinopril). *$p<0.05$ **$p<0.01$

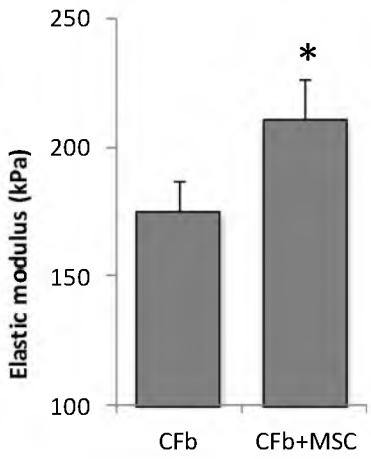


Fig 5.8. Tensile modulus of MSC coculture constructs. Elastic modulus of CFb cocultured with MSC was significantly higher than cell number controlled constructs cultured with CFb only (n=3 CFb, n=4 CFb+MSC). *$p<0.05$ from CFb.

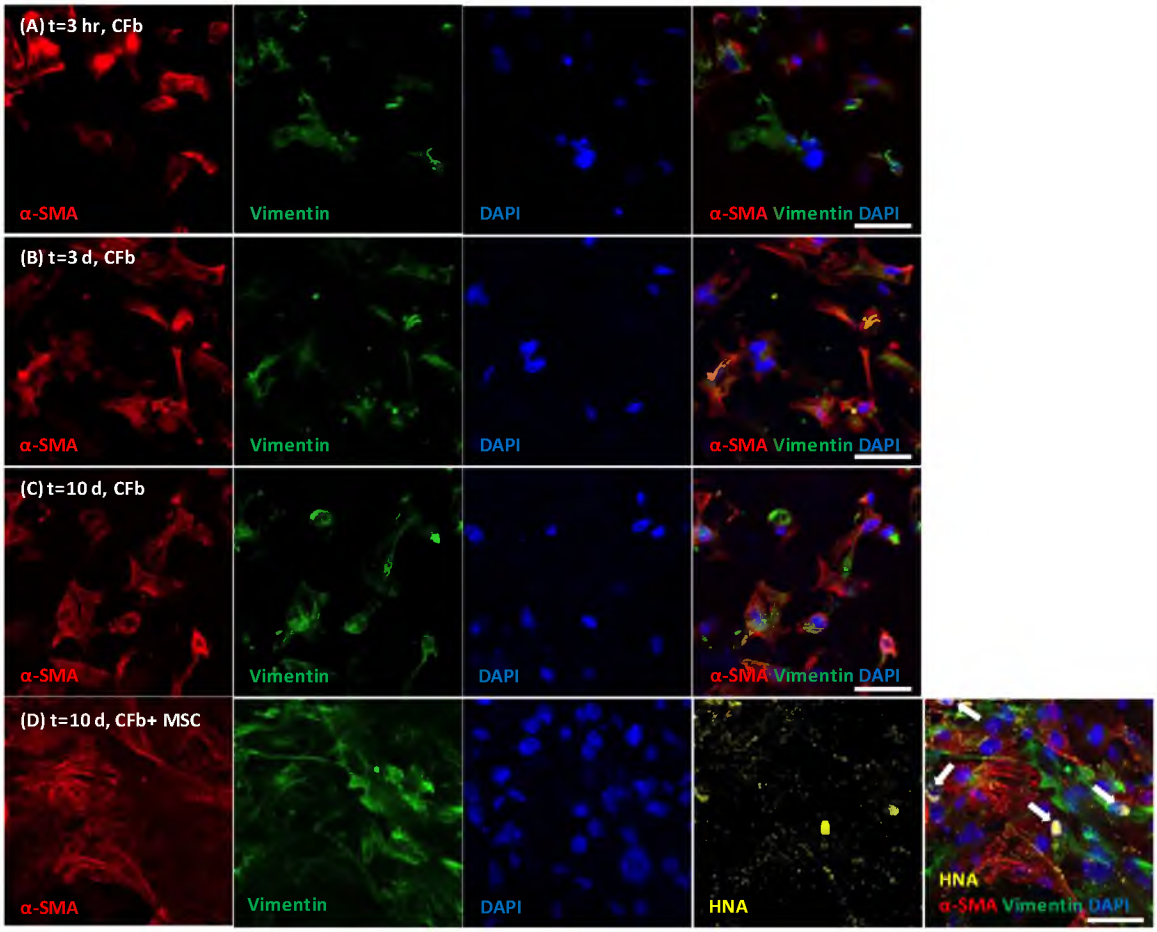


Fig 5.9. Cell characterization during culture. Samples were removed and imaged after 3hrs (A), 3 days (B) and 10 days (C-D). CFb only samples (A-C) were labeled for α-SMA, vimentin, and cell nuclei. CFb-MSC coculture samples were labeled additionally for human nuclei (HNA) to identify MSC (see arrows in D). Scale bars are 50 μm

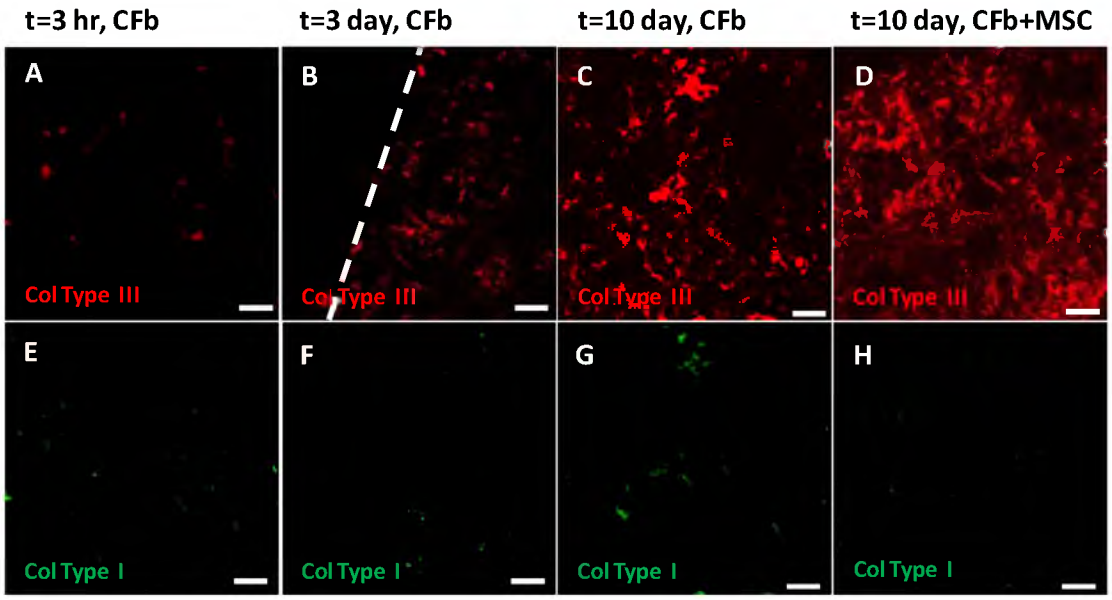


Fig 5.10. Collagen labeling during culture. Type III collagen levels appeared to increase over time (A-C). MSC coculture increased levels of type III collagen compared to CFb only samples (C-D). Dotted white line marks the edge of the substrate in (B). Scale bars are 100 μm.

# CHAPTER 6

# CONCLUSION AND FUTURE DIRECTIONS

## 6.1 Summary and conclusions

In Chapter 3, methods for fabricating a biocompatible substrate with engineering control over stiffness, anisotropy, and porosity were described. This process was automated using a three axis computer controlled spray system. The material used to fabricate the substrate is a nondegradable poly (ether-urethane). Previous work describes methods for processing polyurethanes into porous cell scaffold materials [1] and the use of a sprayed phase separation technique [2, 3]. This work expanded upon current approaches to sprayed phase separation in two ways: (1) the effect of nonsolvent ethanol concentration on stiffness, porosity, and microarchitecture was evaluated, and (2) a postspray elongation technique was developed to introduce anisotropy. Prior to this work, a noteable dipped phase separation technique had been developed by Papenburg et al. [4]. This group evaluated several different alcohol classes and concentrations ranging from 0% to 12.5%. Their work inspired the use of alcohol in the nonsolvent in this dissertation. Based on their results we utilized ethanol in the nonsolvent and expanded the nonsolvent concentration from 0% to 85%.

Moreover, in this work we demonstrated that through postspray elongation this material can be engineered to serve as a static 3D architectural map for fibroblast orientation. One approach to recapitulate cardiac structure and function is to match substrate anisotropy to native cardiac structure. In the first phase of this work, variation in postspray elongation was shown to be correlated with the anisotropy ratio based on mechanical testing. Further, experiments with 3T3 fibroblasts demonstrated that the aligned microarchitecture of the substrate influenced fibroblast alignment within the material. While this technique was not employed in later phases of this work, this is an important technique that broadens the capability of the methods developed in Chapter 3. The control over mechanical properties through postspray elongation and nonsolvent composition established in this phase of the work was critical for later work where this material was shown to have sufficient elasticity to allow detection of cell-mediated changes in stiffness after 10 days of cell culture.

One practical outcome of this phase of research is a method to robustly fabricate porous substrates with high fidelity and control over porosity and mechanical properties. The substrates used in Chapters 4 and 5 relied on the methods developed in this phase of the work. In 2012, 8 batches of substrates (60 substrates from each batch) were fabricated. The porosity and stiffness were inspected from each batch before the substrates were released for use in experiments. Porosity varied by only 2.0% in all batches (over 450 substrates). The robust process used to fabricate the cell scaffold material described in Chapter 3 is a necessary feature of any scaffold that aspires to span the gap between 2D cell culture and animal models [5].

In Chapter 4, a lamination procedure is described that builds channel-like features for anisotropic permeability into composite substrates with variable thicknesses. Prior work described dipped phase separation micromolding techniques [4]. This technique resulted in patterned surfaces of porous materials. The research described here expanded on existing techniques by laminating multiple micropatterned sheets to form enclosed, three-dimensional features within the substrate. The structural features of these substrates were evaluated for both qualitative architecture, and performance characteristics. A media perfusion system was built and the effect of media perfusion on both channeled and nonchanneled substrates was evaluated. Previous studies with cell culture have highlighted the need for convective media transport to supplement diffusion to maintain viability of 3D tissues [6-9]. The unintended consequence of perfusion in cell culture is cellular damage and phenotypic shift due to shear stress of the moving fluid. Both cardiac cells (primarily myocytes, however, Fb are responsive as well) and MSC are highly susceptible to shear stress-induced damage [10-12]. Moreover, depending on substrate microarchitecture, media flow can "wash" cells off the substrate surface resulting in decreasing cell density over time [13]. Approaches to shielding cells from unnecessary shear stress through scaffold architecture hold promise for development of the next generation of 3D cell culture platforms [14]. By designing a substrate with anisotropic hydraulic permeability, we demonstrated that we could significantly increase cell density of MSC after perfusion culture. This result helps establish the use of aligned flow channels to favorably modify media convection through the substrate. Since this work was originally performed, numerous approaches to designing channels into 3D substrates have been proposed [15-18].

The work contained in Chapter 5 describes modifications to the perfusion culture platform to yield individual culture cassettes. These perfusion cassettes are considerably easier to fabricate and use compared to the initial perfusion system descroibed in Chapter 4. Validation of the new culture platform was performed using murine 3T3 fibroblasts. Once functional perfusion parameters were determined, CFb were seeded and cultured on the substrate. An ACE inhibitor and TGF-β were used to validate that treatment induced changes in stiffness could be detected using this system. Following these experiments, MSC were cocultured with CFb for 10 days. Significantly, we observed that despite increased cell density, MSC coculture with cardiac fibroblasts did not increase stiffness when compared to controls. The major conclusion from this phase of work is that unmodified MSC should not be used to influence cardiac fibroblast mediated stiffness. Future utilization of this model will allow evaluation of modified MSC in treating heart failure. While MSC therapy is a promising new treatment for heart failure, it is still unclear what mechanism is responsible for restoring cardiac function in animal models [19]. It has been hypothesized that MSC treatment may have an influence on fibroblast-mediated stiffness, but prior to this work direct measurement had not been attempted. Previous work has had conflicting results regarding the effects of MSC coculture on cardiac stiffness; one study implies that MSC cause increased degradation of ECM through increased MMP production [20], while another suggests that MSC coculture suppresses MMP production and therefore decreases ECM degradation [21]. Many groups have focused on MSC preconditioning or genetic modification [22-24]. Further, clinical MSC isolation kits vary significantly and potentially "modify" MSC enough to cause divergent clinical outcomes [25]. The work presented here supports a growing

body of evidence that unmodified MSC may not have significant effects on cardiac remodeling. Despite this negative finding, the platform developed to evaluate MSC-CFb coculture still holds considerable promise to evaluate modified MSC interactions with CFb. Whatever treatment is developed for maladaptive cardiac remodeling, the platform developed here can provide crucial insight into treatment-induced changed in stiffness. Further, common molecular biology techniques can be employed to gain insight to expression of proteins that are related to stiffness. Application of this insight may directly influence clinical implementation of cardiac cell therapy treatments.

## 6.2 Applications and Future Directions

### 6.2.1 Mesenchymal Stem Cell Modification

The cell culture model described here has application in preclinical evaluation of stem cell interaction with cardiac fibroblasts in 3D. In practice, the use of bone marrow derived stem cells requires specific preparation and isolation processes that have yet to be standardized [19]. This lack of standardization contributes to one limitation of this research – the status of the MSC used in this experiment is related to their history prior to use. It is difficult to directly correlate results from this study to other studies because of differences in the treatment of MSC prior to their use. Divergence of the centrifugation methods used to separate MSC and passage number has been linked to variation of clinical outcomes [25]. Beyond simple processing modifications, some groups have demonstrated that genetic modification of MSC can have enhanced therapeutic effects in animal models. Lian et al. demonstrated that prostaglandin I synthase transformed MSC had higher wall thickness and lower percentages of fibrotic area than unmodified MSC in

mice [22]. Gnecchi and colleagues showed that modification of MSC with the AKT1 survival gene resulted in production of paracrine signals that significantly decreased cardiomyocyte apoptosis when compared to unmodified MSC [24]. Utilization of the in vitro model described herein to evaluate treatment induced changes in stiffness effected through modified MSC phenotypes will allow optimization of the cell processing and preparation techniques that would otherwise be prohibitively difficult and expensive to implement in clinical studies.

### 6.2.2 Dosing and Cell Retention Studies

Another clinical variable associated with implementation of stem cell therapy is dosage [19]. Dosage is dependent on two factors: (1) cell retention, and (2) cell activity [26]. In most cases, the majority of therapeutic cells delivered to the heart are not retained in the desired area after 24 hrs [27]. Moreover, vitality of stem cells after implantation is often decreased significantly depending on the method of delivery and delivery medium [28]. The model and techniques described in this work can be used to assess the minimum number of therapeutic cells required for positive stiffness outcomes. In Chapter 5, rat cardiac fibroblasts were cocultured with human MSC. We were able to differentiate between MSC and fibroblasts using a human specific nuclei stain. Methods described in Chapter 5 for quantification of cell distribution and density could be applied to determine the ratio of MSC to fibroblast throughout the substrate. In future studies using species matched cells, a method described by Radisic and colleagues propose modifying stem cells with a genetic indicator (yellow fluorescent protein marker) to differentiate between injected cells and "native" cells in engineered tissue models could be employed [29].

Other groups have used similar transfection approaches to identify MSC injected in *in vivo* models [23, 30]. Expansion of the current model system to include global cell tracking techniques will allow preliminary evaluation of approaches aimed at preventing stem cells from "washing away." Retention and survival data coupled with functional stiffness changes will help establish a starting point for minimum dosage to be used in vivo. This minimum local cell dosage number may then be used as an input for determining what delivery techniques can be used to meet this requirement.

In addition to investigating whether stems cells are retained after injection, the biomaterial-based model proposed in this work allows interrogation of phenotypic changes that occur during 3D fibroblast and MSC coculture. In general, fibroblast surface interactions with synthetic materials (and the materials' relatively high surface stiffness) tend to guide them toward an activated "myofibroblast" phenotype [31]. We observed that the majority of fibroblast expressed some level of α-SMA, indicative of a myofibroblastic phenotype. On the other hand, the fate of MSC after injection is still unclear. One study indicates that under certain circumstances, MSC recruited to the heart after infarction assume a fibroblast like phenotype [32]. The criteria to fully characterize the phenotype of a MSC in a cardiac environment has yet to be determined, and constitutes a field of future work necessary to understand the role of MSC in cardiac regeneration. An important next step for the model described in this work is to evaluate the phenotypic endpoint of the MSC during coculture. Understanding of phenotypic changes during coculture will speed design of appropriate stem cell treatment regimens and therefore clinical implementation.

6.2.3 Correlation of Bulk Tissue Behavior with Molecular Biology

Beyond its use as a tool to directly correlate stiffness with cell therapy regimens, the fibroblast model here can be used to better understand the molecular mechanisms involved with fibroblast mediated stiffness. As described in Chapter 1, fibroblasts regulate passive stiffness through a complex balance of ECM synthesis, degradation, and modification. Numerous regulatory components have been identified that are produced by fibroblasts, however there is considerable ambiguity surrounding the role that they play in regulating passive stiffness of cardiac tissue. For example, collagen deposition by CFb is generally considered to increase stiffness, however, after infarction in sheep, collagen content was shown to increase from ~40 μg/mg after 2 weeks to ~70 μg/mg after 6 weeks. At these same time points, the stiffness of the tissue decreased from 338.5 g/cm2 at 15% strain in the preferred direction to 115.6 g/cm2 [33]. The complexity of the relationship between molecular mechanisms and changes in observed stiffness are of paramount importance for heart failure. Several studies have shown that targeted deletion or inhibition of certain MMP or MMP inhibitors can prevent cardiac remodeling [34-36]. Application of engineered tissue models to understand how suppression, over-expression, or deletion of ECM regulatory factors impacts bulk stiffness will open new avenues for developing pharmacologic approaches to treating systolic and diastolic heart failure.

Future work using the engineered tissue described here aims to utilize western blot techniques to identify changes in protein expression resulting from MSC coculture. Methods employed by Mias et al. to quantify MMP expression and activity [20] could be could be adapted in a straight forward manner to this culture platform. The primary proteins of interest are for rat CFb regulation of ECM are MMP-2, MMP-9, TIMP-3 and

lysyl oxidase. Following culture, protein will be harvested and isolated, and then quantified using western blot techniques. In addition, more detailed qualitative analysis of ECM structure can be achieved through electron microscopy, or immunohistological approaches [37, 38]. Quantative evaluation of ECM components can be evaluated by serial digestion of ECM using matrix specific proteases as described by Tresco and colleagues [39].

### 6.2.4 Culture Platform Modifications

One of the current limitations of the culture platform described in this work is the inability to perform online tissue analysis. Laganá et al. have designed a optically accessible perfusion bioreactor for online evaluation of engineered microtissues [40]. Principles from their work could be simply applied to the culture cassette described here to provide optical access to the culture chamber without compromising sterility of the construct. The current design of the culture cassette utilizes a polycarbonate base plate. This material allows visualization of the substrate during culture. The major challenge, however, lies with overcoming limitations in working distances using higher magnification (> 10X) objectives. This problem could be approached through a redesign of the culture cassette to provide a coverslip "window" into the culture chamber. Further redesign of the position of the reservoir will be necessary as well to fit the entire culture cassette onto most imaging stages. Confocal microscopy permits visualization approximately 100 μm into the polyurethane scaffold (unpublished observation). Two-photon microscopy may increase the achievable imaging depth [41]. Second harmonic generation (SHG) allows live imaging of collagen and elastin structure without requiring

staining [42, 43]. An optically accessible culture chamber will allow real-time evaluation of development and changes in extracellular matrix structure as well as cellular distribution, density and vitality.

The methods used to fabricate the biomaterial substrate described in this dissertation have been optimized, and with the exception the lamination, automated. The reproducibility of the substrate has been evaluated over the course of 2 years of production. This material has the potential to serve as a foundational component for many 3D cell culture systems. Further development of the fabrication methods can lead to a customizable biomaterial cell substrate that can be made available as a foundational starting point for 3D cell culture to a wide variety of research groups.

## 6.3 References

[1] Mulder MM, Hitchcock RW, Tresco PA. Skeletal myogenesis on elastomeric substrates: implications for tissue engineering. J Biomater Sci Polym Ed. 1998;9:731-48.

[2] Khorasani MT, Shorgashti S. Fabrication of microporous polyurethane by spray phase inversion method as small diameter vascular grafts material. J Biomed Mater Res A. 2006;77:253-60.

[3] Okoshi T, Chen H, Soldani G, Galletti PM, Goddard M. Microporous small diameter PVDF-TrFE vascular grafts fabricated by a spray phase inversion technique. ASAIO J. 1992;38:M201-6.

[4] Papenburg B, Vogelaar L, Bolhuis-Versteeg L, Lammertink R, Stamatialis D, Wessling M. One-step fabrication of porous micropatterned scaffolds to control cell behavior. Biomaterials. 2007;28:1998-2009.

[5] Hollister S, Wang Y, Wang G, Chen L, Li H, Yin T, et al. Scaffold engineering: a bridge to where? : Biofabrication; 2009;1:012001-14.

[6] Radisic M, Yang L, Boublik J, Cohen RJ, Langer R, Freed LE, et al. Medium perfusion enables engineering of compact and contractile cardiac tissue. American Journal of Physiology- Heart and Circulatory Physiology. 2004;286:507-16.

[7] Carrier RL, Rupnick M, Langer R, Schoen FJ, Freed LE, Vunjak-Novakovic G. Perfusion improves tissue architecture of engineered cardiac muscle. Tissue Engineering. 2002;8:175-88.

[8] Liu C, Abedian R, Meister R, Haasper C, Hurschler C, Krettek C, et al. Influence of perfusion and compression on the proliferation and differentiation of bone mesenchymal stromal cells seeded on polyurethane scaffolds. Biomaterials. 2011;33:1052-64.

[9] Maidhof R, Tandon N, Lee EJ, Luo J, Duan Y, Yeager K, et al. Biomimetic perfusion and electrical stimulation applied in concert improved the assembly of engineered cardiac tissue. J Tissue Eng Regen Med. 2012;6:e12-23.

[10] Zhao F, Pathi P, Grayson W, Xing Q, Locke BR, Ma T. Effects of oxygen transport on 3-D human mesenchymal stem cell metabolic activity in perfusion and static cultures: experiments and mathematical model. Biotechnology Progress. 2005;21.

[11] Radisic M, Deen W, Langer R, Vunjak-Novakovic G. Mathematical model of oxygen distribution in engineered cardiac tissue with parallel channel array perfused with culture medium containing oxygen carriers. American Journal of Physiology-Heart and Circulatory Physiology. 2005;288:1278-89.

[12] Kretzmer G, Schügerl K. Response of mammalian cells to shear stress. Applied Microbiology and Biotechnology. 1991;34:613-6.

[13] McCoy RJ, Jungreuthmayer C, O'Brien FJ. Influence of flow rate and scaffold pore size on cell behavior during mechanical stimulation in a flow perfusion bioreactor. Biotechnol Bioeng. 2012;109:1583-94.

[14] McCoy RJ, O'Brien FJ. Influence of shear stress in perfusion bioreactor cultures for the development of three-dimensional bone tissue constructs: a review. Tissue Eng Part B Rev. 2010;16:587-601.

[15] Papenburg BJ, Bolhuis-Versteeg LA, Grijpma DW, Feijen J, Wessling M, Stamatialis D. A Facile Method to Fabricate Poly(L-lactide) Nano-fibrous Morphologies by Phase Inversion. Acta Biomater. 2010;6:2477-83.

[16] Maidhof R, Marsano A, Lee EJ, Vunjak-Novakovic G. Perfusion seeding of channeled elastomeric scaffolds with myocytes and endothelial cells for cardiac tissue engineering. Biotechnol Prog. 2010;26:565-72.

[17] Shi ZD, Tarbell JM. Fluid flow mechanotransduction in vascular smooth muscle cells and fibroblasts. Ann Biomed Eng. 2011;39:1608-19.

[18] Zhang T, Wan LQ, Xiong Z, Marsano A, Maidhof R, Park M, et al. Channelled scaffolds for engineering myocardium with mechanical stimulation. J Tissue Eng Regen Med. 2011;6:748-756.

[19] Menasche P. Cardiac cell therapy: lessons from clinical trials. J Mol Cell Cardiol. 2010;50:258-65.

[20] Mias C, Lairez O, Trouche E, Roncalli J, Calise D, Seguelas MH, et al. Mesenchymal stem cells promote matrix metalloproteinase secretion by cardiac fibroblasts and reduce cardiac ventricular fibrosis after myocardial infarction. Stem Cells. 2009;27:2734-43.

[21] Wang Y, Hu X, Xie X, He A, Liu X, Wang JA. Effects of mesenchymal stem cells on matrix metalloproteinase synthesis in cardiac fibroblasts. Exp Biol Med (Maywood). 2011;236:1197-204.

[22] Lian WS, Cheng WT, Cheng CC, Hsiao FS, Chen JJ, Cheng CF, et al. In vivo therapy of myocardial infarction with mesenchymal stem cells modified with prostaglandin I synthase gene improves cardiac performance in mice. Life Sci. 2011;88:455-64.

[23] Fang J, Chen L, Fan L, Wu L, Chen X, Li W, et al. Enhanced therapeutic effects of mesenchymal stem cells on myocardial infarction by ischemic postconditioning through paracrine mechanisms in rats. J Mol Cell Cardiol. 2011;51:839-47.

[24] Gnecchi M, He H, Liang OD, Melo LG, Morello F, Mu H, et al. Paracrine action accounts for marked protection of ischemic heart by Akt-modified mesenchymal stem cells. Nat Med. 2005;11:367-8.

[25] Seeger FH, Tonn T, Krzossok N, Zeiher AM, Dimmeler S. Cell isolation procedures matter: a comparison of different isolation protocols of bone marrow mononuclear cells used for cell therapy in patients with acute myocardial infarction. Eur Heart J. 2007;28:766-72.

[26] Wu KH, Han ZC, Mo XM, Zhou B. Cell delivery in cardiac regenerative therapy. Ageing Res Rev. 2011;11:32-40.

[27] Menasche P. Stem cell therapy for chronic heart failure: lessons from a 15-year experience. C R Biol. 2011;334:489-96.

[28] Terrovitis JV, Smith RR, Marban E. Assessment and optimization of cell engraftment after transplantation into the heart. Circ Res. 2010;106:479-94.

[29] Song H, Yoon C, Kattman SJ, Dengler J, Masse S, Thavaratnam T, et al. Interrogating functional integration between injected pluripotent stem cell-derived cells and surrogate cardiac tissue. Proc Natl Acad Sci U S A. 2010;107:3329-34.

[30] Hamdi H, Planat-Benard V, Bel A, Puymirat E, Geha R, Pidial L, et al. Epicardial adipose stem cell sheets results in greater post-infarction survival than intramyocardial injections. Cardiovasc Res. 2010;93:483-91.

[31] Li Z, Dranoff JA, Chan EP, Uemura M, Sevigny J, Wells RG. Transforming growth factor-beta and substrate stiffness regulate portal fibroblast activation in culture. Hepatology (Baltimore, Md). 2007;46:1246-56.

[32] Sato D, Otani H, Enoki C, Fujita M, Minato N, Iwasaka T. Phenotypic modulation and turnover of bone marrow-derived cells after myocardial infarction in rats. Cardiovasc Pathol. 2011;20:146-55.

[33] Gupta KB, Ratcliffe MB, Fallert MA, Edmunds LH, Jr., Bogen DK. Changes in passive mechanical stiffness of myocardial tissue with aneurysm formation. Circulation. 1994;89:2315-26.

[34] Limana F, Esposito G, D'Arcangelo D, Di Carlo A, Romani S, Melillo G, et al. HMGB1 Attenuates Cardiac Remodelling in the Failing Heart via Enhanced Cardiac Regeneration and miR-206-Mediated Inhibition of TIMP-3. PLoS One. 2011;6:e19845.

[35] Spinale FG, Mukherjee R, Zavadzkas JA, Koval CN, Bouges S, Stroud RE, et al. Cardiac restricted overexpression of membrane type-1 matrix metalloproteinase causes adverse myocardial remodeling following myocardial infarction. J Biol Chem. 2010;285:30316-27.

[36] Hayashidani S, Tsutsui H, Ikeuchi M, Shiomi T, Matsusaka H, Kubota T, et al. Targeted deletion of MMP-2 attenuates early LV rupture and late remodeling after experimental myocardial infarction. Am J Physiol Heart Circ Physiol. 2003;285:H1229-35.

[37] Rossi MA. Connective tissue skeleton in the normal left ventricle and in hypertensive left ventricular hypertrophy and chronic chagasic myocarditis. Medical Science Monitor : International Medical Journal of Experimental and Clinical Research. 2001;7:820-32.

[38] Lasher RA, Pahnke AQ, Johnson JM, Sachse FB, Hitchcock RW. Electrical stimulation directs engineered cardiac tissue to an age-matched native phenotype. J Tissue Eng. 2012;3:2041731412455354.

[39] Wolchok JC, Tresco PA. The isolation of cell derived extracellular matrix constructs using sacrificial open-cell foams. Biomaterials. 2010;31:9595-603.

[40] Lagana M, Raimondi MT. A miniaturized, optically accessible bioreactor for systematic 3D tissue engineering research. Biomed Microdevices. 2011;14:225-34.

[41] Helmchen F, Denk W. Deep tissue two-photon microscopy. Nat Methods. 2005;2:932-40.

[42] Zipfel WR, Williams RM, Christie R, Nikitin AY, Hyman BT, Webb WW. Live tissue intrinsic emission microscopy using multiphoton-excited native fluorescence and second harmonic generation. Proc Natl Acad Sci U S A. 2003;100:7075-80.

[43] Zoumi A, Lu X, Kassab GS, Tromberg BJ. Imaging coronary artery microstructure using second-harmonic and two-photon fluorescence microscopy. Biophys J. 2004;87:2778-86.

# APPENDIX

## ENGINEERING PRINTS OF PERFUSION BIOREACTOR

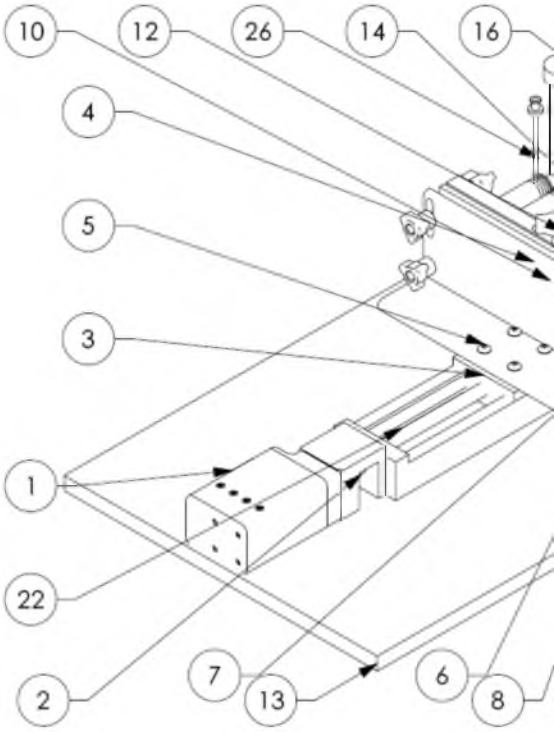
10
12
26
14
16
4
5
3
1
22
2
7
13
6
8

| REV | DESCRIPTION | DWN | DATE |
|---|---|---|---|
| 01 | INITIAL RELEASE | JK | 12/1/11 |
| | | | |
| | | | |
| | | | |
| | | | |

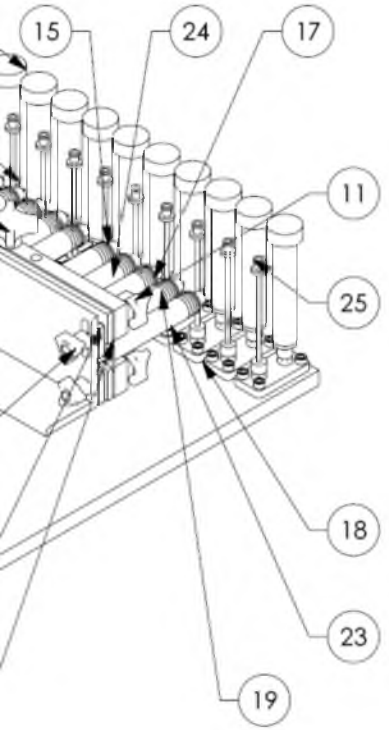


**UNIVERISTY OF UTAH**

| | | |
|---|---|---|
| TITLE: Perfusion Bioreactor | | |
| SIZE A | DWG. NO. N/A | REV 01 |
| PART NO: N/A | SPEC: N/A | |
| MODEL FILE: Perfusion bioreactor | | |
| SCALE: 1:8 | | SHEET 1 OF 2 |

| ITEM NO. | PART NUMBER | DESCRIPTION | QTY. |
|---|---|---|---|
| 1 | SM17205D | Animatic Smart motor series stepper motor | 1 |
| 2 | motor to slide coupler | Thomson motor to slide coupler - included with part number MS33LEAL200 | 1 |
| 3 | Linear slide platform | Thomson linear slide bearing, included with PN: MS33LEAL200 | 1 |
| 4 | Syringe clamp-Mounted plnger clamp | Custom machined 6061 aluminum | 1 |
| 5 | 91239A228 | Black Finish Steel button head socket cap screw M5, McMaster | 4 |
| 6 | Syringe clamp-Threaded plunger clamp | Custom machined 6061 aluminum | 2 |
| 7 | 57715K38 | 1/4-20 x 1/2" Phenolic three arm knob with threaded stud, McMaster | 4 |
| 8 | Syringe clamp-Mounted barrel clamp | Custom machined 6061 aluminum | 2 |
| 9 | 91239A152 | Black finish steel button head socket cap screw M4, McMaster | 2 |
| 10 | Syringe clamp-Threaded barrel clamp | Custom machined 6061 aluminum | 2 |
| 11 | 57715K44 | 1/4-20 x 3/4" Phenolic three arm knob with threaded stud, McMaster | 4 |
| 12 | 60965K32 | 1/4-20 x 3" Aluminum four arm knob with threaded stud, McMaster | 1 |
| 13 | base plate | Delrin base plate | 1 |
| 14 | 097041E | Size 16D silicone stopper, Fisher | 10 |
| 15 | 11553 | Polycarbonate male leur lock to barb connector, fits 3/16" ID tubing, Qosina | 10 |
| 16 | 352096 | BD 15 ml syringe, modified | 10 |
| 17 | culture chamber top plate | Machined polycarbonate | 10 |
| 18 | culture chamber holding plate | Machined polycabonate | 10 |
| 19 | EW-45501-66 | Polycarbonate threaded female luer | 20 |
| 20 | scaffold | Polyurethane Scaffold | 10 |
| 21 | silicone gasket | Custom molded VST 50 platinum cure silicone | 10 |
| 22 | MS33LEAL200 | Thomson Industries Inc linear motion system | 1 |
| 23 | 92185A969 | #10-32 Stainless Steel | 44 |
| 24 | 11545 | Polycarbonate male luer lock to barb connector, fits 1/16" ID tubing | 10 |
| 25 | 11556 | Polycarbonate female luer lock to barb connector, fits 1/16" ID tubing | 10 |
| 26 | EW-064110-62 | Peroxide cured silicone tubing, 1/16" ID, 1/8" OD, 4" length | 10 |
| 27 | 9396K203 | 3/16"ID 7/16" OD silicone O-ring McMaster-Carr PN 9396K203 | 20 |
| 28 | 10 ml plunger | Exel Int 10ml Luer Lock Tip Plunger P/N 26265 | 10 |
| 29 | 10 ml Syringe barrel | Exel Int 10ml Luer Lock Tip Syringe P/N 26265 | 10 |

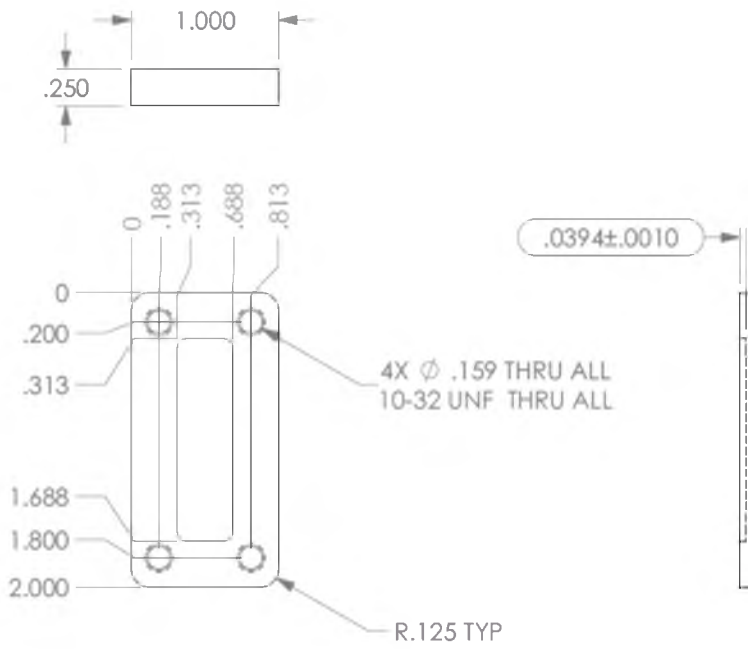
1.000
.250
0
.188
.313
.688
.813
.0394±.0010
0
.200
.313
4X ∅ .159 THRU ALL
10-32 UNF THRU ALL
1.688
1.800
2.000
R.125 TYP

| REV | DESCRIPTION | DWN | DATE |
|---|---|---|---|
| 01 | INITIAL RELEASE | JK | 12/2/11 |
| | | | |
| | | | |
| | | | |
| | | | |

NOTE: Circled dimensions
must be 100% inspected

**UNIVERISTY OF UTAH**
20 S 2030 E Rm 108
Salt Lake City, 84112

TITLE:
Culture Chamber: Holding plate

| SIZE | DWG. NO. | REV |
|---|---|---|
| A | N/A | 01 |

PART NO: N/A SPEC: N/A

MODEL FILE:
culture chamber holding plate

SCALE: 2:1 SHEET 1 OF 1

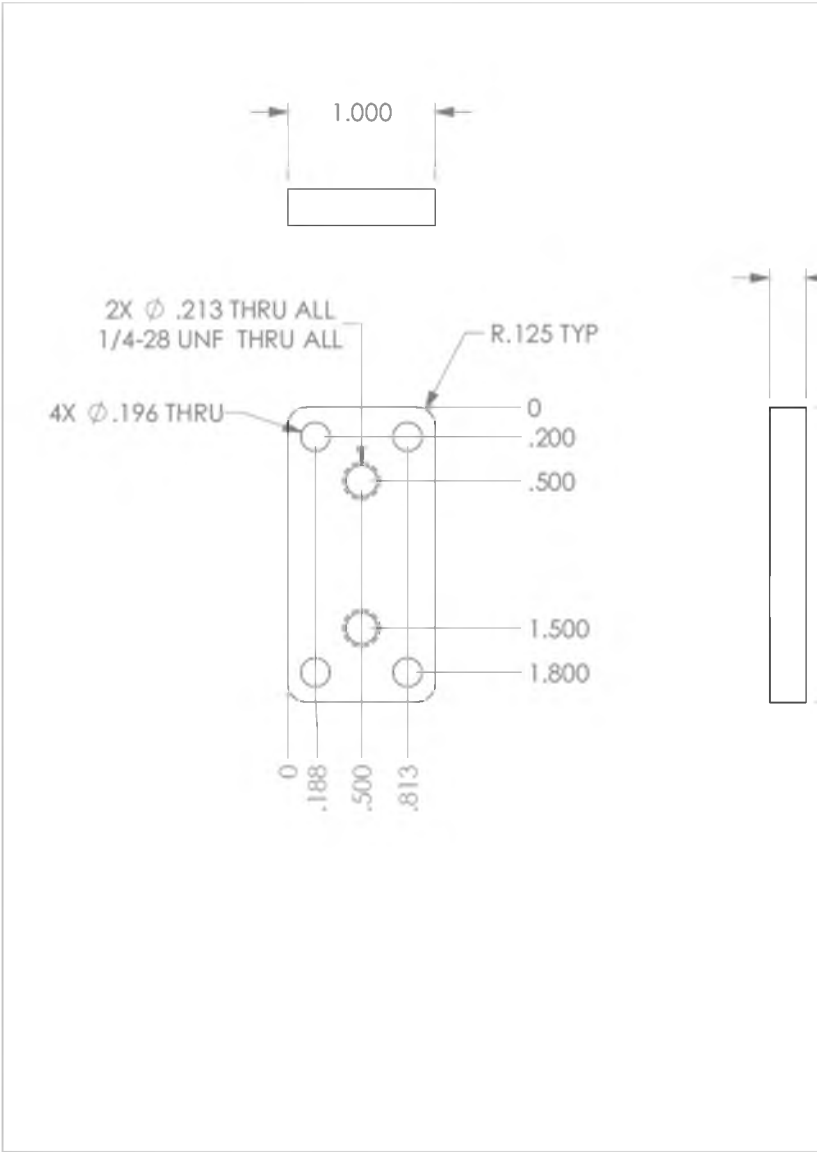
1.000
2X ∅ .213 THRU ALL
1/4-28 UNF THRU ALL
R.125 TYP
4X ∅.196 THRU
0
.200
.500
1.500
1.800
0
.188
.500
.813

| REV | DESCRIPTION | DWN | DATE |
|---|---|---|---|
| 01 | INITIAL RELEASE | JK | 12/2/11 |
| | | | |
| | | | |
| | | | |
| | | | |

.250

2.000

**UNIVERISTY OF UTAH**
20 S 2030 E Rm 108
Salt Lake City, 84112

TITLE:
Culture Chamber: Top plate

| SIZE | DWG. NO. | REV |
|---|---|---|
| A | N/A | 01 |

PART NO: N/A SPEC: N/A

MODEL FILE:
culture chamber top plate

SCALE: 2:1 SHEET 1 OF 1

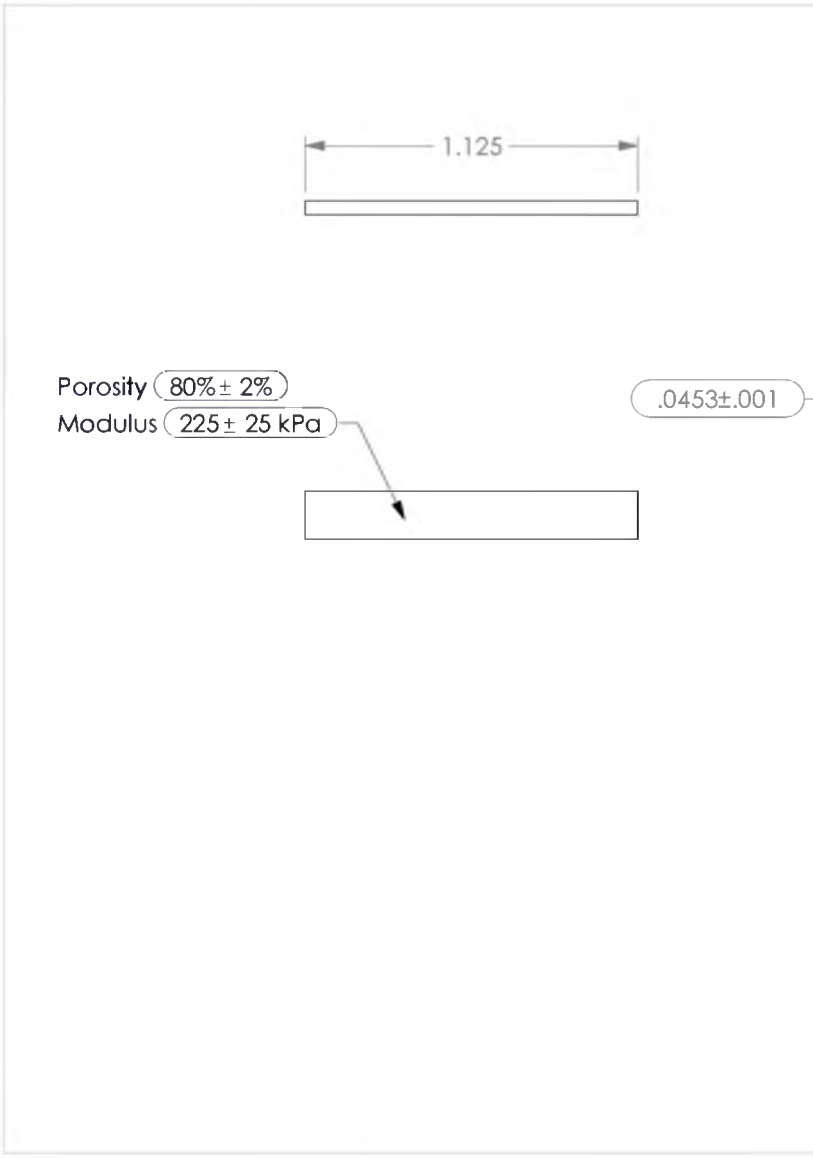
1.125
Porosity 80% ± 2%
Modulus 225 ± 25 kPa
.0453±.001

| REV | DESCRIPTION | DWN | DATE |
|---|---|---|---|
| 01 | INITIAL RELEASE | JK | 12/2/11 |
| | | | |
| | | | |
| | | | |
| | | | |

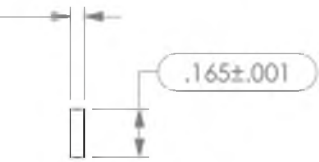


**UNIVERISTY OF UTAH**
20 S 2030 E Rm 108
Salt Lake City, 84112

TITLE: Scaffold

| SIZE | DWG. NO. | REV |
|---|---|---|
| A | N/A | 01 |

PART NO: N/A SPEC: N/A

MODEL FILE: scaffold

SCALE: 4:1 SHEET 1 OF 1

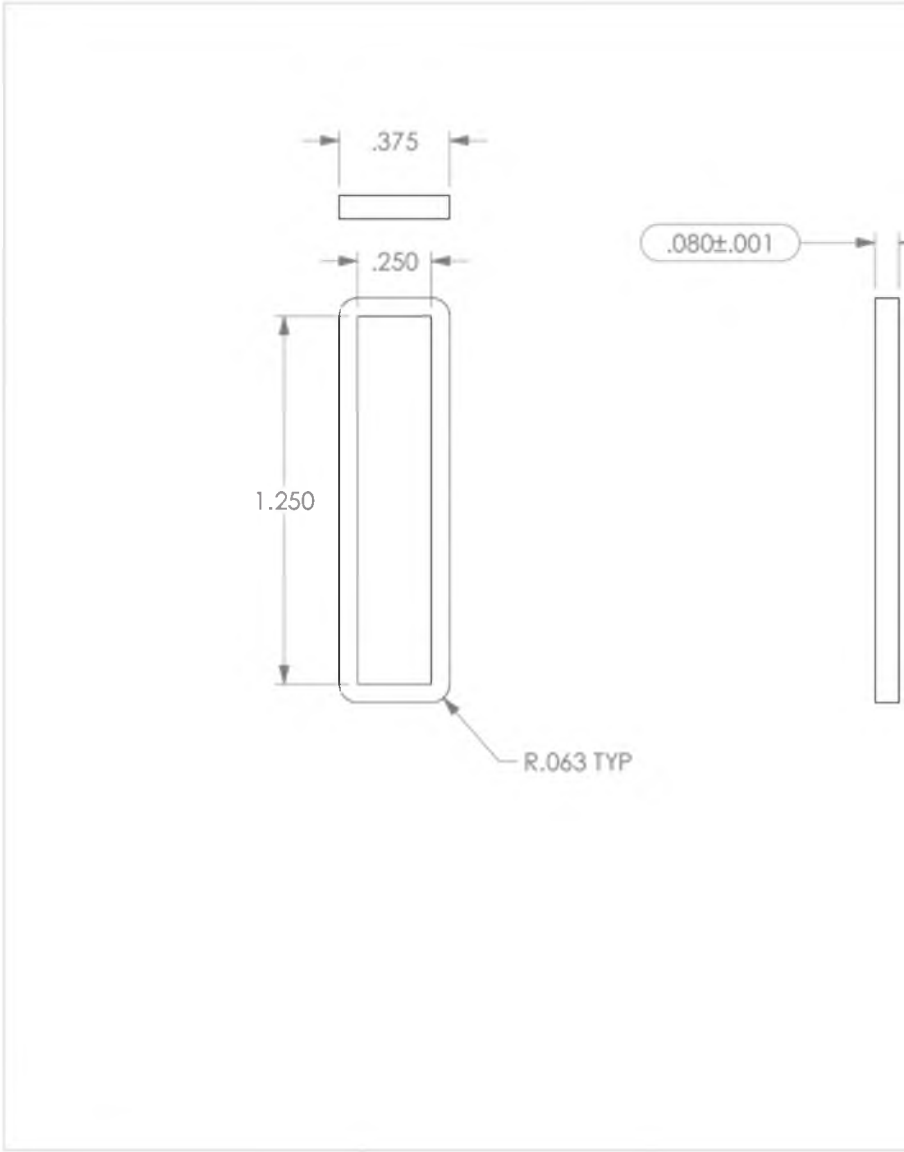
.375
.250
1.250
.080±.001
R.063 TYP

| REV | DESCRIPTION | DWN | DATE |
|---|---|---|---|
| 01 | INITIAL RELEASE | JK | 12/2/11 |
| | | | |
| | | | |
| | | | |
| | | | |


**UNIVERISTY OF UTAH**
20 S 2030 E Rm 108
Salt Lake City, 84112

TITLE:
Silicone gasket

| SIZE | DWG. NO. | REV |
|---|---|---|
| A | N/A | 01 |

PART NO: N/A SPEC: N/A

MODEL FILE: silicone gasket

SCALE: 2:1 SHEET 1 OF 1


CUT TO LENGTH
3.410

| REV | DESCRIPTION | DWN | DATE |
|---|---|---|---|
| 01 | INITIAL RELEASE | JK | 10/25/11 |
| | | | |
| | | | |
| | | | |
| | | | |

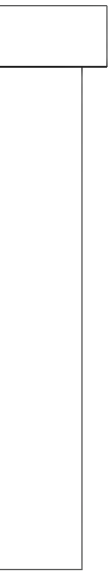

**UNIVERISTY OF UTAH**
20 S 2030 E Rm 108
Salt Lake City, 84112

TITLE: Reservoir

| SIZE | DWG. NO. | REV |
|---|---|---|
| A | N/A | 01 |

PART NO: N/A SPEC: N/A

MODEL FILE: Reservoir

SCALE: 1:1 SHEET 1 OF 1

| REV | DESCRIPTION | DWN | DATE |
|---|---|---|---|
| 01 | INITIAL RELEASE | JK | 12/2/11 |

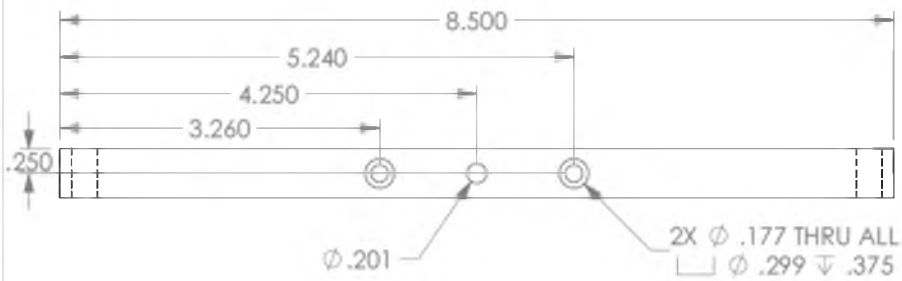


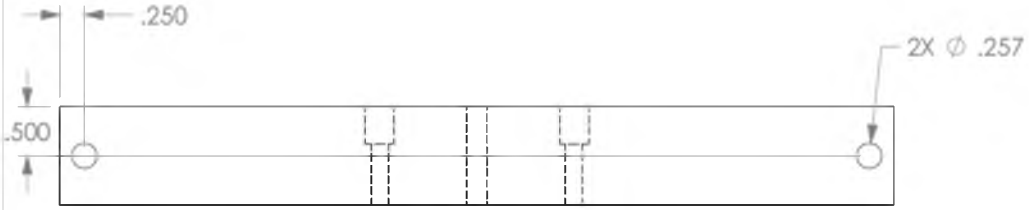


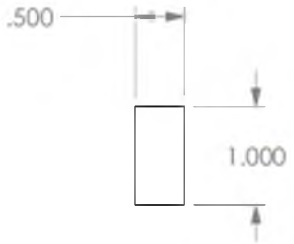


**UNIVERISTY OF UTAH**
20 S 2030 E Rm 108
Salt Lake City, 84112

TITLE:
Syringe clamp: Mounted barrel clamp

| SIZE | DWG. NO. | REV |
|---|---|---|
| A | N/A | 01 |

PART NO: N/A SPEC: N/A

MODEL FILE:
Syringe clamp-Mounted barrel clamp

SCALE: 1:2 SHEET 1 OF 1

| REV | DESCRIPTION | DWN | DATE |
|---|---|---|---|
| 01 | INITIAL RELEASE | JK | 12/2/11 |


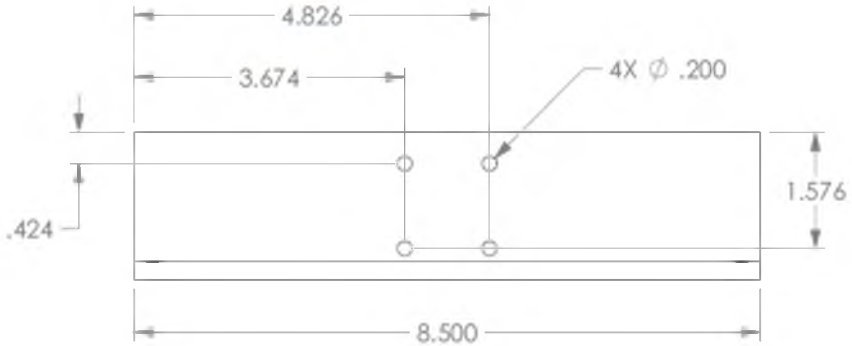


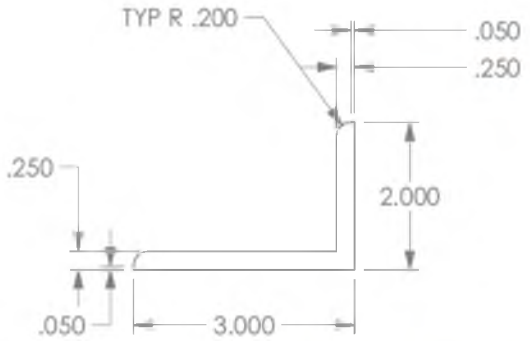


**UNIVERISTY OF UTAH**
20 S 2030 E Rm 108
Salt Lake City, 84112

TITLE:
Syringe clamp: Mounted plunger clamp

| SIZE | DWG. NO. | REV |
|---|---|---|
| A | N/A | 01 |

PART NO: N/A SPEC: N/A

MODEL FILE:
Syringe clamp-Mounted plnger clamp

SCALE: 1:2 SHEET 1 OF 1

| REV | DESCRIPTION | DWN | DATE |
|---|---|---|---|
| 01 | INITIAL RELEASE | JK | 12/2/11 |


**UNIVERISTY OF UTAH**
20 S 2030 E Rm 108
Salt Lake City, 84112

TITLE:
Syring clamp-Threaded Barrel clamp

| SIZE | DWG. NO. | REV |
|---|---|---|
| A | N/A | 01 |

PART NO: N/A SPEC: N/A

MODEL FILE:
Syringe clamp-Threaded barrel clamp

SCALE: 1:2 SHEET 1 OF 1

| REV | DESCRIPTION | DWN | DATE |
|---|---|---|---|
| 01 | INITIAL RELEASE | JK | 12/2/11 |


**UNIVERISTY OF UTAH**
20 S 2030 E Rm 108
Salt Lake City, 84112

TITLE: Syringe clamp: Threaded plunger clamp

| SIZE | DWG. NO. | REV |
|---|---|---|
| A | N/A | 01 |

PART NO: N/A SPEC: N/A

MODEL FILE:
Syringe clamp-Threaded plunger clamp

SCALE: 1:2 SHEET 1 OF 1